A THESIS
FOR THE DEGREE OF DOCTOR OF PHILOSOPHY

Investigation of Electrical Transport Properties of Graphene Layers and its Optoelectronic Applications

KALIANNAN THIYAGARAJAN

Department of Mechatronics Engineering

GRADUATE SCHOOL
JEJU NATIONAL UNIVERSITY

2015. 02

Investigation of Electrical Transport Properties of Graphene Layers and its Optoelectronic Applications

Kaliannan Thiyagarajan
(Supervised by Professor Sang-Jae Kim)

A thesis submitted in partial fulfillment of the requirement for the degree of
Doctor of Philosophy

2014. 12.

This thesis has been examined and approved.

Thesis Director, Prof. Jin-Ho Bae	Professor, Department of Ocean System Engineering, College of Ocean Science, Jeju National University
Thesis Committee Member, Prof. Young-Sun Mok	Professor, Department of Chemical and Biological Engineering, Jeju National University
Thesis Committee Member, Prof. Sang-Jae Kim	Sangjae Kim Professor, Department of Mechatronics Engineering, College of Engineering, Jeju National University
Thesis Committee Member, Prof. Hyeon Suk Shin	Associate Professor, Department of Chemistry, Ulsan National Institute of Science and Technology
Thesis Committee Member, Prof. Sang Min Lee	Assistant Professor, School of Mechanical Engineering, Chung-Ang University

December 11, 2014.

Department of Mechatronics Engineering

GRADUATE SCHOOL

JEJU NATIONAL UNIVERSITY

REPUBLIC OF KOREA

Dedicated to

My beloved parents, family members, wife and my dear friends

For their endless love, support and encouragement

Thesis Overview

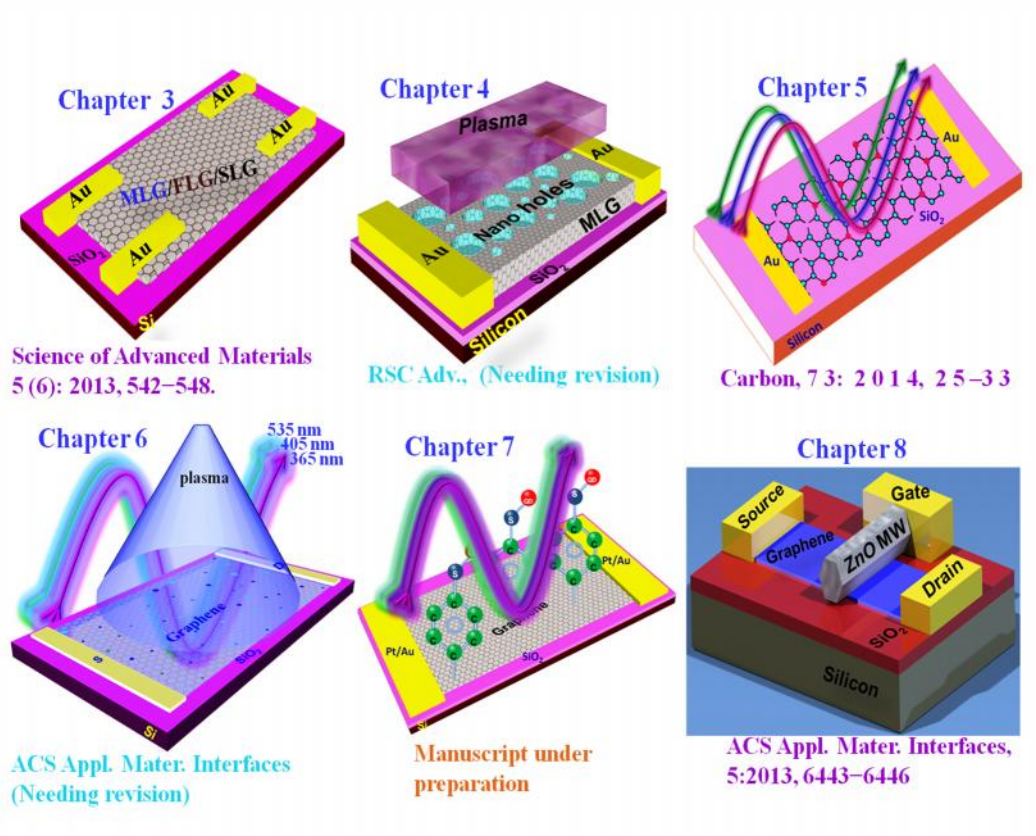

ACKNOWLEDGEMENT

Foremost, my thanks to God for protection and the ability to do the work. Next, I would like to express my sincere gratitude to my supervisor Prof. Sang-Jae KIM, for the continuous support of my Ph.D study and research, for his patience, motivation, enthusiasm, and immense knowledge, his guidance helped me in all the time of research and writing of this thesis. I could not have imagined having a better advisor and mentor for my Ph.D study. Besides my advisor, I would like to thank the rest of my thesis committee for their encouragement, insightful comments, and hard questions.

My heartfelt thanks to Prof. Young-Sun Mok and his student my friend Mr. Antony Ananth, for their support and allowing me to use their the lab facility. With deep sense of gratitude, I Sincerely take this opportunity to express my heartfelt thanks to Dr.M.Sivakumar, Dr.S.Brahadeeswaran, Dr.R.Nandhakumar, Dr. A. Dhayal Raj, Dr.G.Arthanareeswaran, Dr.G.Senguttuvan, Dr.R.Kannan, Dr.Thambidurai, Dr. Manivasakan, Dr. Dharaneetharan, Dr. Anil Khambampatti, Dr Saranaya, for their valuable guidance, and support throughout my studies and also for their valuable information that always helping me to build my future career.

I am exceedingly thankful to current and former members of our group, without their support this work couldn’t possible, first, I would like to thank Dr. Rajneesh Mohan, and Dr. Shrikant Saini for their teaching and guidance and I also thankful to Dr.Gunasekaran Venugopal, Dr. Karthikeyan Krishanamurthy for their support. I am very happy and delighted to thank my friends Mr. Balasubramaniam Saravanakumar, Mr. Ananthakumar Ramadoss, Mr. Eui-Youg Hong, Mis. Shin So Yoon, Mr. Kim Taehyun, Dr. Sivaprakasam Radhakrishnan, Mr. Veerasubramani Ganesh Kumar, Mr. Nagamelleshwara Rao, Mr. Arunkumar, Ms. Sophia Selvarajan, Mr. Ko Eunhyung, Ms. Park Minhee and Mr.Seong Mingeon.

Friends are the backbone of my life without their help and motivation, I cannot move forward in my life as well as in the career. This is the occasion to thank all of my beloved friends, they stayed with me during the hard part of my life and lifted from that situation with the words of we are always with you lets go head, I would like to thank my friends from childhood, Mr. R.Manikandan, Mr.U.Ravikumar, Mr.J.Kamalraj, Mr.Sathish, Mr.Sasikumar, Mr.C.Saravanan, Mr. Mr.R.Logesh, and Mr.Boss. I also want to thank my undergraduate and graduate friends Mr.Padmaraj, Mr.V.Venkatesan, Mr.Subramani, Mr. Sampath, Mr.T.Sasietharan, Mr.M.Jagadesh, Mr.V.Vivekananthan, Mr.R.Suresh, for their support and love. The unconditional love from my friends really motivated me to this work, here I have to acknowledge them with my deepest thanks to Ms.P.Kowsalya, Ms.A.Ranjitha, Mr.N.Balaji, Mr.J.Dhayanandhaprabu, Mr.L.Raja, Mr.R.Laxminarayanan Mrs.T.Thenmozhi, Mrs.Shobana, Mr. Uloganathan, Mr.Pradhap Mr.M.R.M.Panani praphu raja, and Mr.Subbiah Ramesh.

I would like to thank Jeju friends, they make a homely environment during the stay. Dr. Umasuthan, Dr. Karuppiah, Mr. M.S.V. Sudhakar, Miss.M.S Mothishri, Dr. Navaneethan, Dr.Ganesh Thangaraj, Dr.Sridharan, Dr.Gandhi, Dr. Kalpa, Dr.Nauman, Dr.Murtaza, Dr.Zubair, Mr.Kamran Ali, Mr. Suresh Rai, Dr. Adanan Ali,

Mr. Mamoon, Dr.Naeem, Mr.Safdar, Mr.Farrukh, Mr.Razhid, Mr.Sohail, Mr. Junaid, Mr.Lakmal.

I am also grateful for the Research Instrument Centre for their valuable support and permission given to handle all experimental and characterization facilities.

Last but certainly not least, I thank my father Mr. S. Kaliannan, mother Ms. K. Sellammal and my brothers (Yogaraj and Rathinaraj), sister (Shanthi) and family members and my beloved wife Mrs. Rajeswari Thiyagarajan. They have provided unconditional love and care. Finally, I acknowledge the friends those are not mentioned here they helped me a lot of different occasions.

Table of Contents

I **Introduction**

II **Device Fabrication and Measurement Setup**

III Thickness dependent Electrical Transport Properties of Graphene Layers

IV Defect-induced Metallic-to-Semiconducting Transition in Multilayer Graphene

V **Plasma-induced Photoresponse in Fewlayer Graphene**

VI **Gate-tunable Photoresponse of Defective Graphene: from Ultraviolet to Visible**

VII **Graphene-CdSe Quantum dot Hybrid Device for Photosensing Applications**

List of Tables

List of Figures

초록

이 논문은 기본 및 결함상태에서 그래핀 층의 전기 수송 특성을 조사하였으며, 또한 결함 그래핀의 광 감지 활용과 그래핀 양자점 하이브리드 장치의 활용또한 포함한다. 첫 장에서는 그래핀에 대한 설명과 그래핀의 두께 의존 특성, 결함이 그래핀 층에 미치는 영향에 대한 배경지식을 설명하였다. 2장에서는 그래핀층의 준비과정, 소자제작, 처리과정, 측정 및 응용과 관련한 전반적인 내용을 설명하였다.

3장에서는 무결함 다층 및 몇 개의 다층 그리고 단층 그래핀의 두께에 따른 전기 수송 특성에 대해 연구하였으며 그 결과, 플레이크 두께의 작용으로 금속성이 반도체로 전이하는 것으로 분석했다. 4장에서는 결함이 있거나 없는 다층 그래핀의 전자 수송 특성을 다루었다. 결함이 많은 다층 그래핀은 반도체와 같이 저항에 따른 온도 의존성을 나타냈다.

5장에서는, midgap밴드 결함상태의 다층 그래핀이 광감응성 경향을 맞출수 있는 새로운 방법을 소개하였다. 6장에서는 가시영역에 자외선을 통해 결함이 있는 단층 그래핀의 게이트 조정 광감응성 특성을 확인하였다. 그래핀 - CdSe 양자점 하이브리드 소자의 광감지 기능에 대해 7장에서 조사하였다. 마지막 장에서는 자가유도 유전체 층과 탑 게이트 전극역할인 ZnO 마이크로와이어를 바탕으로 한 avant-grade 그래핀 전계효과 트랜지스터의 특성에 대해 입증하였다.

Abstract

This dissertation investigates the electrical transport properties of graphene layers at pristine and defected states. It also covers the photo-sensing applications of defective-graphene as well as the graphene quantum dot hybrid device.

The first chapter portrays the background information about graphene and thickness dependent properties of graphene and effect of defects on graphene layers. Where the second chapter describes the general overview of the steps involved in the graphene layer preparation, device fabrication, processing, measurements and its application.

In chapter three I have investigated the thickness dependent electrical transport properties of an ideal defect- free multilayer, few-layer and single layer graphene and the results were interpreted as a metallic to semiconducting transition as a function of flake thickness.

The chapter four deals with the electronic transport properties of the multilayer graphene with and without defect. The defect-rich multilayer graphene exhibits semiconductor-like temperature dependence of the resistance.

In chapter five, we introduce a novel way to tailor the photoresponsive behavior from few layer graphene by introducing a defect midgap states band. In chapter six we demonstrated the gate tunable photoresponsive behavior of the defective single layer graphene over ultraviolet to the visible region.

The photo-sensing capability of graphene-CdSe QDs hybrid device was investigated and presented in chapter seven. In the final chapter, we demonstrated the performance of the avant-grade graphene field effect transistor based on ZnO microwire as a top-gate electrode with self-induced dielectric layer.

CHAPTER I

Introduction

In this chapter we will provide the background information on thickness dependent properties of graphene and effect of defects on graphene layers and its phoresponsive nature, finally we introduce the motivation of our research.

1.1 Carbon

Carbon is the basic building block of organic materials and is abundant on earth, which has six electrons corresponding to the electron configuration, $1s^2 2s^2 2p^2$. The $1s$ electrons are firmly bound to the nuclei will not contribute to electronic transport. Whereas the $2s$ and $2p$ are weakly bound, plays a key role in determining electronic properties, when the carbon atoms are assembled together, theses four valence electrons take part in the formation of covalent bonds through orbital hybridization. Depending on the types of hybridization and shape of the physical structure, carbon forms different allotropes, such as diamond, graphite, carbon nanotube, fullerene and **graphene**.

1.2 Graphene

Graphene, mother of all graphitic material, is one - atom thick,[1] with an exclusive topological arrangement of carbon atoms, which provides extraordinary physical properties such as high electrical and thermal conductivity and high mechanical stiffness and strength, which makes it suitable for many applications,[1-4] see Fig.1.1 for the structures. Electrons and holes in this 2D material obey a linear energy dispersion relation near the Fermi level and behave as relativistic, massless particles (i.e. Dirac fermions) leads the electronic property of graphene. [5]

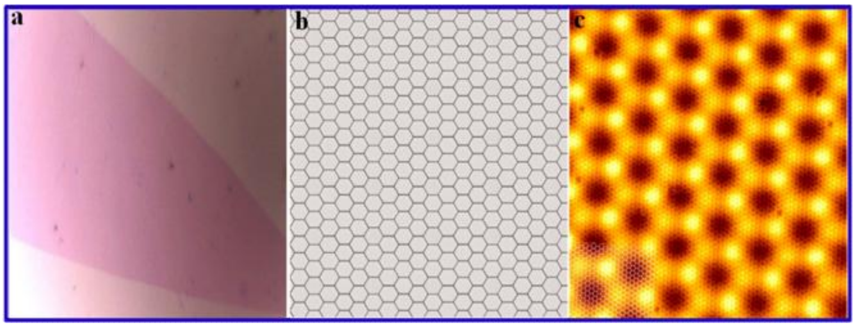

Fig.1.1. (a) Optical image of graphene on Si/SiO2 substrate, (b) schematic of the graphene layer (c) scanning tunneling microscopy image of graphene layer.

1.3 Thickness dependent properties of graphene layers

Graphene properties significantly vary with respect to the flake thickness (number of layers). Based on the thickness, graphene is divided into five groups, such as multilayer, few layer, trilayer, bilayer and single layer. In this thesis, we have investigated properties of multilayer graphene (MLG), fewlayer graphene (FLG) and single layer graphene (SLG) see Fig.1.2 for schematic and electronic band diagram of the above mention thickness.

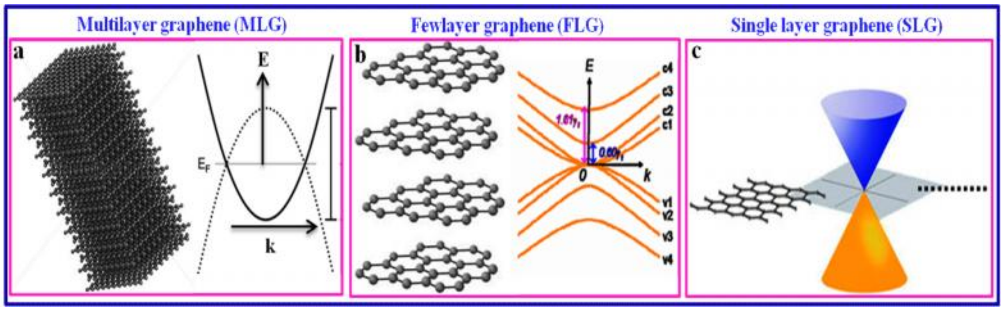

Fig.1.2. Shows the schematic and electronic band structures of graphene layers with different thickness.

The multilayer graphene (consists of multiple graphene layers) stacked to form a thickness of ~50 nm. As the number of graphene layer increases, physical property of multilayer graphene (MLG) decreases.[5] The parallel stacking of several single layer graphene combines to form Fewlayer graphene (FLG) system with thickness ranging from 3 - 6 nm. Each specific thickness of FLG shows a distinct physical property which depends on the number of graphene layers and stacking sequences (Bernal or Rhombohedral).[6] The zero band gap single layer graphene (SLG) is a one-atom thick semiconductor.

1.4 Defects on graphene surface

In recent years, researchers are very keen to modify the fascinating electrical properties of graphene, owing to its potential application.[7,8]Defect engineering is one of the methods to manipulate the electrical, chemical, and magnetic properties of graphene. Defects are typically viewed as imperfections in material, which may significantly degrade the materials properties (physical, chemical and electrical). However, nanoscale or nanosize defects in the graphene surface could be extremely useful, if they engender a novel, groundbreaking applications.[9] Collision cascade,[10] Ion irradiation (Ga^+ and Ar^+),[11,12] and plasma irradiation[13-15] are the most commonly used methods to induce surface defects in solid materials see Fig.1.3 (a-c). This defect generation will start by introducing the Stone-Wales (SW) defect on graphene then will be extended to single vacancy (SV) and divacancy (DV) shown in Fig.1.3 (d-f), which is formed when two neighboring vacancies coalesce.

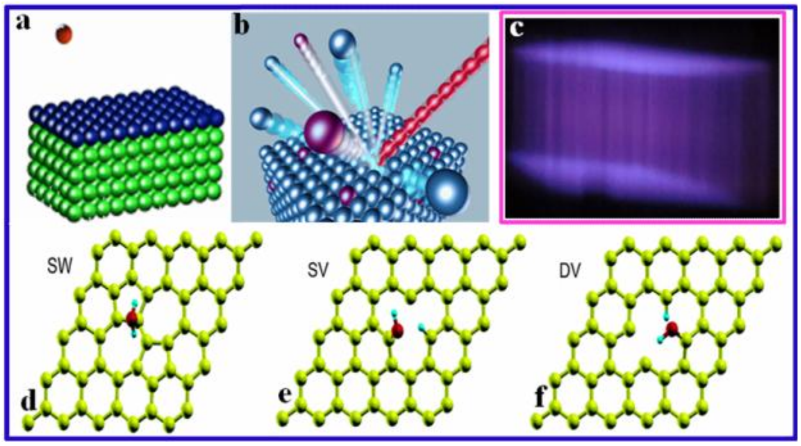

Fig.1.3. (a) Collision cascade (b) ion beam irradiation (c) plasma irradiation (d) Stone-Wales defect (e) generation of single vacancy (f) generation of divacancy.

In this thesis, we have used atmospheric plasma irradiation on graphene surface may lead to forms the different types of defects: (i) structural (sp^2-like), (ii) topological (sp^2-like) (iii) doping/functionalization and impurity (sp^2- and sp^3-like), and (iv) graphene islands or vacancies/edge type defects (non-sp^2-like),[9] which significantly affect the properties of the graphene.

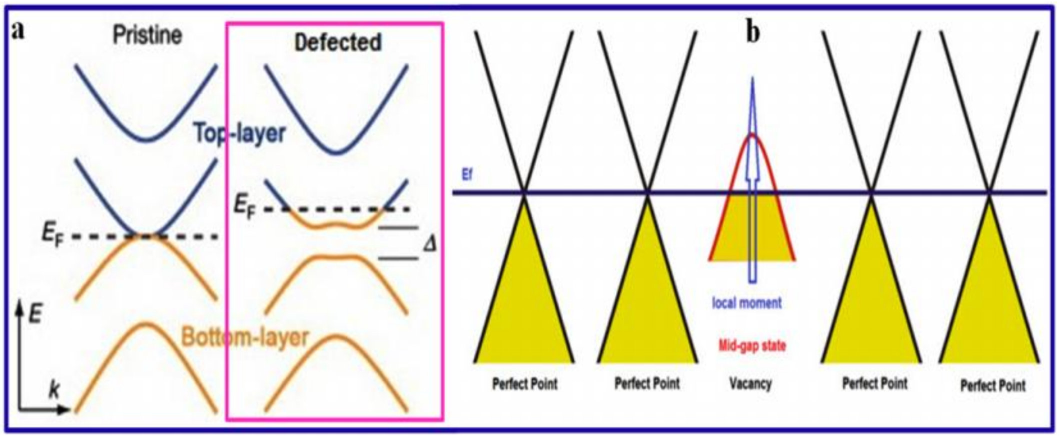

Fig.1.4. (a) Schematic of the electronic band diagram of the pristine and defected graphene layers. (b) Formation of mid gap state in the defected graphene due to the generation of vacancy.

Interestingly defective graphene opens up the bandgap due to the formation of localized mid-gap state, when Fermi energy reaches to Dirac points, due to strong hole-electron symmetry in perfect Dirac points, there is no available state for conduction electrons rather than the mid-gap state. As a result electrons drop from conduction bands to lower lying mid-gap band which is still partially filled. In other words delocalized conduction electrons of graphene are trapped into this state and become localized electrons.

1.5 **Photoresponse of the defected graphene layers**

Graphene has attracted much attention because of its extraordinary electrical and optical properties that promise a wide range of device applications.[2,16] For example, graphene photodetectors have been fabricated for high-speed optical communication,[17,18] wide band optical detection,[18] terahertz detection,[19] and other applications. The existing semiconductor photodetector range is limited by the bandgap, however, the zero bandgap graphene can be used for a wide spectral range, from ultraviolet to infrared. The high mobility of carriers in graphene supports the high-speed photodetecting, and high operating bandwidth promotes the high-speed data communications by graphene based photodetectors.[17]

The photocurrent generation in graphene-based optoelectronic devices are explained by built-in electric at the graphene-metal contacts, photothermoelectric (PTE) effects from hot carriers, and bolometric effects. The photogenerated current in graphene-based photodetectors usually occurs at the graphene-metal contacts, where an internal electric field accelerates the charge carriers to flow to contacts.[17] Metal electrodes have been deposited on the two sides of graphene layers to form built-in electric fields at the metal/graphene interfaces. The electric profile is created by the work function difference between a metal electrode and graphene: the Fermi level of two materials line up at the thermal equilibrium and then the electric field shaped up as a slope see Fig.1.5. Electron carriers in graphene, in response to incident photons, are generated and directed from the interface to the metal leads. This internal electric field will drive electrons from one material of high work function to another with low work function.

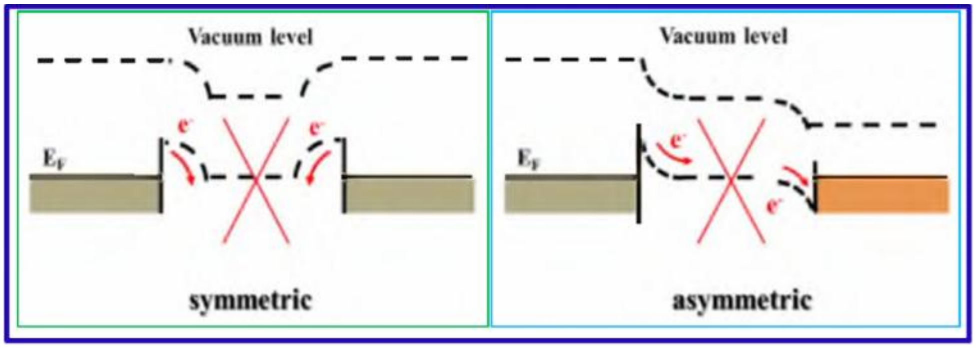

Fig.1.5. Energy band diagram showing the internal electrical field for (a) symmetric metal scheme and (b) an asymmetric metal scheme.

Fig.1.4 a shows the working mechanism of the symmetric graphene photodetectors[18,20]are realized by using only one metal material to build the two electrodes on graphene. The mirror contacts (see Fig. 1.5a) lead to an opposite direction of electron flow. In contrast, an asymmetric metal scheme can be applied by using two metals,[17] one having a higher work function than graphene (Φ ~ 4.6 eV) and the other lower, to direct electron flow in the same direction to enhance the signal under light illumination.

The entropy difference in the interface (between the graphene layers) induces PTE effects[21] which is proportional to the difference of density of states *(D(E)).* Thus, hot carriers tend to diffuse to the material with higher *D(E)* to enable the maximized entropy, which leads to electron (or hole) doped materials. Such hot carrier transport may also apply for the photocurrent generation at graphene-metal interfaces.

The photoresponse of the graphene can also explained by bolometric mechanisms can which generates electrons under light illuminations.[22] The resistance of the graphene can be changed with the enhanced local temperature, owing to the incident electromagnetic radiation. The small specific heat makes the electrons be quickly heated up, and the weak electron-phonon coupling allows the thermally decoupled electrons from the lattice.[23] Based on light illumination, resistance change by photon absorption can be detected in electrical signals, and photocurrent is then generated in the biased graphene.

We have introduced surface defects on graphene by plasma irradiation and formed the midgap band states band in the symmetric metal scheme to enhance the photoresponse behavior of graphene layers, where the plasma induced defect sites are acting as a light absorbing agent. In the later part we have attached CdSe quantum dot on graphene surface to enhance the photoresponse by generating the electron-hole pair by absorbing the incident photon.

1.6 **Self induced gate dielectric for graphene transistor**

Final part of this thesis deals with the fabrication of dielectric free graphene field-effect transistor (GFET), where the different gate architectures (back-, top- and side-gate) of GFET have their own merits and de-merits. Gate oxide layer (dielectric) is an essential part of a transistor compare to the graphene channel. Optical visualization of graphene required 300 nm of SiO_2 capping layer over the back - gate limits device performance.[2,4] Side-gated graphene FETs doesn't require any gate dielectric which degrades the channel mobility. Hahnlein *et al*. reported high transconductance of G-FETs based on side - gate configuration.[24] At the same time transconductance and current–voltage (I-V) characteristics studies of side-gate-FETs are inadequate. As compared to back-gate and side gate configurations top – gated graphene FETs (T-GFETs) have the authorized control over the electronic properties of graphene channel,[25] which is due the freedom of altering the dielectric materials and its thickness.

The performance of T-GFET device is mainly dependent on the gate dielectric materials (high dielectric constant (*k*)) such as HfO_2, Al_2O_3, and $ZrO_{2.}$ [26,27] Depositing a high-quality gate dielectrics, without introducing defects on graphene lattice is a challenging task in the transistor fabrication process.[28] Although, atomic-layer deposition (ALD) is the most common technique to deposit high-*k* dielectrics, which requires an initial functionalization process prior to the deposition. This results in breaking of chemical bonds, defective structure and even doping of unwanted impurities on the graphene lattice which can significantly affect the device mobility, on/off ratio, conductance, sub-threshold swing, and may also increase the noise level of G-FETs.[28 30] To overcome this performance degradation of graphene device, Liao *et al.* developed a concept of self – aligned gate electrodes based on Co_2Si-Al_2O_3 core – shell nanowire as a gate electrode see Fig.1.6.[31] Self – aligning method simplifies the lithographic process and also minimize the capacitance overlap.

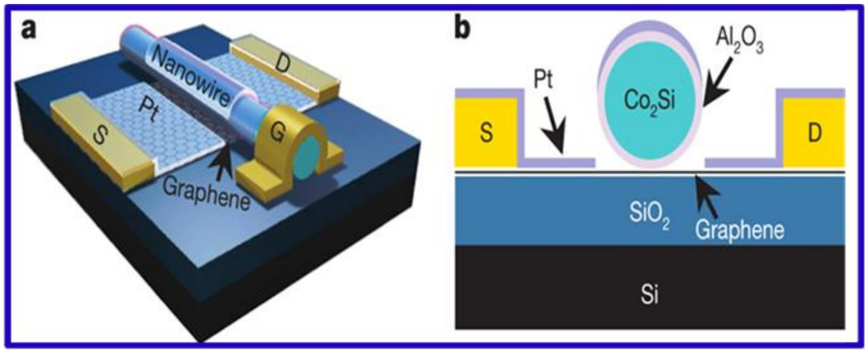

Fig.1.6. (a) Schematic of the three-dimensional view of a high-speed graphene transistor with a Co_2Si–Al_2O_3 core–shell nanowire as the self-aligned top-gate. (b) Schematic of the cross-sectional view of the device.

Here we have fabricated a new type of GFET device based on ZnO microwire as a top-gate electrode with self-induced dielectric layers. The surface adsorbed[32] oxide layer of ZnO act as dielectric layer, where the high-*k* value of ZnO provides enough capacitance to control over the active graphene channel and also defines the working area.

1.7 **Aim and Scope of the thesis**

The aim of this thesis was to investigate the thickness dependent electrical transport properties of pristine and defective graphene and its optoelectronic applications.

References

[1] A. K. Geim K. S. Novoselov. The rise of graphene *Nat. Mater.***,** 6, (2007)183-191.

[2] K. S. Novoselov, A. K. Geim, S. V. Morozov, D. Jiang, Y. Zhang, S. V. Dubonos, I. V. Grigorieva, and A. A. Firsov. Electric field effect in atomically thin carbon films *Science* 306, (2004) 666-669.

[3] K. S. Novoselov, D. Jiang, F. Schedin, T. J. Booth, V. V. Khotkevich, S. V. Morozov, A. K. Geim. Two dimensional atomic crystals *PNAS***,** 102, (2005)10451-10453.

[4] K. S. Novoselov, A. K. Geim, S. V. Morozov, D. Jiang, M. I. Katsnelson, I. V. Grigorieva, S. V. Dubonos, A. A. Firsov. Two dimensional gas of massless Dirac fermions in graphene *Nature* 438, (2005), 197-200.

[5] P. H. Tan, W. P. Han, W. J. Zhao, Z. H. Wu, K. Chang, H. Wang, Y. F. Wang, N. Bonini, N. Marzari, N. Pugno, G. Savini, A. Lombardo, and A. C. Ferrari. The shear mode of multilayer graphene *Nature Mat*.**,** 11 (2012), 294-300.

[6] M. F. Craciun, S. Russo, M. Yamamoto, and S. Tarucha. Tuneable electronic properties in graphene *Nano Today***,** 6, (2011), 42-60.

[7] Sun, P.; Zhu, M.; Wang, K.; Zhong, M.; Wei, J.; Wu, D.; Cheng, Y,; Zhu, H. Photoinduced Molecular Desorption from Graphene Films *Appl Phys Lett. 101*, (2012), 053107.

[8] Zhang, E. X.; Newaz, A. K. M.; Wang, B.; Zhang, C. X.; Fleetwood, D. M.; Bolotin, K. I.; Schrimpf, R. D.; Pantelides, S. T.; Alles, M. L. Ozone-Exposure and

Annealing Effects on Graphene-SiO_2 Transistors. *Appl. Phys. Lett. 101, (*2012), 121601.

[9] Terrones, H.; Lv, R.; Terrones, M.; Dresselhaus, M. S. The Role of Defects and Doping in 2D Graphene Sheets and 1D Nanoribbons. *Rep. Prog. Phys. 75*, (2012), 062501.

[10] Kitagawa, K.; Yamakawa, K.; Fukushima, H.; Yoshiie, T.; Hayashi, Y.; Yoshida, H.; Shimomura, Y.; Kiritani, M. Ion-Irradiation Experiment for the Fundamental Studies of Damage Evolution of Fusion Materials. *J. Nucl. Mater.**,** 133-134,* (1985) 395-399.

[11] Al-Harthi, S. H.; Kara`a, A.; Hysen, T.; Elzain, M.; Al-Hinai, A. T.; Myint, M. T. Z. Evolution of Surface Morphology and Electronic Structure of Few layer Graphene After Low Energy Ar^+ Ion Irradiation. *Appl. Phys. Lett. 101*, 2012, 213107.

[12] Zhou, Y.B.; Liao, Z. M.; Wang, Y. F.; Duesberg, G. S.; Xu, J.; Fu, Q.; Wu, X. S.; Yu, D. P. Ion Irradiation Induced Structural and Electrical Transition in Graphene. *J Chem Phys. 133, (*2010), 2347031.

[13] Cheng, Y. C.; Kaloni, T. P.; Zhu, Z. Y.; Schwingenschlögl, U. Oxidation of Graphene in Ozone Under Ultraviolet Light. *Appl. Phys. Lett. 101,* (2012), 073110.

[14] Fang, Z.; Wang, Y.; Liu, Z.; Schlather, A.; Ajayan, P. M.; Koppens, F. H. L,; Nordlander, P.; Halas, N. J. Plasmon-Induced Doping of Graphene. *ACS Nano 6*, (2012), 10222-10228.

[15] Thiyagarajan, K.; Ananth, A.; Saravanakumar, B.; Mok Y. S.; Kim, S. J. Plasma-Induced Photoresponse in Few-layer Graphene. *Carbon 73,* (2014), 25-33.

[16] P. Avouris, Z. Chen, and V. Perebeinos. Carbon based electronics Nat. Nanotechnol.**,** 2, (2007), 605-615.

[17] T. Mueller, F. Xla, and P. Avouris. Graphene photodetectors for high speed optical communications Nat. Photon., 4, (2010), 297-301.

[18] Y. Liu, R. Cheng, L. Liao, H. Zhou, J. Bal, G. Liu, L. Liu, Y. Huang, and X. Duan. Plasmon resonance enhanced multicolour photodetection by graphene Nat. Commun.**,** 2, (2011) 579.

[19] L. Prechtel, L. Song, D. Schuh, P. Ajayan, W. Wegscheider, and A. W. Holleitner. Time resolved ultrafast photocurrents and terahertz generation in freely suspended graphene Nat. Commun., 3, (2012), 646.

[20] J. H. Lee Eduardo, K. Balasubramanian, R. T. Weitz, M. Burghard, and K. Kern. Contact and edge effects in graphene devices Nat. Nanotech. 3, (2008), 486-490.

[21] X. Xu, N. Gabor, J. Alden, A. van der Zande, and P. McEuen. Photo-thermoelectric effect at a graphene interface jucntion Nano Lett. 10, (2010), 562-566.

[22] J. Yan, M. H. Kim, J. Elle, A. Sushkov, G. Jenkins, H. Milchberg, M. Fuhrer, and H. Drew. Dual-gated Bilayer graphene hot-electron bolometer Nat. Nanotechnol. 7, (2012), 472-478.

[23] J. Viljas and T. Heikkila. Electron-phonon heat transfer in monolayer and Bilayer graphene Phys. Rev. B 81, (2010), 245404.

[24] Hahnlein, B.; Handel, B.; Pezoldt, J.; Topfer, H.; Granzner, R.; Schwierz, F. Side-gate graphene field-effect transistors with high transconductance *Appl. Phys. Lett.* 101, **(2012),** 093504.

[25] Meric, I.; Han, M. Y.; Young, A. F.; Ozyilmaz, B.; Kim, P.; Shepard, K. Current saturation in zero-bandgap, top-gated graphene filed-effect transistors *Nat. Nanotechnol.* 3,(2008), 654-659.

[26] Kim, S.; Nah, J.; Jo, I.; Shahrjerdi, D.; Colombo, L.; Yao, Z.; Tutuc, E.; Banerjee, S. K. Realization of a high mobility dual-gated graphene field-effect transistor with Al_2O_3 dielectric *Appl. Phys. Lett.* 94, (2009), 062107.

[27] Liao, L.; Duan, X. Graphene-dielectric integration for graphene transistors *Mater. Sci. Eng. R* 70, (2010), 354-370.

[28] Liao, L.; Bai, J.; Lin, Y.C.; Qu, Y.; Huang, Y.; Duan, X. High-performance top-gated graphene-nanoribbon transistors uning Zirconium oxide nanowires as high-dielectric-constant gate dielectrics *Adv. Mater.* 22, (2010), 1941-1945.

[29] Lin, Y.M.; Chiu, H.Y.; Jenkins, K. A.; Farmer, D. B.; Avouris, P.; Valdes-Garcia, A. Dual-gated graphene FETs with f_T of 50 GHz *IEEE Electron Device Lett.* 31, (2010), 68.

[30] Lemme, M. C.; Echtermeyer, T. J.; Baus, M.; Kurz, H. A graphene field-effect device *IEEE Electron Device Lett.* 28, (2007), 282-284.

[31] Liao, L.; Lin, Y-C.; Bao, M.; Cheng, R.; Bai, J.; Liu, Y.; Qu, Y.; Wang, K- L.; Huang, Yu.; Duan, X. High-speed graphene transistors with a self-aligned nanowire gate Nature 467, (2010), 305-308.

[32] Liao, Z-M.; Lv, Z-K.; Zhou, Y-B.; Xu, J.; Zhang, J-M.; Yu, D-P. The effect of adsorbates on the space-charge-limited current in single ZnO nanowires Nanotechnology 19, (2008), 335204.

CHAPTER II

Device Fabrication and Measurement Setup

In this chapter I present the general overview of the steps involved in the graphene layer preparation, device fabrication, processing, measurements and its application.

2.1 Preparation of graphene layers

We can prepare the graphene layers from the available graphites sources, such as Natural (powders), Kish and Highly Oriented Pyrolytic Graphite (HOPG), among these graphite sources, HOPG holds the highest crystal quality, high chemical purity and solidity for large size see Fig.2.1a, make them as a primary choice for the studies. In this thesis, all presented measurements, samples are from HOGP.

Prior to the graphene deposition, the wafer consists of highly doped silicon, covered by 300 nm of SiO_2 was cleaned with acetone, isopropanol and water successively in an ultrasonic bath for 2 min and then dried in N_2 gas, which removes the impurities present over the surface.

Graphene flakes are produced by micromechanical cleavage method, developed by Novoselov et.al in 2004, which is still a fast and the most effective way to produce high quality (defect free) graphene samples with different thickness[2] (SLG, BLG, TLG, FLG and MLG). The HOPG flakes are distributed on the scotch tape, which is then folded and unfolded for numerous times to cleave the graphene from graphite Fig.2.1b. The flake size depends on the number of folding events; five to ten folding is a good number: if the tape is folded less often, the graphite is not cleaved enough, too many folding affects the size of the flake and leaves more glue residuals.

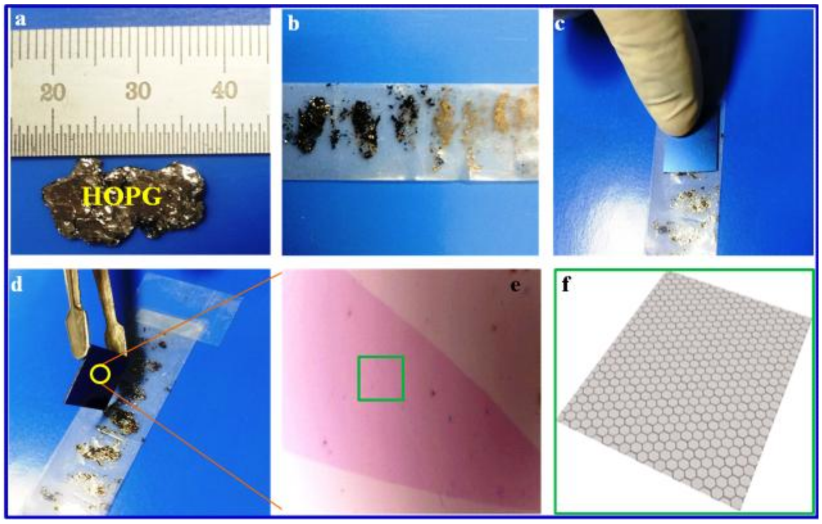

Fig.2.1. Micromechanical exfoliation of graphene layers (a) Digital photography of HOPG, (b) graphite flakes on scotch tape (c and d) transferring of graphene to SiO_2 (300 nm)/Si substrate (e) optical microscopy image of graphene (f) schematic of the atomic structure of graphene.

The cleaned SiO_2 (300 nm)/Si substrate is placed on top of the tape and gently pressed over the substrate with tweezers or with a finger (Fig.2.1c) and removed carefully (Fig.2.1d). Now the graphene contain substrate was cleaned with acetone and isopropanol in an ultrasonic bath for 2 min and then dried in N_2 gas, which ensures the chosen flakes was attached well to the surface. An optical microscope was used to locate the optimum graphene samples on the substrate see Fig.2.1e.

2.2 Thickness determination of graphene layers

After transfer process the SiO_2 (300 nm)/Si substrate is covered by many graphene flakes with different thicknesses. The thickness of the graphene flakes is evaluated through optical microscopy (OM- color contrast), [1-3] atomic force microscopy

(AFM) and Raman spectroscopy. Fig.2.2a shows the optical microscopic image of the graphene flakes contains single layer garaphene (SLG-blue arrow), few layer graphene (FLG- green arrow) and multilayer graphene (MLG-red arrow). Here the optimization was done by the color contrast method, when the flake thickness increases the color seen under the optical microscope changes from purple to dark purple, and then to green and finally to yellow. AFM image along with the line profile is shown in Fig.2.2b, where the unambiguous flake thickness can be determined by the height difference between the substrate and the graphene flake[1,4]. Raman spectrum of graphene flake is shown in Fig.2.2c, where the spectrum features differ with respect to flake thickness, the 2D peak (~2700 cm^{-1}) and full width half maximum (FWHM) are serving as a direct evidence for the determination of graphene flake thickness.[4]

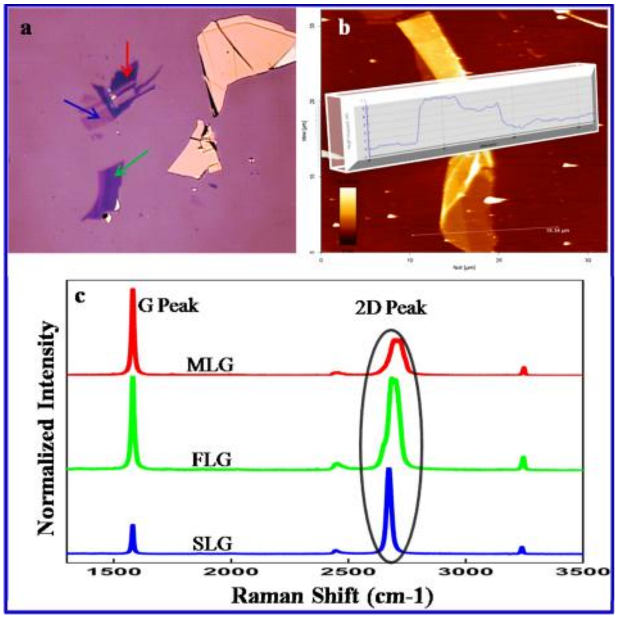

Fig.2.2. (a) Optical microscopic image of the graphene flakes contains single layer garaphene (SLG-blue arrow), few layer graphene (FLG- green arrow) and multilayer graphene (MLG-red arrow). (b) AFM image of a graphene flake along with the line profile. (c) Raman spectrum of graphene layers.

2.3 Electrode Fabrication- Photolithography

Electrodes were patterned by conventional photolithography (Mask Aligner MDA-400M, MIDAS) process. After thickness determination the positive photo-resist (AZ 5214) was spin coated and chromium (Cr) mask was used to form the desire pattern over the graphene flakes. A 100 nm, thick gold electrode was formed by thermal evaporation, and the lift-off process was done using acetone see Fig.2.3a-d, for the process diagram. After lift-off process, the device was annealed at 250 °C in Ar/H_2 atmosphere for 30 min to improve the adhesion of the gold electrodes with graphene flake as well as to remove the resist residuals.[5]The optical and field emission scanning electron microscopy (FESEM) image of the fabricated device with MLG is shown Fig.2.3e and f respectively.

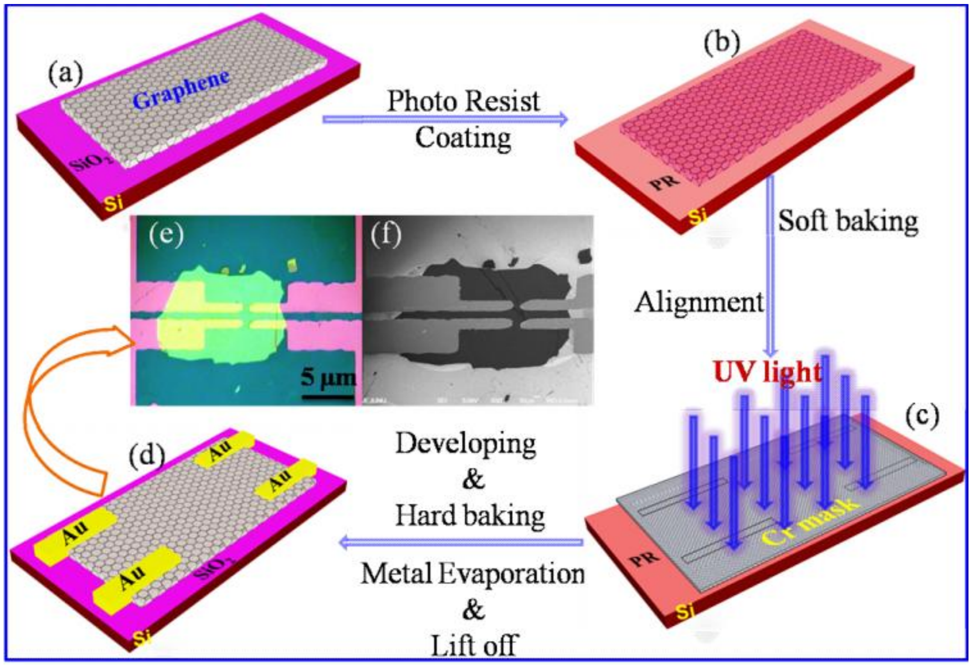

Fig.2.3. Process flow diagram of photolithography.

2.4 Defect generation on graphene layers-Plasma irradiation

We have used dielectric barrier discharge (DBD) plasma reactor to induce defects on graphene (MLG, FLG and SLG) surface. Prior to plasma exposure, electrodes were covered with epoxy resin and dried at 150°C for 30 min in air to prevent electrode oxidization and damage. The graphene device was exposed to a homemade atmospheric plasma reactor (shown in Fig.2.4a) for different time period (depend on the flake thickness) in an Ar atmosphere with the flow rate of 60 sccm at a pressure of ~1 Torr, where the applied voltage is 130 V and the frequency is 400 Hz. The photograph of the generated Ar plasma based on the above condition is shown in Fig.2.4c. The effect of plasma irradiation on the graphene (here FLG) surface was clearly visible in the optical microscope images shown in Fig.2.4b and d (before and after plasma irradiation, respectively).

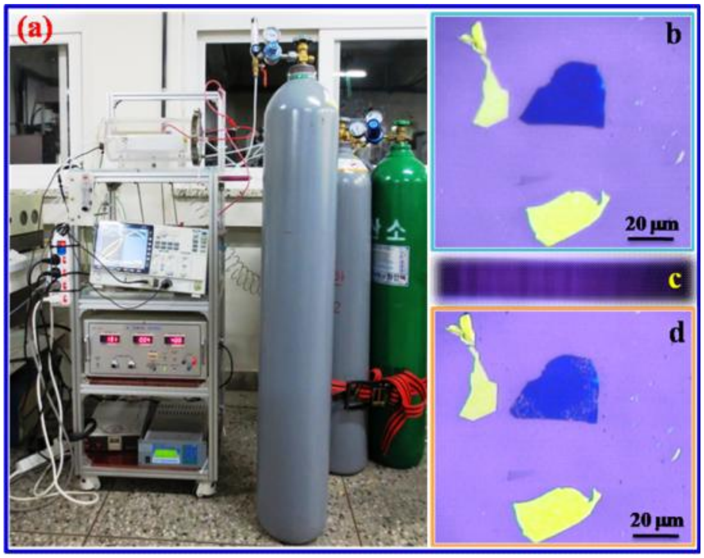

Fig.2.4. (a) Digital photograph of the DBD plasma reactor. (b and d) optical microscopic images of FLG graphene before and after plasma irradiation respectively. (c) Photograph of the generated argon plasma.

2.5 Synthesis of ZnO Microwires

ZnO microwires were synthesized through the vapor transport method in a horizontal tube furnace using ZnO and the carbon powder mixture as a source material. The schematic of the experimental setup for growth of ZnO microwires is shown in Fig.2.5a. The mixture of ZnO and graphite with 1:1 weight ratio was loaded in alumina boat and placed at the midpoint of a 1 m long quartz tube. Argon gas with high purity was introduced through one side of the furnace and water bubbler was connected to the other side of the quartz tube. The mixture was heated to 1100 °C at 360 °C/h rate under a constant argon flow rate of 500 sccm. When the temperature reaches 800 °C oxygen gas was also introduced with a flow rate of 25 sccm. The furnace was maintained under these conditions for 30 min and then cooled to room temperature at a rate of 6 °C/min. ZnO fine wires were found to grow on the upstream end of the alumina boat. The surface morphology of ZnO fine wires was studied using FE-SEM (JEOL, JSM 6700F) is shown in Fig.2.5b.

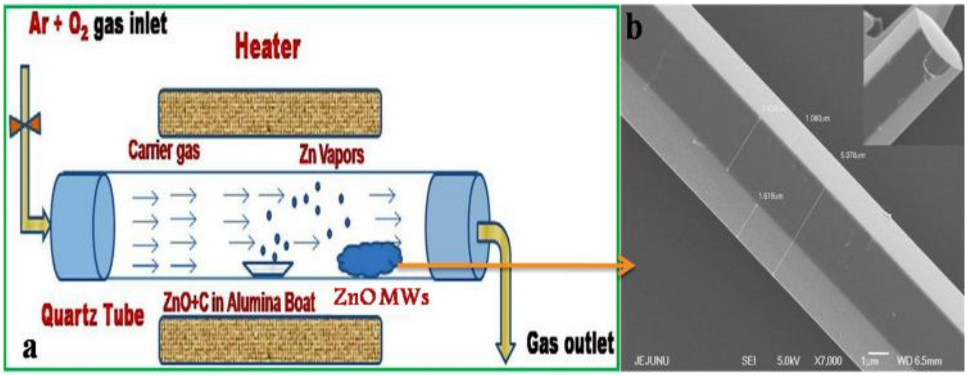

Fig.2.5. (a) The schematic of the experimental setup for growth of ZnO microwires. (b) FESEM image of ZnO microwires where the inset is the enlarged view of the edge part of ZnO microwire shown hexagonal structures.

2.6 Measurement units

2.6.1 Low temperature measurement

The electrical transport measurements depend on the low-temperature presented in this thesis have been performed with four probes using a closed-cycle refrigerator system (CKW-21, Sumitomo-Japan). Fig.2.6a shows the schematic of the measurement setup, which allows us to characterize the devices at temperature in the range of 15-300 K using a Keithley 2182A nanovoltmeter and Keithley 2400 source meter. Here the low temperature was achieved through ^{4}He gas flow.

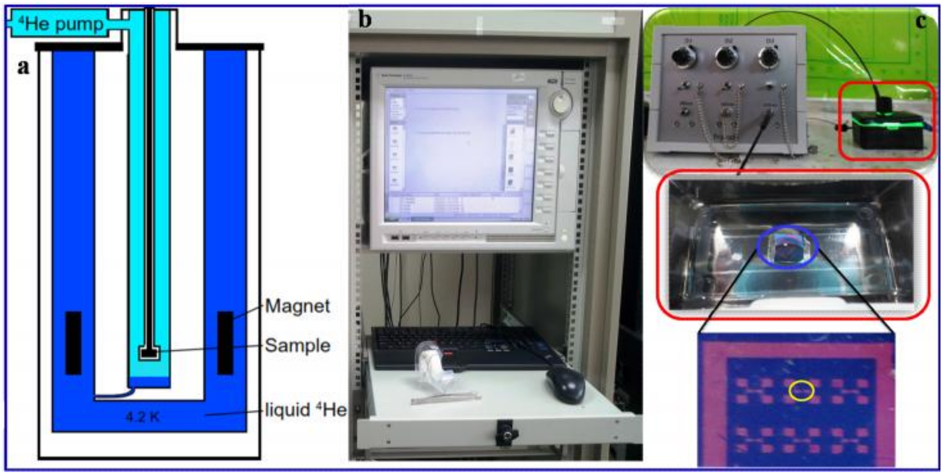

Fig.2.6. (a) Schematic of the closed-cycle refrigerator system. (b) Photo of the semiconductor parameter analyzer. (c) Experiment setup for the photocurrent measurement.

2.6.2 Electrical and photocurrent measurement

Electrical and photocurrent measurements were carried out using a semiconductor parameter analyzer (Agilent, B 1500A), combined with a Prizmatix multi-wavelength LED light source see Fig.2.6b and c respectively. For the photocurrent measurement the whole device was illuminated with different wavelength.

References

[1] Z. H. Ni, H. M. Wang, J. Kasim, H. M. Fan, T. Yu, Y. H. Wu, Y. P. Feng, and Z. X. Shen. Graphene thickness determination using reflection and contrast spectroscopy *Nano Lett.* 7, (2007), 2758-2763.

[2] G. Venugopal, and S. J. Kim. Temperature dependent transfer characteristics of graphene field effect transistors fabricated using photolithography *Curr. Appl Phys.* 11, (2011), S381-S384.

[3] P. Blake, E. W. Hill, A. H. Castro Neto, K. S. Novoselov, D. Jiang, R. Yang, T. J. Booth, and A. K. Geim, Making graphene visible *Appl Phys. Lett.* 91, (2007), 063124.

[4] Thiyagarajan K, Saravanakumar B, Mohan R, Kim SJ. Thickness dependent electrical transport properties of graphene. Sci Adv Mater 5, (2013), 542-548.

[5] J. H. Chen, C. Jang, S. Xiao, M. Ishigami, and M. S. Fuhrer, Intrinsic and extrinsic performance limits of graphene devices on SiO_2 *Nat. Nanotechnol.* 3, (2008)**,** 206-209.

CHAPTER III

Thickness Dependent Electrical Transport Properties of Graphene

3.1 Introduction

The properties of graphene entirely differs, with respect to the flake thickness or layers, where the graphene family is generally classified into five major groups, such as multilayer, fewlayer, trilayer, bilayer and single layer. One of the important parameters that determines the electronic transport in a material is the temperature. In any material, energy associated with temperature causes the atoms to vibrate, as electrons travel through the material. They can bounce off these vibrating atoms, giving rise to electrical resistance.[22] This electrical resistance is intrinsic to the material which can be eliminated when it is cooled to absolute zero temperature. Understanding and scheming of this resistance is the key to develop high-performance devices.

In this chapter, we investigate the thickness dependent electrical transport properties of the multilayer, few-layer and single layer graphene and analyzed them based on the optical contrast, Raman spectrum, AFM and resistance versus temperature (R-T) characteristics. An ideal defect- free graphene with thickness ranging from few tens of nanometer to sub nanometer is taken for the temperature dependence resistance (R (T)) measurement. The results were interpreted as a metallic to semiconducting transition as a function of flake thickness.

3.2 Electrical transport properties of multilayer graphene

The stacking of number of graphene layers, one above the other with perfect periodicity, forms multilayer graphene (MLG) and the thickness ranges from 10-50 nm. As the number of graphene layer increases, the physical property of MLG decreases, eventhough, MLG system has the potential to overcome curbing effect of substrate, a noise screener in electrical transport, [1] the high carrier density and resonant frequency, which allow us to use in photonics to manipulate the terahertz waves. It's necessary to analysis resistance behavior of MLG at low temperature.

For the details of device fabrication please refer section 2.1 and 2.3. Thickness of the graphene flake can be determined by the light reflectance method, which is based on optical contrast between graphene and the underlying substrate.[2-4]Fig.3.1a shows the optical microscopic image of a graphene flake with greenish color on SiO_2/Si substrate, suggest that the flake, consist of many numbers of graphene layers, which might be MLG, and the FESEM observation similar flake is shown in Fig.3.1b**.** The most direct way to identify the thickness or number of graphene layers in a flake is AFM analysis.[2] In the present discussion, the height difference between the graphene surface and the underlying substrate was considered as the thickness of the sample. Fig.3.1c**,** shows the AFM image of the MLG and height matching profile (Fig.3.1 d and e) verifies that the thickness of MLG varies from 13 to 21 nm. This asymmetric nature on the surface of MLG affects its electrical transport property.

Raman spectrum of MLG is shown in Fig.3.1f**,** the G peak appears at 1583 cm^{-1}, and the 2D peak centered at 2707 cm^{-1} is considerably broader and fitted with multiple peaks shown in the inset of Fig.3.1f. Due to the successive addition of graphene layers in MLG lowers the symmetric nature of the sample. As a result, 2D peak splits into several overlapping modes. The resultant changes in the 2D peak help us to evaluate the electronic structure of the multilayered graphene.[5] The full width at half maximum (FWHM) of 2D peak and the intensity ratio between G peak and 2D peak (I_{2D}/I_G) are used to determine sample thickness. From the obtain Raman spectrum gives the values for the FWHM of 2D peak is ~ 59 and I_{2D}/I_G value is 0.43, which is suggesting that the flake is MLG.[6]

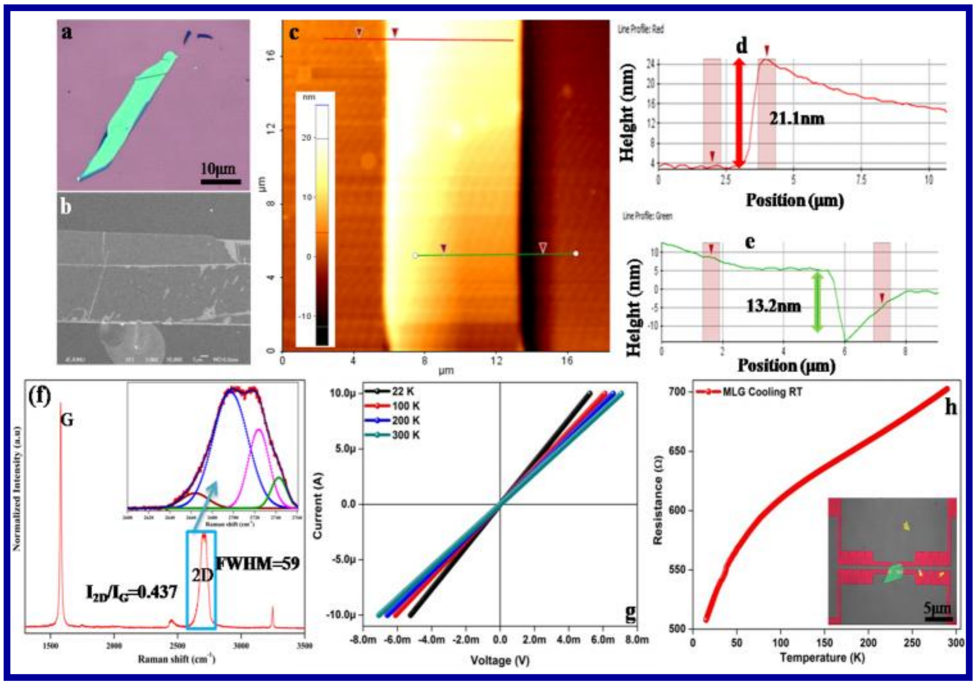

Fig.3.1. (a) Optical microscopic image of MLG (b) FESEM image of MLG (c) AFM image of a typical multilayer graphene sample on SiO_2 /Si substrate. (d) Height matching profile to the red line in (c) shows the thickness of 21.1 nm. (e) Height matching profile to the green line in (c) shows the thickness of 13.2 nm. (f) Raman spectra MLG Sample, where the inset is the enlarged view of the 2D peak which is fitted with multiple peaks. (g) Temperature dependent I-V characteristics of MLG. (h) R-T characteristics of MLG shows clear metallic nature of the sample.

The current - voltage (*I*-*V*), and R (T) measurement was performed under the vacuum conditions on clean samples to minimize adsorption/desorption of molecules due to temperature - dependent effects. The current biased temperature dependent current - voltage (*I*-*V*) characteristic of MLG is shown in Fig.3.1g. The linear *I*-*V* curve indicates the Ohmic contact has been formed between the gold electrode and the graphene channel. The MLG with thickness ranging from 20 to 50 nm sample shows metallic like behavior (resistance-decreases when the temperature decreases) in the R (T) measurement, which is shown in Fig.3.1h. This metallic behavior arises due to the permanent overlapping of bands[7] (electron and hole) in MLG, splitting of π-bands owing to the interface interactions of graphene layers and stacking sequences of MLG.[8] The 2D peak of the Raman spectrum (inset of Fig.3.1f) is fitted with multiple peaks because of the π-bands splitting and the asymmetric surface topography (Fig.3.1c) leads to the electronic transition from 2D to 3D (bulk) in MLG.[8]

3.3 Electrical transport properties of fewlayer graphene

The parallel stacking of several single layer graphene combines to form Fewlayer graphene (FLG) system with thickness ranging from 3 - 6 nm. Each specific thickness of FLG shows a distinct physical property which depends on the number of graphene layers and stacking sequences (Bernal or Rhombohedral).[9] Trilayer graphene (TLG) consists of three graphene layers, which are the thinnest in FLG family and the electrical property of TLG mainly rely on the stacking arrangements of graphene layers.[10] Bernal (or ABA)-stacked Trilayer graphene (B-TLG) is semi-metallic due to the electron and hole band shift towards lower energy level with respect to the external electric field.[9] The ABC (or

Rhombohedral) - stacked trilayer graphene (r-TLG) is insulating with an intrinsic (spontaneous) gap of ~ 6 meV.[11] Here we show the existence of semi-conducting behavior in FLG system based on the R-T curve behavior.

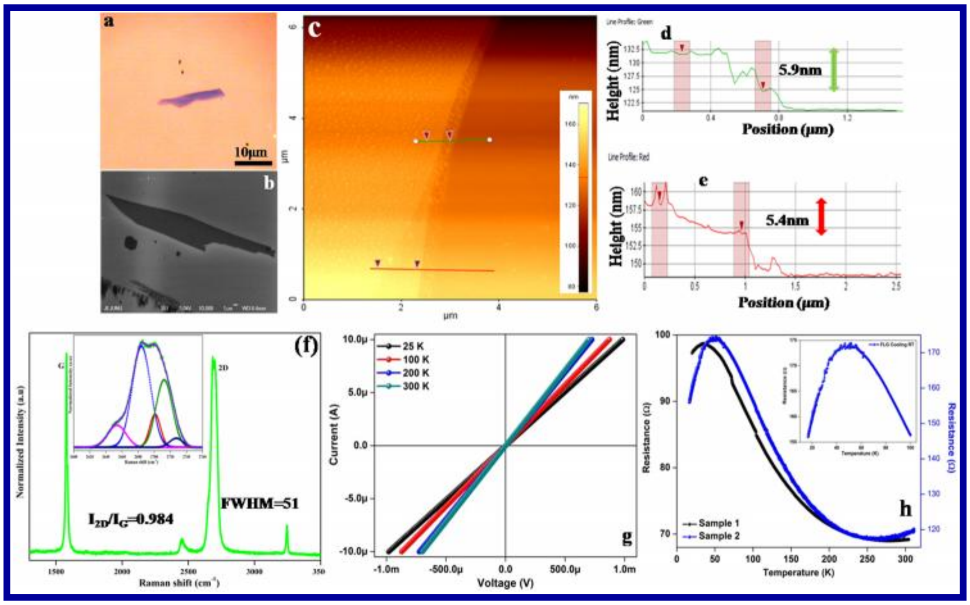

Fig.3.2. (a) Optical microscopic image of FLG (b) FESEM image of FLG (c) AFM image of a typical FLG sample on SiO_2 /Si substrate. (d) Height matching profile to the green line in (c) shows the thickness of 5.9 nm. (e) Height matching profile to the red line in (c) shows the thickness of 5.4 nm. (f) Raman spectra FLG Sample, where the inset is the enlarged view of the 2D peak which is fitted with multiple peaks. (g) Temperature dependent I-V characteristics of FLG. (h) R-T characteristics of FLG shows mixed face of semiconducting and metallic nature.

The optical and FESEM image of the FLG is shown in Fig.3.2a and b**.** The blue color in the optical image indicates that the flake contains of a few layers of graphene. The AFM result of FLG is shown in Fig.3.2c along with height matching profiles in Fig.3.2d and e**.** The reduction in the number of layers in FLG drops its thickness to ~ 6 nm which is obtained through height matching profiles. The thickness all along the FLG sample was more uniform compared to MLG samples (Fig.3.2c**)**.

Fig.3.2f**,** is the Raman spectrum of few layer graphene. The G peak of FLG at 1583 cm^{-1} corresponds to the stretching vibrations of in plane carbon atoms present in the Brillouin zone.[12] The inset in Fig.3.2f shows the enlarged and fitted 2D peak of FLG emerged at 2693 cm^{-1} with the FWHM of ~51cm^{-1} and I_{2D}/I_G ratio of 0.98, which conform that the flake contains only few layers of graphene.

Similar to MLG the FLG also shows linear characteristics in temperature dependent I-V, is presented in Fig.3.2f, which shows the linear behavior in all studied temperature. The semi conducting behavior is becoming clearly visible when the sample thickness decreased to few nanometers (about ~ 3 to 6 nm) where the interlayer interaction between graphene layers decreases. The semiconductor – metallic behavior (c-axis like behavior) transistion was observed in the FLG, the low temperature region see Fig.3.2h, which is due to the tunneling of electrons between graphene planes.[13, 14]When the interlayer symmetry of FLG is broken by the the external electric field, which leasds to the shifts electron and hole bands towards the lower energy level.[9, 7] Top of the valence band and bottom of the conduction band overlaps and causes transition from semiconductor – metallic. The insets of Fig.3.2h show the transition points of FLG samples. We observation shows that the transition point in FLG significantly changes with sample thickness.

3.4 Electrical transport properties of single layer graphene

The single layer graphene (SLG) is a fascinating one-atom thick, semiconductor with zero band gap. This part of the chapter serves as the evidence for the existence semi-conducting nature in SLG. The SLG with high transmittance see Fig.3.3a, was located by optical microscopy and further visualized through FESEM (Fig.3.3b). The AFM topographic and the corresponding height matching profiles of SLG are shown in Fig.3.3c, and d. In theory, the thickness of SLG is 0.34 nm, however the measured height profile revealed that the thickness is about 0.65 nm due to the interaction between graphene and SiO_2. Presence of ambient species like nitrogen, oxygen, argon, and water molecules always leads to higher values.[15] The surface roughness of graphene is more significant because the asymmetric surface causes scattering of charge carriers which may affect the electrical transport property of the device.[15]

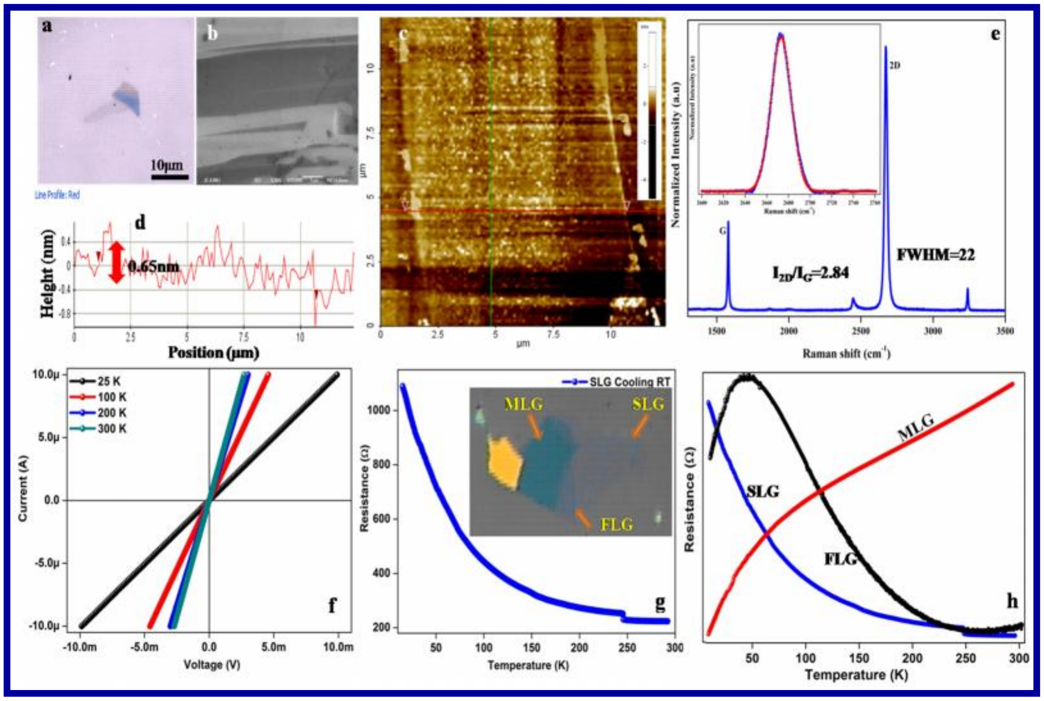

Fig.3.3. (a) Optical microscopic image of SLG (b) FESEM image of SLG (c) AFM image of a typical SLG sample on SiO_2/Si substrate. (d) Height matching profile to the red line in (c) shows the thickness of 0.65 nm. (e) Raman spectra SLG Sample, where the inset is the enlarged view of the 2D peak, which is fitted with only one peak. (f) Temperature dependent I-V characteristics of SLG. (g) R-T characteristics of SLG show clear semiconducting behavior. (h) Metallic to semiconducnting transition of graphene layers as a function of flake thickness.

Raman spectrum of single layer graphene is shown in Fig.3.3e, the G peak and the 2D peaks are centered at 1583 cm^{-1} and 2673 cm^{-1} respectively. The 2D peak of SLG is well fitted with single Lorentzian peak see the inset of Fig.3.3e. This sharp 2D peak is well distinguished from FLG and MLG. It shows that when the thickness of graphene decreases (MLG to SLG) the FWHM of the 2D peak decreases along with the increase in the I_{2D}/I_G ratio, these changes alters the 2D peak position, shape, and its relative intensities, which are sensitive to the number of graphene layers, which help us to calculate the sample thickness.

The temperature dependent *I-V* characteristic of SLG is presented in Fig.3.3f, which shows the linear characteristics for all studied temperature. Voltage drops are observed when the sample reaches room temperature, which is mainly due to the scattering of charge carriers. The sub nanometer thick SLG shows semi conducting behavior in R (T) measurement, which is presented in Fig.3.3g. This semi-conducting behavior arises due to the absence of inter layer interactions, and decrease in the number of interfaces.[14] The charge carriers present in the graphene surface are responsible for this semi conducting behavior.[16] The fabricated graphene device shows the metallic to semiconductor transition with respect to sample thickness in low temperature electrical transport (R (T) measurement see Fig.3.3h. FLG with thickness ~ 6 nm samples shows the *c-axis* characteristic in (R (T) measurement due to the tunneling of electrons between the graphene layers. This layer dependent electrical transport property of graphene makes them a promising candidate for the future electronic applications. The semiconducting behavior of SLG in R (T) measurement suggests that each graphene layer inside the graphite flakes are semiconductors.

3.5 Conclusions

We have studied the resistance of a graphene sample as a function of flake thickness. The graphene sample thickness ranging from sub nanometer (~ 0.65 nm) to a few tens of nanometer (~ 50 nm) with an active channel area in several μm^2. The electrical transport phenomenon of fabricated graphene devices showed the transition of metallic (MLG) to semiconductor (SLG) behavior with respect to their thickness. The c-axis characteristic (semi conducting to metallic) was observed only in FLG, due to the tunneling of electrons between the graphene interlayers. The obtained result clearly indicates that the resistance of an ideal, defect-free graphene samples are sensitive to the number of graphene layers. The R-T curve behavior of the graphene samples suggests that the R (T) measurement is another way of identifying graphene sample thickness.

References

[1] M. A. Kuroda, J. Tersoff, and G. J. Martyna. Nonlinear screening in multilayer graphene systems *Phys. Rev. Lett.* 106, (2011),116804.

[2] Z. H. Ni, H. M. Wang, J. Kasim, H. M. Fan, T. Yu, Y. H. Wu, Y. P. Feng, and Z. X. Shen. Graphene thickness determination using reflection and contrast spectroscopy *Nano Lett.* 7, (2007), 2758-2763.

[3] P. Blake, E. W. Hill, A. H. Castro Neto, K. S. Novoselov, D. Jiang, R. Yang, T. J. Booth, and A. K. Geim, Making graphene visible *Appl Phys. Lett.* 91, (2007), 063124.

[4] L. Gao, W. Ren, F. Li, and H. M. Cheng, Total color difference for rapid and accurate identification of graphene *ACS Nano* 2, (2008), 1625-1633.

[5] A. C. Ferrari, J. C. Meyer, V. Scardaci, C. Casiraghi, M. Lazzeri, F. Mauri, S. Piscanec, D. Jiang, K. S. Novoselov, S. Roth, and A. K. Geim, Raman spectrum of graphene and graphene layers *Phys. Rev. Lett.* 97, (2006), 187401.

[6] L. M. Malard, M. A. Pimenta, G. Dresselhaus, M. S. Dresselhaus, Raman spectroscopy in graphene *Physics Reports* 473, (2009), 51-87.

[7] M. Koshino, Interlayer screening effect in graphene multilayer with ABA and ABC stacking *Phys. Rev. B* 81, (2010),125304.

[8] T. Ohta, A. Bostwick, J. L. McChesney, T. Seyller, K. Horn, and Eli Rotenberg, Interlayer interaction and electronic screening in multilayer graphene investigated with angle-resolved photoemission spectroscopy *Phys. Rev. Lett.* 98**, (**2007), 206802.

[9] M. F. Craciuna, S. Russob, M. Yamamotoc, and S. Taruchac, Tunable electronic properties in graphene *Nano Today* 6, **(**2011), 42-60.

[10] Amir Yacoby, Graphene: Tri and tri again *Nature Phy.* 7, (2011), 925-926.

[11] W. Bao, L. Jing, J. Velasco Jr, Y. Lee, G. Liu , D. Tran, B. Standley, M. Aykol, S. B. Cronin, D. Smirnov, M. Koshino, E. McCann, M. Bockrath, and C. N. Lau. Stacking-dependent band gap and quantum transport in trilayer graphene *Nature Phy.* 7, (2011), 948-952.

[12] Y. Hao, Y. Wang, L. Wang, Z. Ni, Z. Wang, R. Wang, C. K. Koo, Z. Shen, and John T. L. Thong, Probing layer number and stacking order of few-layer graphene by raman spectroscopy *Small* 6, (2010), 195-200.

[13] G. Venugopal, M. H. Jung, M. Suemitsu, and S. J. Kim, Fabrication of nanoscale three-dimensional graphite stacked-junctions by focused-ion-beam and observation of anomalous transport characteristics *Carbon* 49, (2011), 2766-2772.

[14] N. Garcıa, P. Esquinazi, J. Barzola-Quiquia, and S. Dusari, Evidence for semiconducting behavior with a narrow band gap of Bernal graphite *New J. Phys.* 14, (2012), 053015.

[15] M. Ishigami, J. H. Chen, W. G. Cullen, M. S. Fuhrer, and E. D. Williams, Atomic structure of graphene on SiO_2 *Nano Lett.* 7, (2007), 1643-1648.

[16] S. V. Morozov, K. S. Novoselov, M. I. Katsnelson, F. Schedin, D. C. Elias, J. A. Jaszczak, and A. K. Geim, Giant intrinsic carrier mobilities in graphene and its bilayer *Phys. Rev. Lett.* 100, (2008), 016602.

CHAPTER IV

Defect-induced Metallic-to-Semiconducting Transition in Multilayer Graphene

4.1 Introduction

The stacking of number of graphene layers, one above the other with perfect periodicity, forms multilayer graphene (MLG) which lacks in the physical significance due to higher thickness. Temperature dependence resistance (R (T)) measurement confirms that the ideal defect- free MLG is metallic in nature (see Section 3.2 in chapter 3), which is owing to the band overlapping, π-bands splitting, asymmetric surface topography and stacking sequences.

In this chapter, we show that the MLG with morphological disorder exhibits a metallic-to-semiconductor transition in the resistance as a function of temperature (R (T)). The pristine MLG was metallic; however, plasma irradiation induces defects, such as including vacancies, voids, and nanoholes, which altered the resistance of the MLG. The resulting defect-rich MLG follows plasma treatment exhibited a semiconductor-like temperature dependence of the resistance.

4.2 Experimental Section

The MLG exfoliation, and electrode fabrication details please refer chapter 2 sections (2.1and 2.3) where the thickness approximation was shown in Fig.4.1a-c. After the metal (Au) deposition the MLG devices were annealed at 250°C in an Ar/H_2

atmosphere for 30 min to improve the adhesion of the gold electrodes to the graphene flakes and to remove the residual resist. Prior to plasma exposure, the electrodes were covered using a thin layer of epoxy resin, and dried at 150°C for 30 min in the air to prevent oxidization and damage to the electrodes.

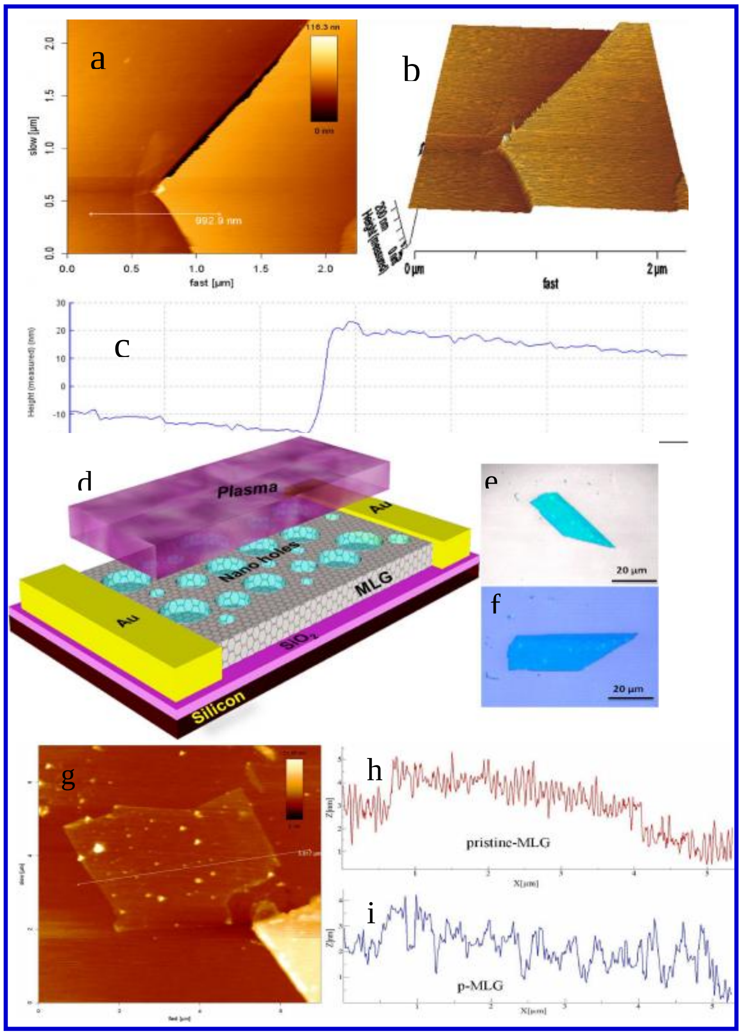

Fig.4.1. AFM analysis: (a) 2D image of pristine-MLG and (b) 3D image of (a). (c) The line profile image corresponding to the *x*-axis of (a) which shows the thickness of ~ 35 nm. (d) Schematic of diagram nanoholes multilayer graphene device. Optical microscopy image of (e) pristine- MLG and (f) p- MLG. (g) The two-dimensional AFM image of the MLG. (h) and (i) Line profile image corresponding to the *x*-axis of (d) corresponds to pristine- MLG and p-MLG.

Then the MLG device was exposed to a custom-made atmospheric plasma reactor (see Fig.2.4) in Ar atmosphere with a flow rate of 60 sccm at a pressure of ~1 Torr for 10 min. The plasma irradiation induces surface defects and also generates nanoholes which is schematically shown in Fig.4.1d. We compare the OM image of the pristine-MLG (before) and p-MLG (after) plasma irradiation (see Fig. 4.1e and f), but there are no obvious changes observed. Longer plasma irradiation on graphene surface leads to significant defect generation and then to etching, which causes the sample thickness, in case of MLG the thickness variation is in the sub nanometer range see Fig.4.1g –i.

To characterize the defects nature and its type, we carry out Raman spectroscopy measurements using a 514 nm Ar+ laser as an excitation source (Horiba Jobin Yvon, LabRAM HR800). Nanoview surface profile analysis (Nano System Co., Ltd.) was employed to visualize the surface defects. Field-emission scanning electron microscopy (FESEM) (JEOL, JSM-6700F) was used to characterize the structural changes in the plasma-treated samples. Room-temperature electrical measurements were carried out using a semiconductor parameter analyzer (Agilent, B 1500A see Fig.2.6b). Low-temperature electrical transport measurements of the devices were performed using a closed-cycle refrigerator system (CKW-21, Sumitomo-Japan see Fig.2.6a), allowing us to characterize the devices at temperatures in the range of 15–300 K using a Keithley 2182A nanovoltmeter and a Keithley 2400 source meter.

4.3 Results and Discussion

In general the defect-rich graphene sheets exhibit significant differences in their physicochemical properties compared with pristine graphene.[1] The thickness of the flakes and the process parameters determine the defect density. Plasma irradiation induces a number of different types of defects on the surface of the MLG [2] however, defects are typically generated from existing Stone–Thrower–Wales (STW) defects. The MLG sheets react with the Ar plasma species to form a defect (i.e., a vacancy or nano-scale hole); these defects result in a change in the electrical resistance of the MLG.

The defect nature of the MLG devices was characterized using Raman spectroscopy. Fig.4.2 shows the first-order and second-order Raman spectra of pristine-MLG and p-MLG device. The Raman spectrum of the pristine-MLG exhibited graphitic (G and 2D) peaks, and a disorder D peak was not observed, which indicates the crystalline nature of MLG. In contrast, the p-MLG exhibited graphitic peaks as well as defect-associated (D, D′ and D+G) peaks. Here, the Raman-inactive D peak, which was attributed to the A1g symmetry of phonons near the K-zone, became active due to the presence of structural disorder.[3] The defect-related D peak appeared at 1364 cm,$^{-1}$ and another disorder-related (D′) peak appeared at 1628 cm,$^{-1}$which was attributed to intravalley phonons. An additional peak appeared at 2958 cm,$^{-1}$ which was attributed to D+G overtones. The existence of these defect-related peaks, and the increase in the full-width at half-maximum (FWHM) of the G and 2D peaks suggests the formation of structural disorder in the p-MLG. The concentration of the defects is given by the ratio of $I_{(D)}$ /$I_{(G)}$, and the defect type is given by the $I_{(D)}/I_{(D')}$ ratio. In our case, the defect concentration is 0.431 and the, $I_{(D)}$ /$I_{(D')}$ value is 3.26. These values suggest that the defects were due to vacancies, voids, and nano-scale holes. The density and nature of these defects strongly depend on the production and processing techniques, and we may expect some sample-to-sample variation in the graphene specimens.

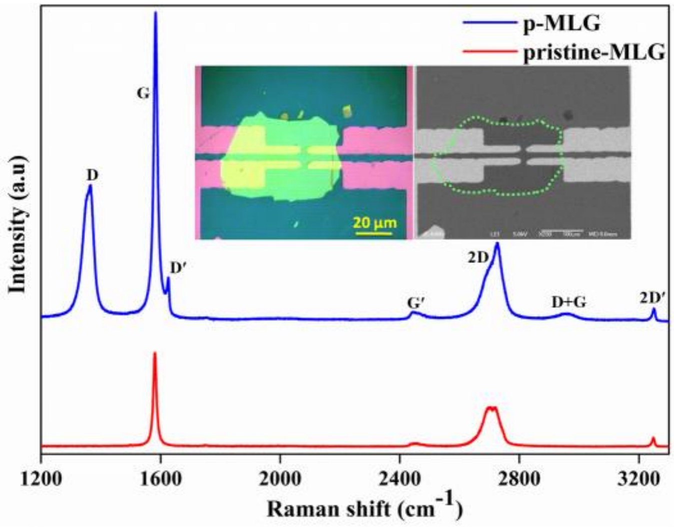

Fig.4.2. Micro-Raman spectrum (λ = 532 nm) of the pristine and plasma-irradiated devices. The inset at the top-left shows an optical microscopy image, and the inset at the top-right shows a FESEM image of a typical device.

The obtain Raman spectrum (Fig.4.2) confirms that the generated defects are holes, here we used FESEM analysis to envisage the defect. Fig.4.3a–d shows FESEM images of the p-MLG in different magnification on a silicon wafer following Ar plasma treatment. Nanoholes and vacancies are clearly visible; the size of the nanoholes varied in the range 100–500 nm. The FESEM images could not resolve the point-like defects, which were present all over the surface. In contrast, the pristine-MLG exhibited a smooth surface (see Fig.4.3e and f). Defects in p-MLG lead to an increase in the surface area, and the disorder at the surface results in localized regions of amorphous carbon atoms.[4]

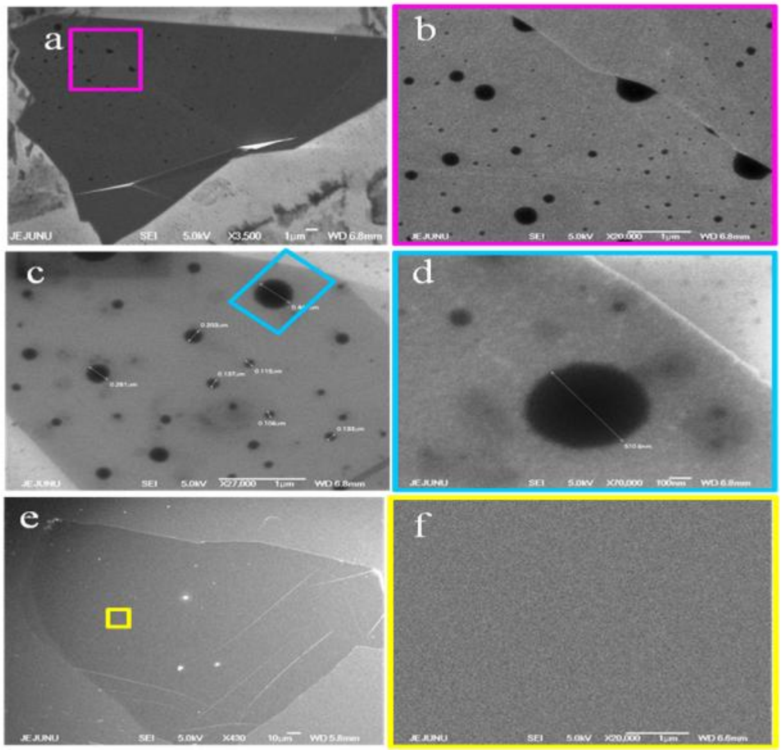

Fig.4.3. The FESEM image of p-MLG: (a) surface with different stack heights, (b) an enlarged view of the stack, (c) nanoholes of various sizes, and (d) a magnified image of a single nanohole. The FESEM image of pristine-MLG (e) Surface of the pristine-MLG (f) Magnified image of the marked (yellow color) area of the pristine-MLG (e) shows the smooth surface.

Further corroborate the Raman, FESEM results and to measure the depth of the defect, we employed 3D nano profile analysis. Fig.4.4a and b show images of the p-MLG, and the corresponding line profiles are shown in Fig.4.4c and d. The 3D view shown in Fig.4. 4b reveals that the entire surface of the MLG was affected by plasma irradiation. The roughness of the surface significantly increased following the plasma treatment, and served as clear evidence of the presence of defects. The plasma-induced nanoholes had various depths (see Fig.4. 4c and d); this variation may be promoted by the presence of ultra-small defects, such as STW defects or corrugated surfaces,[5]and then the synergistic effect of plasma carries the process further.[6] A high-magnification, 3D view of a single nanohole is shown in Fig.4. 4e; the width was ~ 4 nm and the depth was ~ 8.2 nm. The data shown in Fig.4. 4e were processed using image-processing software (SPIP 6.2.5), and the resulting image is shown in Fig.4. 4f. Here, the different colors indicate that the width and the depth of the nanoholes depended on the thickness of the MLG. These surface defects and nanoholes are the conductivity causing factors of the p-MLG.

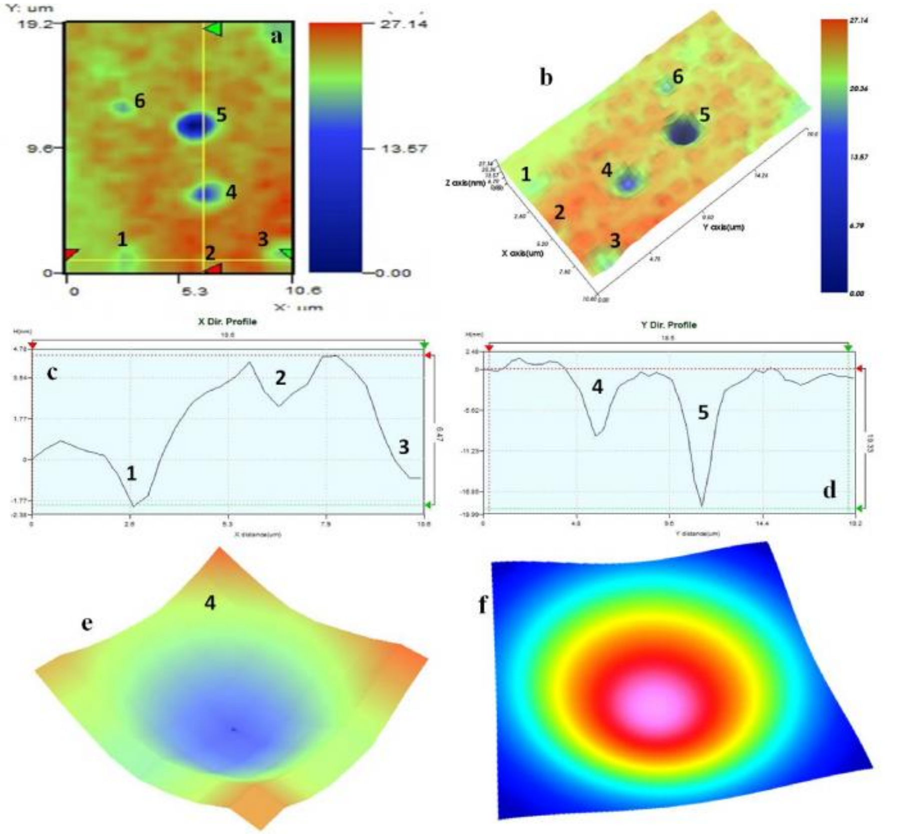

Fig.4.4. Surface profile analysis. (a) Two-dimensional image of p-MLG; here, the numbers 1 to 6 indicate the plasma-generated nanoholes. (b) 3D image of the data shown in (a). Line profiles of (c) the *x*- and (d) the *y*-axis of the data shown in (a). (e) High-magnification image of a single nanohole (numbered 4 in (a) and (b)). (f) Processed 3D image of the data shown in (e).

The plasma induced defect alters the electrical transport properties of the device. To investigate that we measured the current–voltage (*I*–*V*) characteristics of the MLG sample at room temperature (Fig.4.5a). The linear *I–V* response of pristine-MLG indicates the formation of Ohmic contacts between the Au electrodes and the MLG channel. The large current at an applied bias of 5 V shows that the resistance of the pristine-MLG was small. When the MLG was irradiated with Ar plasma for 10 min, the synergistic effect of the plasma species, including ions, electrons, photons, and metastable neutral atoms[6] struck the graphene lattice, which broke the π–π bonds, allowing some carbon atoms to detach, producing the nanoscale holes. The resulting p-MLG exhibited nonlinear *I–V* curves, as shown in Fig.4. 5a, with a drop in the current value of three orders of magnitude.

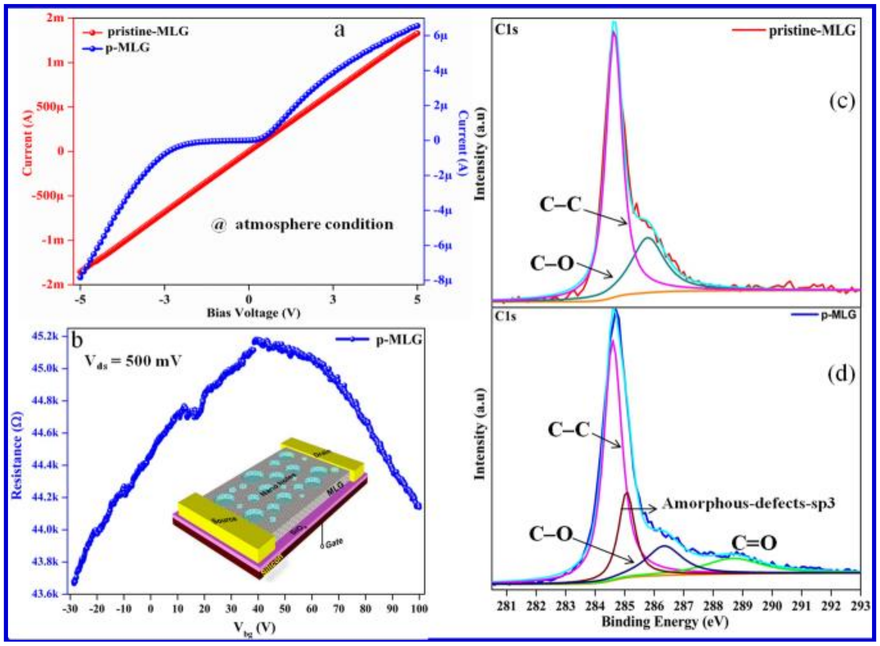

Fig.4.5. (a) Voltage-biased I–V curves of the pristine-MLG and p-MLG at room temperature, (b) Transfer characteristics of the p-MLG Field effect transistor device at the drain source voltage of 500 mV, Inset is the schematic of the p-MLG FET device. (c) and (d) C1s high-resolution XPS spectra of the pristine and p-MLG respectively. (Note that the spectra were deconvoluted using the Shirley method of background removal).

To elucidate the electrical properties of this p-MLG, we fabricate field-effect transistor (FET) with back-gate configuration (see the inset of Fig.4. 5b) and measured the transfer characteristics at room temperature. Fig.4.5b shows the resistance (R) as a function of back-gate voltage (V_{bg}), where the p-MLG device exhibits asymmetric ambipolar behavior and the Dirac point (maximum resistance, V_{DP}) is located around 39 V, whereas the ambipolar characteristic is absence in pristine-MLG device (data not shown). This p-type behavior of the p-MLG device clearly suggesting that the plasma irradiation leads to increase p-doping effect which deteriorates the electron conductivity (adsorbance of water and oxygen molecules)[7] and introduce an asymmetry between electron and hole transport [8] (semiconducting behavior), which leads to increase the device resistance.

Now it's necessary to identify the functional group involved in the p-doping effect of p-MLG for that we performed an XPS analysis to investigate the p-doping effect, Fig.4.5c and d, shows the C1s core level spectra corresponds to pristine and p-MLG devices, where the pristine-MLG exhibit two components, the peak at 284.6 eV is belong to sp^2 carbon (C=C/C–C) bonds and the other peak at 285.8 eV was assigned to C–O (non-covalent) bond this may arise during device fabrication.[2] The C1s spectra of p-MLG (Fig.4.5d) also shows a sp^2 carbon (C=C/C–C) peak at 284.6 eV, which significantly differs from pristine-MLG when the peak emerges at 285.0 eV which is attributed to the sp^3carbon due to the removal of carbon atoms (amorphous defect generation),[9,10] leads to deteriorating the electrical conductivity. The peak corresponds to C–O (286.3 eV) which has the possibility of forming epoxy and a hydroxyl group. For epoxy formation, one O atom bridging over two neighboring carbon atoms, because of the O2p orbital strongly hybridizes with extended π π* bands in graphene it changes the carbon planer (sp^2) hybridization to distorted sp^3 hybridization.[11] In case of hydroxyl formation the O atom is on top of a carbon with C–O bond nearly perpendicular to the graphene plane, which causes the change in carbon hybridization from sp^2 to sp^3 by forming a strong covalent bond between C and O. The peak at 288.5 eV ascribed to the formation of carbonyl bonds (C=O),[2,12] this may be a ketone. Soon or after defect generation, oxygen molecules from the atmosphere reacts with defected p-MLG surface and forms hydroxyl, epoxy and carbonyl functional groups which up-shifts the V_{DP} from 8 to 39 V in FET and also increases the device resistance considerably.

To further evaluate this resistance changing behavior of p-MLG, we opted temperature dependence of the resistance (R (T)) measurement (four probe). Fig.4.6a and b shows the R (T) behavior of the pristine and p-MLG device, with the sample thickness of ~21 and ~35 nm device respectively, where the resistance of the pristine-MLG decreases, when the temperature decreases (metallic nature), which was attributed to the overlapping bands, different stacking sequences, splitting of the π-band, and interlayer hopping of the charge carriers.[13, 14,15] In contrast, the temperature dependence of p-MLG was similar to that of a semiconductor, where the resistance decreased with increasing temperature. This semiconducting behavior overwhelm owing to the formation of various types of defect, such as point defects, vacancies, and nanoholes.[16] The sharp D-peak intensity, splitting of the G-peak, increment in the G-peak intensity (Raman spectra, Fig.4.2), visualization of the defects, nanoholes in the 3D nanoprofiler analysis (Fig.4.4b) indicates the formation of a large defect density and a drop in crystallinity (increment in the sp^2/sp^3 ratio), which significantly increases the resistance of the p-MLG.[16, 17]

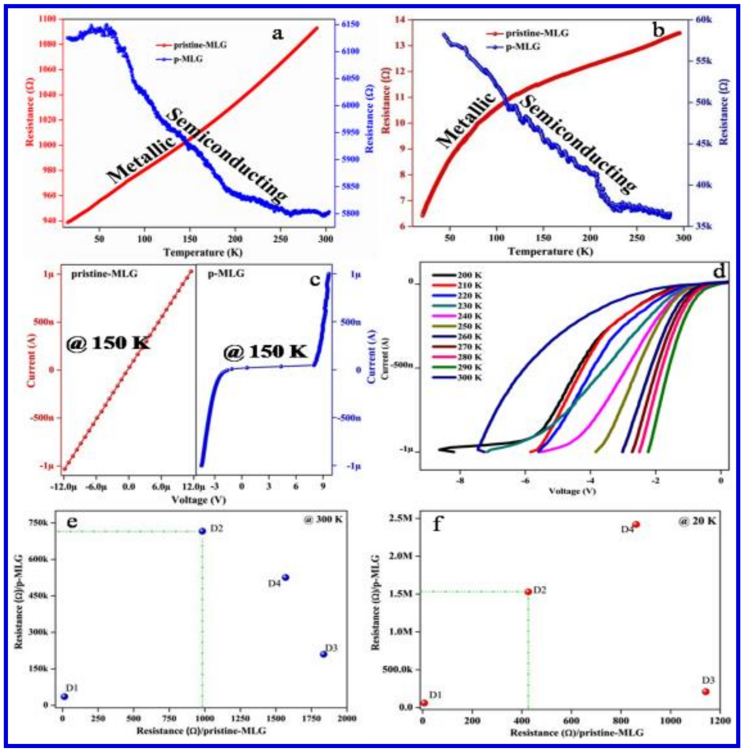

Fig.4.6. (a) and (b) Temperature dependence of the resistance R (T) of pristine and p-MLG device with the sample thickness of ~21 and 35 nm device respectively.(c) Current-biased, *I–V* curves of the pristine and p-MLG device at 150 K. (d) Current biased temperature dependent *I-V* characteristic of p-MLG at various temperature. (e) and (f) Temperature dependent resistance change of four different devices at room temperature (300 K) and low temperature (20 K) respectively (green color (dash dot dot) line is the guideline to the eye).

Fig.4.6b shows the current-biased, *I–V* characteristic of the pristine and p-MLG device at 150 K. We can clearly see a linear to non-linear transition in the *I–V* curves after the pristine- MLG was exposed to the Ar plasma. Similar behavior was observed at all temperatures (see Fig.4.6d). The temperature dependence of the resistance of the pristine and p-MLG of four different samples are shown in Fig.4.6e and f. The resistance of the p-MLG increased with decreasing temperature from 300 K down to 20 K, is mainly due to the deficiency of thermal excitation and hopping of charge carriers.

Charge transport in p-MLG can be described by a combination of (i) tunneling, (ii)hopping, (iii) *c*-axis conduction across nanoholes, and (iv) percolative conduction pathways. The plasma induces stacking faults, charge transport across these stacking faults is by tunneling.[18] A reduction in the hopping current across the holes with decreasing temperature due to the reduction in thermal excitation leads to an increase in the resistance of the p-MLG. In defect-free graphene, current flows across the graphene channel in the *ab*-plane, and *c*-axis charge transport is not significant; however, *c*-axis conduction becomes more significant here due to the presence of the nanoholes in the p-MLG. The charges flow in the *ab*-plane,[15] but diverge at the walls of the nanoholes.[2] With a sufficiently large defect density, charge transport in p-MLG follows percolative conduction pathways.[2, 16] This defect induced M-SC transition in MLG will be useful in nonlinear device applications.

4.5 Conclusions

In this chapter we have investigated the change in the electrical properties of MLG following exposure to an Ar plasma. The plasma induces vacancies, voids, and nanoholes on MLG, which resulted in semiconductor-like temperature dependence of the resistance. Where the electrical conduction is the combination of tunneling, hopping, and *c*-axis conduction between graphene sheets at nanoholes and, in regions of large defect densities, charge transport was via percolation.

References

[1] Terrones H, Lv R, Terrones M, Dresselhaus MS. The role of defects and doping in 2D graphene sheets and 1D nanoribbons Rep. Prog. Phys. 75, (2012), 062501.

[2] Thiyagarajan K, Ananth A, Saravanakumar B, Mok YS, Kim SJ. Plasma-induced photoresponse in few-layer graphene Carbon 73, (2014), 25-33.

[3] Thomsen C, Reich S. Double resonant Raman scattering in graphite Phys. Rev. Lett. 85, (2000), 5214-5217.

[4] Me´linon P, Hannour A, Bardotti L, Pre´vel B, Gierak J, Bourhis E, Faini G, Canut B. Ion beam nanopatterning in graphite: characterization of single extended defects Nanotechnology 19, (2008), 235305.

[5] Prével B, Benoit J-M, Bardotti L, Mélinon P, Ouerghi A, Lucot D, Bourhis E, Gierak J. Nanostructuring graphene on SiC by focused ion beam: Effect of the ion fluence Appl Phys Lett. 99, (2011), 083116.

[6] Rousseau B, Szwarckopf HE, Thomann A-L, BraultStable P. C-atom displacements on HOPG surface under plasma low-energy argon-ion bombardment Appl. Phys. A 77, (2003), 591-597.

[7] Feng T, Xie D, Zhao H, Li G, Xu J, Ren T, Zhu H. Ambipolar/unipolar conversion in graphene transistors by surface doping Appl. Phys. Lett. 103, (2013), 193502.

[8] Jacobsen A, Koehler FM, Stark WJ, Ensslin K. Towards electron transport measurements in chemically modified graphene effect of a solvent. New Journal of Physics 12, (2010), 125007.

[9] Yeo S, Choi C, Jang CW, Lee S, Jhon YM. Sensitivity enhancement of carbon nanotube based ammonium ion sensors through surface modification by using oxygen plasma treatment. Appl Phys Lett 102, (2013), 073108.

[10] Su Y, Pei S, Du J, Liu WB, Liu C, Cheng HM. Patterning flexible single-walled carbon nanotube thin films by an ozone gas exposure method. Carbon 53, (2013), 4-10.

[11] Yan J-An, Chou M. Y. Oxidation functional groups on graphene: Structural and electronic properties, Phy. Rev.B 82, (2010), 125403.

[12] Nourbakhsh A, Cantoro M, Klekachev AV, Pourtois G, Vosch T, Hofkens J, van der Veen M H, Heyns MM, De Gendt S, Sels BF. Single layer vs bilayer graphene: A comparative study of the effects of oxygen plasma treatment on their electronic and optical properties. J Phys Chem C 115, (2011), 16619-16624.

[13] Thiyagarajan K, Saravanakumar B, Mohan R, Kim SJ. Thickness dependent electrical transport properties of graphene. Sci Adv Mater 5, (2013), 542-548.

[14] Ohta T, Bostwick A, McChesney JL, Seyller T, Horn K, Rotenberg E. Interlayer interaction and electronic screening in multilayer graphene Investigated with angle-resolved photoemission spectroscopy. PRL 98, (2007), 206802.

[15] Venugopal G, Jung MH, Suemitsu M, Kim SJ. Fabrication of nanoscale three-dimensional graphite stacked junctions by focused-ion-beam and observation of anomalous transport characteristics. Carbon 49, (2011), 2766-2772.

[16] Zhang EX, Newaz AKM, Wang B, Zhang CX, Fleetwood DM, Bolotin KI, Schrimpf RD, Pantelides ST, Alles ML. Ozone-exposure and annealing effects on graphene-SiO_2 transistors. Appl Phys Lett. 101, (2012), 121601.

[17] Leconte N, Moser J, Ordejon P, Tao H, Lherbier A, Bachtold A, Alsina F, Sotomayor-Torres CM, Charlier JC, Roche S. Damaging graphene with ozone treatment: A chemically tunable metal–insulator transition. ACS Nano. 4, (2010), 4033-4038.

[18] Ono S. C-axis resistivity of graphite in connection with stacking faults. J Phys Soc Jpn 40, (1976), 498-504.

CHAPTER V

Plasma-induced Photoresponse in Few-Layer Graphene

5.1 Introduction

A photodetector is a device that produces an output signal depending on the light intensity illuminated in its active region. Graphene is the extraordinary material with controlled electronic properties, but it weakly absorbs light (only 2.3% of incident light), which is a major drawback for the development of graphene-based photodetectors.[1]A number of experimental methods have been proposed to enhance the photoresponsivity of monolayer graphene, by increasing the absorption efficiency and lifetime (few picoseconds) of photo-generated carriers.

In this chapter, we introduce a novel method to induce photoresponse from few layers of graphene (FLG) system through artificial defect generation resulting from atmospheric plasma irradiation. The first part of the chapter describes about the defect generation and structural changes, whereas the second part of the chapter explains the defect-induced electrical changes and photoconducting properties of pristine-FLG and plasma-irradiated FLG (p-FLG) were studied under both visible (535 and 405 nm) UV (365 nm) light illumination by introducing a defect midgap states band (MGB).

5.2. Experimental Section

FLG sheet was peeled from HOPG based on the technique described in section 2.1, were thickness approximation and electrode fabrication was done based on the condition described in section 2.2 and 2.3 respectively. The fabricated FLG device electrodes were covered with epoxy resin and dried at 150°C for 30 min in air to prevent electrode oxidization and damage. After that the FLG device was exposed to a homemade atmospheric plasma reactor shown in Fig.5.1a for 5 min in an Ar atmosphere (flow rate of 60 sccm) at a pressure of ~1 Torr. Fig.5.1b shows a digital photograph of the Ar plasma generated based on the above condition. The effect of plasma irradiation on the FLG surface was clearly observed in the optical microscope images shown in Fig.5.1c and d (before and after plasma irradiation, respectively).

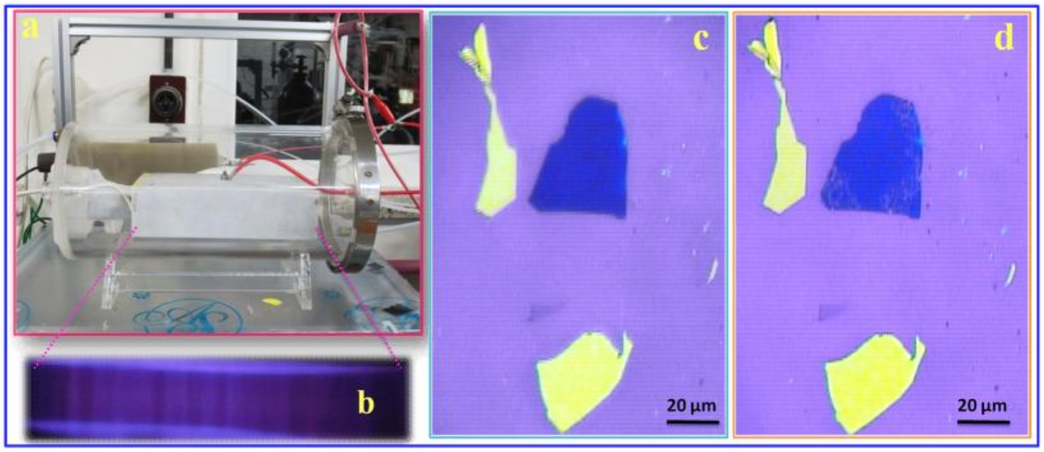

Fig.5.1. (a) Digital photograph of a homemade atmospheric plasma reactor. (b) The live photographic image of generated Ar plasma. Optical microscopic images in (c) and (d) correspond to before and after plasma irradiation.

5.3 Results and Discussion

Tailoring the property of solid materials with ion irradiation and collision cascades is a method that has been used for several decades.[2] Defect engineering is one way to create a bandgap in graphene to manipulate its electrical, chemical, and magnetic properties. To engineer the electronic properties of graphene, researchers introduced artificial defects to the graphene surface by ion-beam irradiation (Ga^+ and Ar^+).[3,4] Another approach is plasma irradiation, a novel method used to introduce defects and to dope the hydrophobic (chemically inert) graphene surface.[5,6]

Defects are good when they enhance the material's properties in useful ways. Plasma and ion irradiation on the hydrophobic graphene (solid material) can induce different types of surface defects (e.g., vacancies, graphene islands, doping and impurity).[7,8] Plasma irradiation disrupts honeycombed lattice to form vacancies,[9] resulting in a highly disordered morphology (see Fig.5.1d); the degree of disorder appears to be dependent on the thickness of the graphene flake.[10] The defect generation deteriorates the electrical conductivity of the graphene layers, even though it opens up several exciting applications in two-dimensional nanoelectronics.

5.3 .1 Defect generation and structural characterization

To evaluate the tantalizing defect behavior of the p-FLG device, we studied its Raman spectrum using a 514 nm Ar^+ ion laser as an excitation light source (Horiba Jobin Yvon LabRAM HR800 system). Fig.5. 2b shows the normalized Raman spectrum of a p-FLG device, along with a pristine FLG device. An optical microscopy image of a typical device is shown in the inset of Fig.5.2b (circles indicate the measurement sites). The defect peaks (D, D′) associated with the disorder were hardly noticeable in pristine FLG, however, strong peaks were observed at ~1364 cm^{-1} (D peak) and 1624 cm^{-1} (D′

peak) after plasma exposure. The existence of intervalley (D) and intravalley (D′) phonons strongly indicates defect formation on the graphene surface. Similar results were observed previously for ozone exposure,[1] oxygen plasma exposure,[11] Ga^+ ion irradiation[5] and electron-beam irradiation[12] on single-layer graphene.

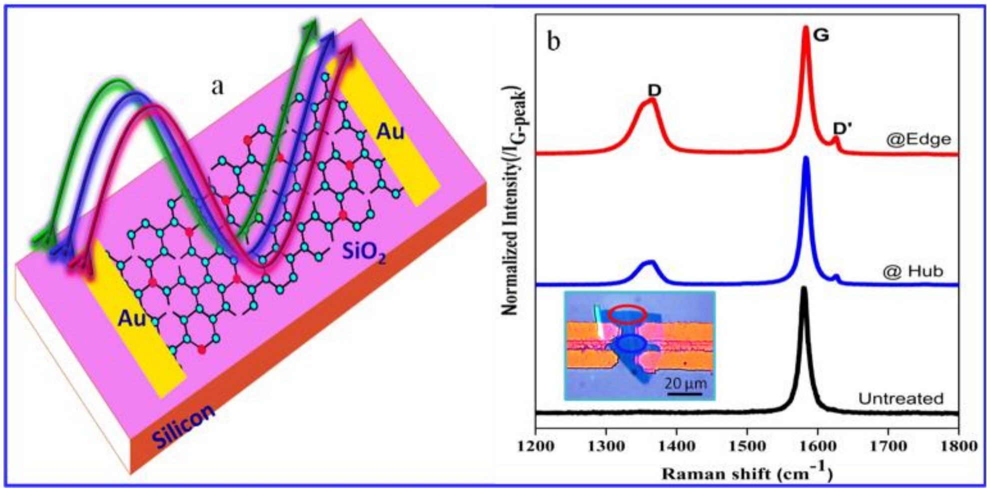

Fig.5.2. (a) Schematic representation of the plasma-irradiated graphene device. (b) The normalized micro Raman spectrum (λ = 532 nm) of the pristine few-layer graphene (FLG) sheets and plasma-irradiated (p-FLG) devices. The inset is an optical microscopy image of a typical device, where the circles indicate the measurement sites: hub (blue circle) and the edge (red circle).

To study the detailed defect generation at the graphene surface, we measured the Raman spectrum at different places on the graphene surface (e.g., the hub and the edge). The Raman spectrum of these distinct sites showed similar behavior, although with different intensities. The results clearly indicated that the defect levels were present more at the edges than the hub, which was in good agreement with the I_D/I_G ratios given in Table 5.1. This may be attributed to fewer graphene layers and different morphologies at the edges. The wavy degradation nature of graphene opens up novel applications in graphene research. These defects may act as light-absorbing site for optoelectronic applications.

Table 5.1. The intensity ratio’s of the Raman spectrum.

Sample FLG	Normalized G-peak Intensity (I_G)	D-peak Intensity (I_D)	D’-peak Intensity ($I_{D'}$)	Ratio of I_D/I_G	Ratio of $I_{D'}/I_G$	Ratio of $I_D/I_{D'}$
Pristine	1.00	-	-	-	-	-
Hub	1.00	0.204	0.166	0.204	0.166	1.228
Edge	1.00	0.455	0.106	0.455	0.106	4.292

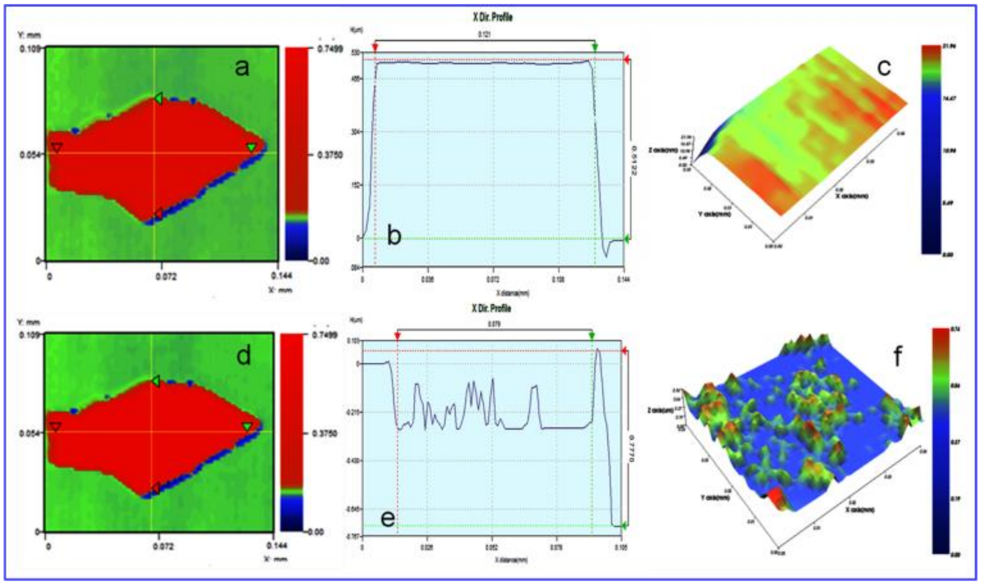

Fig.5.3. Surface profile analysis: (a) two-dimensional (2-D) image of FLG before plasma irradiation. (b) Line profile image corresponding to the *x*-axis of (a). (c) Three-dimensional (3-D) image showing the defect-free (uniform) surface. (d) 2-D image of plasma-irradiated FLG (i.e., the formation of p-FLG). (e) Line profile image corresponding to the *x*-axis of (d). (f) 3-D image showing defect formation on p-FLG.

To visualize the pristine FLG surface and the wavy degradation nature of p-FLG, we used a non-destructive, non-contact, three-dimensional (3-D) nanoprofile analysis (Nano System Co., Ltd) and showed in Fig.5., where the pristine FLG showed a smooth, defect-free surface with a roughness of 0.46 nm (Fig.5.3a–c). These measurements were in good agreement with Raman spectroscopy. Apparently, plasma irradiation induced defects on the FLG surface, e.g., graphene islands and graphene dots, which increased the surface roughness value to 78 nm (Fig.5.3d–f); the line profile in Fig.5.3e, shows defect formation clearly. The results shown in Fig.5.3f indicates that the graphene layers are not removed completely, due to plasma irradiation, which only induces defects on the surface of p-FLG.

The morphology of the p-FLG was characterized using AFM (XE-100, park system) and the result is presented in Fig.5.4. The morphology of the p-FLG is distinct from the pristine-FLG (see section 3.3) which exhibits a relatively flat surface, when compare to the p-FLG. Graphene exposed to plasma generally causing two important differences in surface (i) generating surface roughness, and (ii) blister formation (only for the prolonged plasma irradiation).[13] Fig.5.4c is the 2D image of the p-FLG and the corresponding line profile image is given in Fig.5.4e, in which the height variation clearly indicates that the plasma irradiation induces defect on the graphene surface. The 3D image of p-FLG (Fig.5.4d) is processed using image processing software (SPIP 6.2.5) and shown in Fig.5.4f, which certainly serves as a evident for the formation of nano size defect hole (nano hole) on p-FLG surface and the depth of these defect holes is around 0.1-0.5 nm. These defects were contributing to the defect related D and D' peaks of the Raman spectrum. Optical microscopy images, surface profile analysis, AFM analysis, and Raman spectroscopy confirm that the plasma irradiation induces defect on graphene surface.

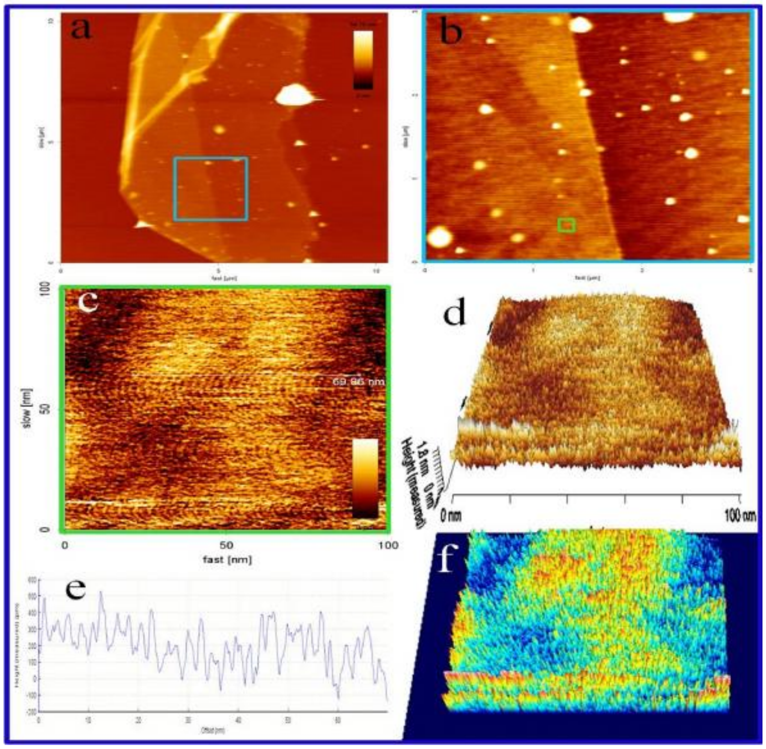

Fig.5.4. AFM analysis: (a, b) two-dimensional (2-D) image of p-FLG with different magnification. (c) 2-D image of the p-FLG at a small scan area of (100 nm) and the corresponding three-dimensional (3-D) image shown in (d). (e) Line profile image corresponding to the *x*-axis of (c). (f) Processed 3-D image of (d) showing the nano hole defect formation on p-FLG.

To confirm the attachment of a foreign body (oxygen bonding) on p-FLG was confirmed by X-ray photoelectron spectroscopy (XPS) using an ESCA-2000, VG Microtech Ltd. spectrometer (Al Kα). Different components of the XPS spectrum were deconvoluted using the Shirley method of background removal in conjunction with a least squares fitting algorithm using full Voigt functions. Fig.5.5a and b correspond to the C 1s core level of the XPS spectra of FLG before and after plasma irradiation, respectively. The XPS results for pristine FLG revealed two different carbon bonds, as indicated by the peaks in Fig.5.5a. The peak at 284.6 eV was attributed to sp^2 carbon

(C=C/C–C) bonds,[13-15] and the other peak at 285.8 eV was assigned to C–O bond that may arise during device fabrication.[16] Fig.5.5b is the XPS spectra of p-FLG. The peak at 284.6 eV corresponds to the sp^2 carbon (C=C/C–C) bonds,[13,14] and the peak at 285.0 eV is ascribed to the sp^3 carbon due to amorphous defect generation (removal of carbon atoms from the honeycombed lattice)[4,17,18] an increment in the peak intensity suggested that the surface was affected by plasma irradiation. The additional two peaks at 286.3 and 288.5 eV were attributed to C–O (epoxy/hydroxyl bonds)[13,19] and C=O (carbonyl bonds),[7,16,20] soon after defect generation, oxygen molecules from the atmosphere reacts with defected graphene surface to produce O–containing groups.[6] These results imply that chemical bonds have been formed between carbon and oxygen when FLG was exposed to atmospheric plasma.

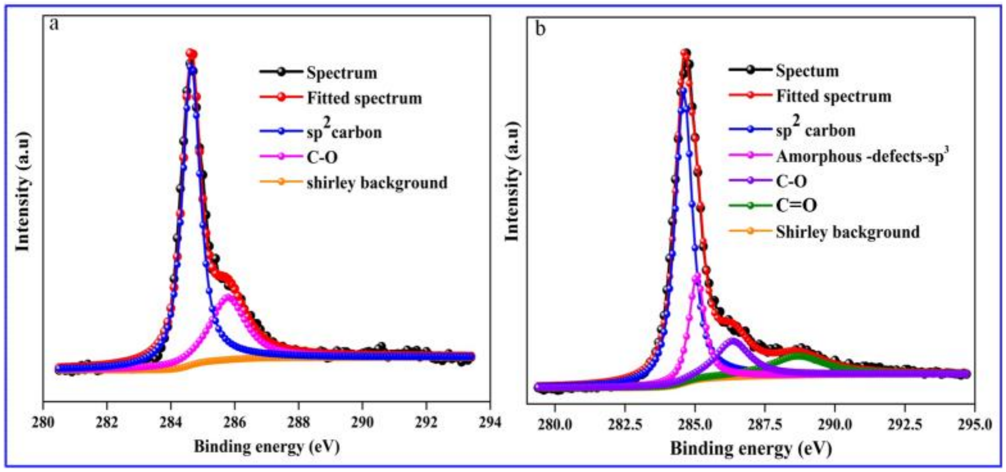

Fig.5.5. C1s high-resolution XPS spectra of the FLG device (a) before and (b) after plasma irradiation. Components related to various chemical shifts of the carbon bonds are indicated. (Note that the spectra were deconvoluted using the Shirley method of background removal).

5.3.2 Defect-induced electrical changes and photoconducting properties

The photoresponsivity of the pure graphene photodetector was low; we attributed this result to the poor absorption efficiency and short recombination lifetimes (few picoseconds) of the photo-generated carriers.[19] To date, few studies have investigated the photocurrent generation in graphene based on carrier multiexcitation generation (MEG) (i.e., multiple charge carriers generated from the absorption of a single photon by impact ionization), also known as inverse Auger recombination (AR).[21,20,22] Plasma irradiation of FLG tends to induce surface defect or vacancy formation, such as graphene quantum dots, graphene islands, and doping as well as deposit the impurities on hydrophobic lattice.[8] The underlying graphene layers serve as a transport layer, where the edges (having more defects) eventually follow percolative conduction path mechanism.[1] The defects, dopant (oxygen), and impurities are acting as light-absorbing centers, whereas graphene quantum dots or islands frame the MGB which behaves as an electron-trapping center, and a bandgap is created due to the quantum confinement.

Fig.5.6a shows the energy band diagram for photocurrent generation in p-FLG. The incident photons (IP) generates an electron–hole pair through photo-excitation (PE) after impact ionization (II) (red arrows). The photo-excited electron relaxes to a lower–energy state inside the conduction band via an intraband transition simultaneously; an interband transition occurs that stimulates excitation of a valence band electron to the conduction band. Concurrently, electrons in the conduction band are scattered to the valence band by transferring energy to another electron present in the conduction band, which is ultimately excited to a higher- energy level by the AR process (black arrows

Fig.5.6a). Thus, carrier multiplication was accomplished through impact ionization (II) and AR process,[23,24] which produces secondary electrons in the conduction band. Electron-phonon scattering decreases[25] between the conduction and valence bands soon after the band gap formation, which results in more photoexcited and secondary generated electrons trapping in the MGB. The photo-generated hole is recirculated through hopping within the lifetime, which results in a high photoconductive gain.

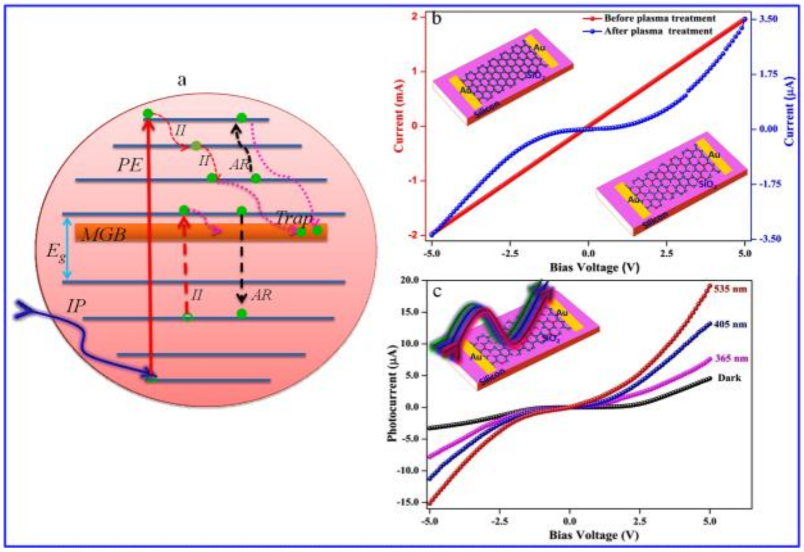

Fig.5.6. (a) Energy band diagram (including the defect midgap states band (MGB) and band gap energy (Eg)), including the concept for photocurrent generation for p-FLG. An incident photons (IP) interacts with the electron in the valence band and generates an electron–hole pair via photon excitation (PE), followed by the impact ionization (II) process. When the excited electron transfers to the lower energy level in the conduction band and transfers the energy to another electron, initiating the AR process. Each of the steps in this cascade increases the population of electron–hole pairs; the multiexcitation generation (MEG) effect exists, the possibility of more excited electrons being trapped by the MGB. (b) Current (*I*) versus voltage (*V*) curve for FLG, before (red) and after (blue) plasma irradiation; the insets are the corresponding device structures before (top-left) and after (lower-right) plasma irradiation. (c) The photoresponse *I*–*V* curve of the p-FLG device under dark conditions and also with various light sources. The inset shows a schematic diagram of the p-FLG device interacting with light source.

The electrical and photocurrent measurements were carried out using a semiconductor parameter analyzer (Agilent, B 1500A) combined with a Prizmatix multi-wavelength LED light source. Fig.5.6b shows the current–voltage (*I*–*V*) characteristics of FLG before (red) and after (blue) plasma irradiation; the insets are the corresponding device structures before (top-left) and after (lower right) plasma irradiation. The pristine FLG device exhibited linear (ohmic) *I*–*V* behavior with high electrical conductivity. After plasma irradiation (i.e., the formation of p-FLG), the device conductivity deteriorated considerably, exhibiting nonlinear behavior (Schottky). This behavior was attributed to the detachment of carbon atoms from the honeycomb lattice, the doping of oxygen, breaking of the π–π bond, and void formation, leading to the production of a vast number of graphene quantum dots, which absorb the incident light more efficiently than does pristine graphene. The layers with most defects ultimately results in a percolative conduction path for the applied bias voltage. To explore the plasma-induced photoresponse characteristics of the FLG device, we carried out photoelectric measurements under ambient conditions and an applied bias of 5 V for different illumination wavelengths (Fig.5.6c). As a reference, we also measured the pristine FLG device under the same conditions. No obvious response was observed, which was expected due to the higher transmittance of defect-free graphene; however, the p-FLG device showed a strong dependence on illumination wavelength (see Fig.5.6c). The maximum photocurrent was observed under 535 nm illumination; the photocurrent decreased with the illumination wavelength. The device illuminated with 365 nm photocurrent ($I_{light\text{-}365\ nm}$) exhibited a maximum photocurrent of 7.67 μA, and the photocurrent $I_{light\text{-}405\ nm}$ and $I_{light\text{-}535\ nm}$ improved to 13.31 and 19.16 μA for the 405 and 535 nm wavelengths, respectively, under an applied bias voltage of 5 V.

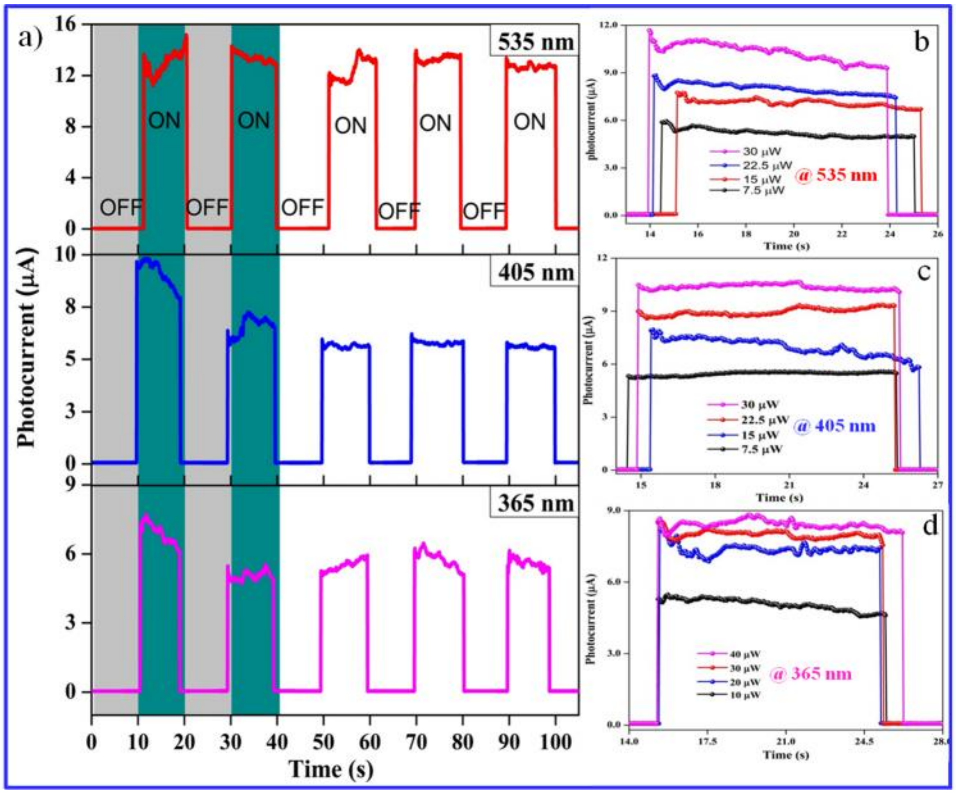

Fig.5.7. (a) Time-dependent photocurrent spectra of the p-FLG device under UV (365 nm) and visible (405 and 535 nm) light irradiation for a bias of 0 V, with multiple on/off cycles. The power dependence photocurrents for (b) 535, (c) 405, and (d) 365 nm at 0 V bias voltage.

The time-dependent photocurrent measurement of the p-FLG device under UV (365 nm) and visible (405 and 535 nm) light irradiation at 0 V bias, with multiple on/off cycles is presented in Fig.5.7a. The turn-on and turn-off time of the light source was 10 s. The device exhibited excellent stability and reproducibility over the UV and visible region. When the light source was turned on, the photocurrent reached its maximum within a millisecond (ms). The ratio I_{light} to I_{dark} increased as the illumination wavelength, increased, having values of 90, 100, and 227, for wavelengths 365, 405, and 535 nm respectively. The incident power dependence; and photocurrent for p-FLG are shown in Fig.5.7b–d at different wavelength illuminations. Linear behavior was observed for the visible and UV wavelengths, indicating the broader spectral response of graphene.

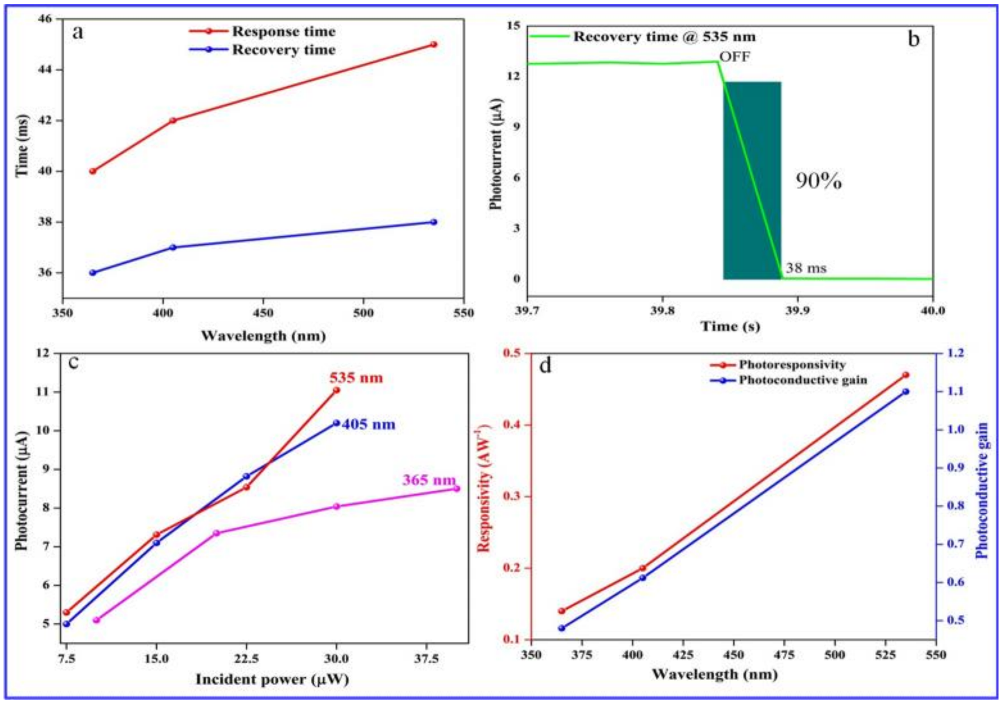

Fig.5.8. Summarized photoresponse result of the p-FLG device. (a) The response and recovery times of the device under UV and visible-light irradiation. (b) The magnification of a single on/off cycle for 535 nm. (c) The power-dependence photoresponse of the p-FLG device. (d) Responsivity and photoconductive gain of the p-FLG device as function of the incident light source.

The summarized photoresponse result of the p-FLG device is presented in Fig.5.8. The response and recovery time of the device with respect to illumination wavelength is shown in Fig.5.8a; the response and recovery time increased linearly with the illumination wavelength. The high-energy (365 nm) photons reduce the depletion barrier in a shorter time than did the low energy photons (405, and 535 nm light). Soon after the light was switched off, the recovery process was initiated, with the device reaching 10% of its maximum value within 38 ms, as shown in Fig.5.8b. The fast recovery observed for the high-energy photons was attributed to recombination through interband transitions. In contrast, the existence of a dominant intraband transition created an increment in the recovery time.[21] However, the response and recovery time of our device was comparable to that in previous reports[21,26] The photocurrent as a function of incident power with various illumination wavelengths is shown in Fig.5.8c. The photocurrent of the device increased linearly with the incident power for all illumination wavelengths.

The most significant parameters to determine the capability of a photodetector or photoconductor is responsivity (R), which depends on the electrical output to the optical input. R is defined as,

$$R\left(AW^{-1}\right) = \frac{\left(I_{light} - I_{dark}\right)}{P_{opt}} = \eta\left(\frac{q\lambda}{hc}\right)G \qquad (5.1)$$

Where, $I_{light,}$ I_{dark}, $P_{opt,}$ η, q, λ h, c and G are the current under illumination, current in dark, incident light power, quantum efficiency, electronic charge, light wavelength, Planck's constant, speed of light, and photoconductive gain, respectively. The responsivity of the p-FLG device is estimated using Eq. (1), assuming that η =1 at a bias voltage of 0 V for the three different wavelengths shown in Fig.5.8d. The high responsivity of 0.47, 0.20 and 0.14 AW^{-1} was obtained for 535, 405, and 365 nm wavelengths, respectively. This high photoresponsivity of p-FLG was achieved through electron-hole pair generation by direct PE and the impact ionization process. Meanwhile, the photoconductive gain for p-FLG also calculated and the values are 1.1, 0.61, and 0.48 corresponds to the 535, 405, and 365 nm illumination wavelength, respectively

(Fig.5.8d). The photoconductive gain increased with respect to the wavelength, which arose due to the increment in carrier MEG efficiency. When the photo-excited electron arrived to the higher– energy level in the conduction band, it began to scatter into the lower energy levels of the conduction band by impact ionization. This generated more excitons, which led to the capture of the electron in the MGB state, resulting in a higher photoconductive gain.[21] In case of high-energy (UV) photons the responsivity and the photoconductive gain values are small when compare to the lower-energy (visible light) photons, this due to photoinduced molecular desorption,[14] from defected graphene surface. The plasma-induced structural defects open up a new way to tailor graphene properties to specific optoelectronic applications.

5.4. Conclusions

We have demonstrated a simple, novel way to harvest the optoelectronic properties of graphene layers based on atmospheric plasma irradiation. Plasma-induced structural defects and electrical changes were systematically studied. The photoconducting ability of p-FLG was tested under both visible and ultraviolet light illumination. A maximum photoresponsivity of 0.47 AW^{-1} and photoconductive gain of 1.1 were achieved with 535 nm light illumination and a bias voltage of 0 V.

References

[1] Zhang EX, Newaz AKM, Wang B, Zhang CX, Fleetwood DM, Bolotin KI, Schrimpf RD, Pantelides ST, Alles ML. Ozone-exposure and annealing effects on graphene-SiO_2 transistors Appl Phys Lett. 101, (2012), 121601.

[2] Kitagawa K, Yamakawa K, Fukushima H, Yoshiie T, Hayashi Y, Yoshida H, Shimomura Y, Kiritani M. Ion-irradiation experiment for the fundamental studies of damage evolution of fusion materials J Nucl Mater 133–134, (1985), 395-399.

[3] Al-Harthi SH, Kara`a A, Hysen T, Elzain M, Al-Hinai A. T, Myint MTZ. Evolution of surface morphology and electronic structure of few layer graphene after low energy Ar^+ ion irradiation Appl Phys Lett 101, (2012), 213107.

[4] Zhou YB, Liao ZM, Wang YF, Duesberg GS, Xu J, Fu Q, Wu XS, Yu DP. Ion irradiation induced structural and electrical transition in graphene J Chem Phys 133, (2010), 2347031.

[5] Cheng YC, Kaloni TP, Zhu ZY, Schwingenschlögl U. Oxidation of graphene in ozone under ultraviolet light. Appl Phys Lett 101, (2012), 073110.

[6] Fang Z, Wang Y, Liu Z, Schlather A, Ajayan PM, Koppens FHL, Nordlander P, Halas NJ. Plasmon-induced doping of graphene ACS Nano 6, (2012), 10222-10228.

[7] Nourbakhsh A, Cantoro M, Klekachev AV, Pourtois G, Vosch T, Hofkens J, van der Veen M H, Heyns MM, De Gendt S, Sels BF. Single layer vs bilayer graphene: a comparative study of the effects of oxygen plasma treatment on their electronic and optical properties. J Phys Chem C 115, (2011), 16619-16624.

[8] Singh AK, Penev ES, Yakobson BI. Vacancy clusters in graphene as quantum dots. ACS Nano 4, (2010), 3510-3514.

[9] Woo SO, Teizer W. The effect of electron induced hydrogenation of graphene on its electrical transport properties Appl Phys Lett 103, (2013), 041603.

[10] Tao H, Moser J, Alzina F, Wang Q, Sotomayor-Torres CM. The morphology of graphene sheets treated in an ozone generator J Phys Chem C 115, (2011), 18257-18260.

[11] Childres I, Jauregui LA, Tian J, Chen YP. Effect of oxygen plasma etching on graphene studied using Raman spectroscopy and electronic transport measurements. New J Phys 13, (2011), 025008.

[12] Teweldebrhan D, Balandin AA. Modification of graphene properties due to electron-beam irradiation. Appl Phys Lett 94, (2009), 013101.

[13] Lee SW, Mattevi C, Chhowalla M, Mohan Sankaran R. Plasma-assisted reduction of graphene oxide at low temperature and atmospheric pressure for flexible conductor applications J Phys Chem Lett, 3, (2012) 772-777.

[14] Sun P, Zhu M, Wang K, Zhong M, Wei J, Wu D, Cheng Y, Zhu H. Photoinduced molecular desorption from graphene films Appl Phys Lett 101, (2012), 053107.

[15] Peltekis N, Kumar S, McEvoy N, Lee K, Weidlich A, Duesberg GS. The effect of downstream plasma treatments on graphene surfaces Carbon 50, (2012), 395-403.

[16] Choi K, Lim J, Rani JR, Yoon HS, Oh J, Hong T, Ha T, Park BC, Sim KI, Jun SC, Kim J H. Terahertz and optical study of monolayer graphene processed by plasma oxidation Appl Phys Lett 102, (2013), 131901.

[17] Yeo S, Choi C, Jang CW, Lee S, Jhon YM. Sensitivity enhancement of carbon nanotube based ammonium ion sensors through surface modification by using oxygen plasma treatment Appl Phys Lett 102, (2013), 073108.

[18] Su Y, Pei S, Du J, Liu WB, Liu C, Cheng HM. Patterning flexible single-walled carbon nanotube thin films by an ozone gas exposure method. Carbon 53, (2013), 4-10.

[19] Breusing M. Ropers C, Elsaesser T. Ultrafast carrier dynamics in graphite Phys Rev Lett 102, (2009), 086809.

[20] Tielrooij KJ, Song JCW, Jensen SA, Centeno A, Pesquera A, Elorza AZ, Bonn M, Levitov LS, Koppens FHL. Photoexcitation cascade and multiple hot-carrier generation in graphene Nat Phys 9, (2013), 248-252.

[21] Zhang Y, Liu T, Meng B, Li X, Liang G, Hu X, Wang QJ. Broadband high photoresponse from pure mono graphene photodetector Nat Commun 4, (2013), 1811.

[22] Winzer T, Knorr A, Malic E. Carrier multiplication in graphene. Nano Lett 10, (2010), 4839-4843.

[23] Sukhovatkin V, Hinds S, Brzozowski L, Sargent EH. Colloidal quantum-dot photodetectors exploiting multiexciton generation Science 324, (2009),1542-1544.

[24] Schaller RD, Klimov VI. High efficiency carrier multiplication in PbSe nanocrystals implications for solar energy conversion Phys Rev Lett 92, (2004), 186601.

[25] Ellingson RJ, Beard MC, Johnson JC, Yu P, Micic OI, Nozik AJ, Shabaev A, Efros AL. Highly efficient multiple exciton generation in colloidal PbSe and PbS quantum dots Nano Lett 5, (2005), 865.

[26] Sun Z, Liu Z, Li J, Tai G, Lau SP, Yan F. Infrared photodetectors based on CVD-grown graphene and PbS quantum dots with ultrahigh responsivity Adv Mater 24, (2012), 5878-5883.

CHAPTER VI

Gate-tunable Photoresponse of Defective Graphene: from Ultraviolet to Visible

6.1 Introduction

A photodetector is a device that produces an output signal depending on the light intensity illuminated in its active region. These days the photodetectors are made up of different photoactive semiconductors with appropriate bandgap,[1] to detect the wide spectral (ultraviolet to far-infrared) range, which is the central to the imaging, sensing, and spectroscopic applications.[2] In contrast, the tunable bandgap in the fascinating two-dimensional graphene promises the ultra-broadband photodetection[1,3,4] (ultraviolet to far-infrared) due to the electron hole pair generation upon a light irradiation over a broad spectrum.[1,5] Graphene field effect transistors (GFET) are recognized as a type of excellent transducers for photodetection thanks to the inherent amplification function of the transistors and the feasibility of miniaturization and the unique properties of graphene.

In this chapter, we demonstrate, the gate tunable photoresponse behavior of the defected graphene, over ultraviolet to the visible region, where the plasma irradiation induces the defects on surface graphene. Depend on the illumination wavelength the Dirac point of the device shifts either sides along with the change in the drain current, which engenders a novel way to tailor the photoresponse of the graphene.

6.2 Experimental section

The sample preparation, thickness approximation, and electrode fabrication are discussed in the section 2.1-2.3. Prior to plasma exposure, Raman spectrum (see Fig.6.1b (blue color)) and electrical measurements were carried out to ensure the properties of the pristine-GFET, and then the device was exposed to a custom-made atmospheric plasma reactor under Ar atmosphere with a flow rate of 60 sccm at a pressure of ~1 Torr for 1 min. After that the structural and electrical modification of the plasma treated GFET (defective-GFET) was systematically studied and presented in the next section of this chapter.

6.3 Results and discussion

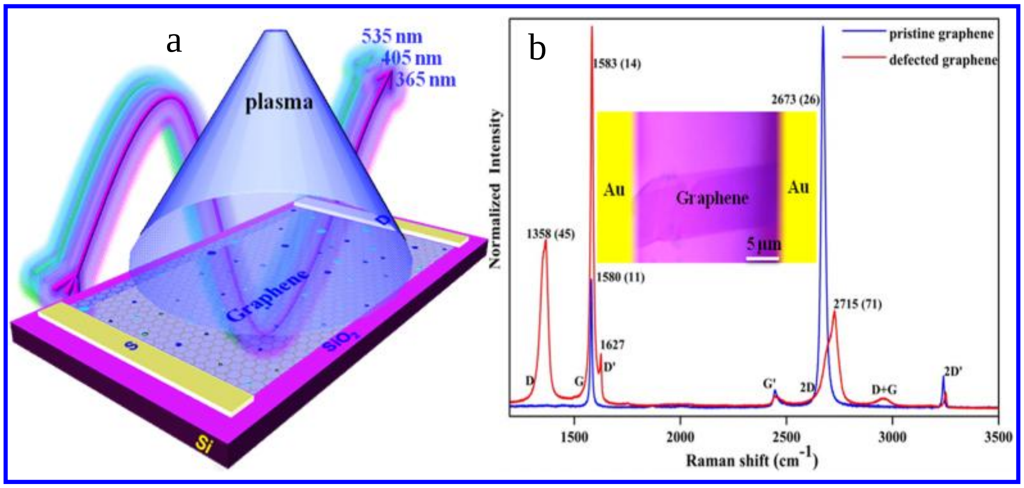

Fig.6.1. (a) Schematic representation of defect generation, and photoresponse of the fabricated graphene device (b) The normalized micro Raman spectrum of the pristine and the defective graphene device, where the numbers denote the peak positions and the numbers in the brackets are the full width half maximum of the corresponding peaks. The inset is an optical microscopy image of a typical device.

The schematic of the fabricated defective-GFET is shown in Fig.6.1a, where the point like structure in the graphene lattice represents the defects generated by plasma irradiation and the arrows represents the three different wavelengths used for the photocurrent measurement. The normalized Raman spectrum of the pristine (blue color) and defective (red color) GFET was shown in Fig.6.1b. Absence of defect related D peak and the appearance of G and 2D (graphitic) peaks, with the intensity ratio of 2.94 indicates that the device was successfully fabricated on a SiO_2/Si substrate without causing any material damage.[6] The inset in Fig.6.1b is the optical microscopy, image of the fabricated GFET device. The appearance of defect associated (D, D′ and D+G) peaks along with G and 2D peaks, in defected-GFET, suggest that the A1g symmetry phonons near the K-zone, became active[7] when the device exposed into plasma. The existence of these defects-related peaks, with increment in the full-width at half-maximum (FWHM - numbers in the brackets) of the G and 2D peaks along with the peak shift towards higher wave numbers confirm the formation of structural defects[7] which also suggested that the defects induces p-doping in graphene device.[8]

To examine the electrical transformation of the defected-GFET, we measured the transfer characteristics of the defected-GFET in room atmosphere and compared with pristine-GFET with respect to back-gate voltage (V_{bg}) at drain –source voltage (V_{ds}) of 10 mV and the result is depicted in Fig.6.2b. The pristine-GFET device (see the inset of for the schematics) shows an ambipolar behavior with the Dirac point (V_{Dirac} charge neutrality point) at 8 V in the back-gate, which implies the p-doping characteristics, due to the adsorbance of water and oxygen molecules on graphene surface.[6] Where as the Dirac point of the defected-GFET device is up-shifted to 39 V, which clearly suggest that the plasma treatment leads to increase the p-doping effect and introduce an asymmetry between electron and hole transport due to the accumulation holes in graphene surface.[9] The plasma treatment introduces nanoscale defects in graphene surface, where the honeycomb lattice was broken by the synergistic effect of the plasma species,[10] and the defect sites were reacting with the oxygen molecules (from atmosphere), making the device p-doped, which up-shifts the Dirac point to 39 V. The functional groups involved in the p-doping effect was obtained via X-ray photoelectron spectroscopy (XPS), Fig.6.2 a and c illustrates the C1s core level spectra of pristine and defected-GFET respectively.

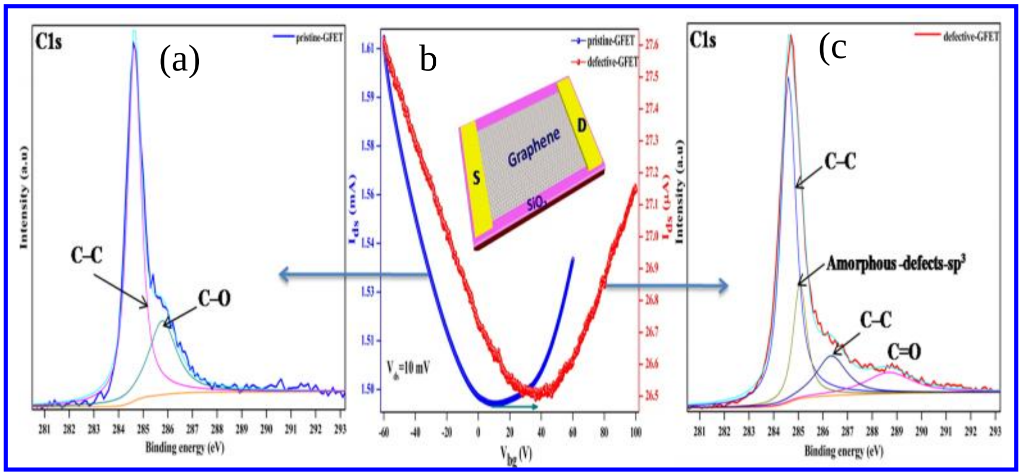

Fig.6.2. (a) C1s high-resolution XPS spectra of the pristine –GFET device. (b) Transfer characteristics of the pristine and defective-GFET device at the drain source voltage of 10 mV. (c) C1s high-resolution XPS spectra of the defective–GFET device, (Note that the spectra were deconvoluted using the Shirley method of background removal).

The spectra of pristine graphene fitted with two peaks, where the 284.6 eV peak, belong to sp^2 hybridized carbon atom (C–C bond) and the other peak at 285.8 eV was assigned to non-covalent C–O bond, this may arise during device fabrication.[7] In contrast the C1s spectrum of defective graphene is fitted with four major components, where the higher intensity peak at 284.6 eV, which is similar to that of pristine, spectrum differs when the peak emerges at 285.0 eV, which is attributed to the formation of sp^3 hybridized carbon atoms, due to the removal of carbon atoms from the honeycomb lattice (amorphous defect generation).[11] The peak corresponds to C–O (286.3 eV), which has the possibility of forming epoxy and a hydroxyl group. For epoxy formation, one O atom bridging over two neighboring carbon atoms, because of the O2p orbital strongly hybridizes with extended π π* bands in graphene it changes the carbon planer (sp^2) hybridization to distorted sp^3 hybridization.[12] In case of hydroxyl formation the O atom is on top of a carbon with C–O bond nearly perpendicular to the graphene plane which causes the change in carbon hybridization from sp^2 to sp^3 by forming a strong covalent bond between C and O.[12] The peak at 288.5 eV ascribed to the formation of carbonyl bonds (C=O),[7] this may be a ketone. From the XPS spectra it's clear that the p-doping behavior emerges in defective GFET, ascribed to the formation of hydroxyl, epoxy and carbonyl functional groups which up-shifted the V_{Dirac} from 8 to 39 V. The plasma induced defects and the functional groups are the light absorbing agents in the photocurrent measurement.

Fig.6.3b shows the effect of light illumination on defected-GFET with different wavelength, where the Dirac point of the transfer curve in the dark is around 39 V, indicating the heavy p-doped nature of the device. When the device illuminated by the visible light of 405 and 535 nm, the Dirac points shifted more towards the positive direction, along with the drain current increment (I_{ds}) in the p-channel indicates the further p-doping behavior.[8,9]Where as the Dirac point shifted towards the negative side and the I_{ds} in the p-channel decreases, when the device illuminated by UV light (365 nm), indicating the n-doping behavior, due to the photo-induced molecular desorption that decreases the hole density in the defective-graphene channel.[13,14] There is no shift in the Dirac point of the pristine-GFET, when illuminated with different wavelengths of light (see Fig.6.3a). The photocurrent dependence on gate voltage with respect to wavelength can be obtained by subtracting the dark current from the light current (I_{light} – I_{dark}) and the result is plotted in Fig.6.3c. It is clear that the gate-dependent photoresponse of the defective-GFET, can be tuned by illumination wavelength. The typical photoresponse of the defected-GFET device as a function of source – drain voltage (V_{ds}) under different illumination wavelengths (Fig.6.3d) with constant back gate voltage of 10 V, attributed to the effective separation of electron- hole pairs [1, 9] in the defected graphene. For reference, we also measured the pristine-GFET device under the same condition, no obvious response was observed, which was expected due to the poor absorbance and short recombination lifetime of the photo-generated carriers in defect-free graphene.[3,7,15]

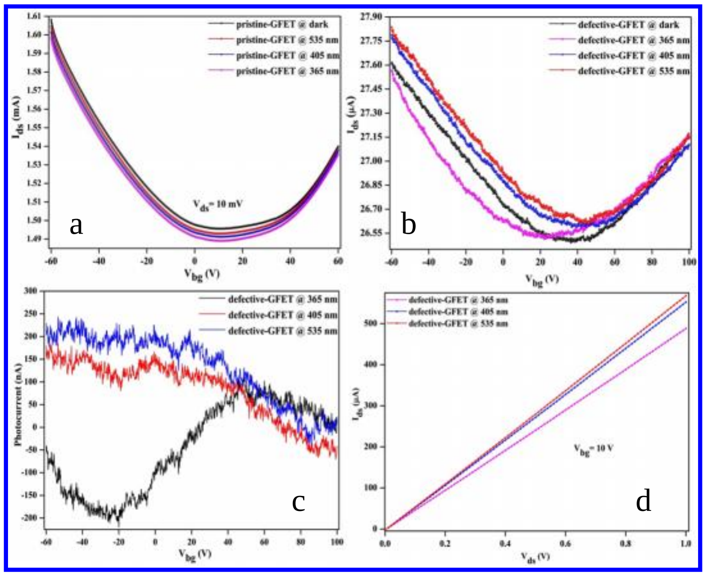

Fig.6.3. Transfer curves (a) pristine and (b) defective GFET device under different illumination wavelength. (c) Photocurrent as a function of back gate voltage based on the transfer curves obtained in (b). (d) Photocurrent of the defective-GFET device with respect to the source-drain voltage, under the different illumination wavelength at constant V_{bg} =10 V.

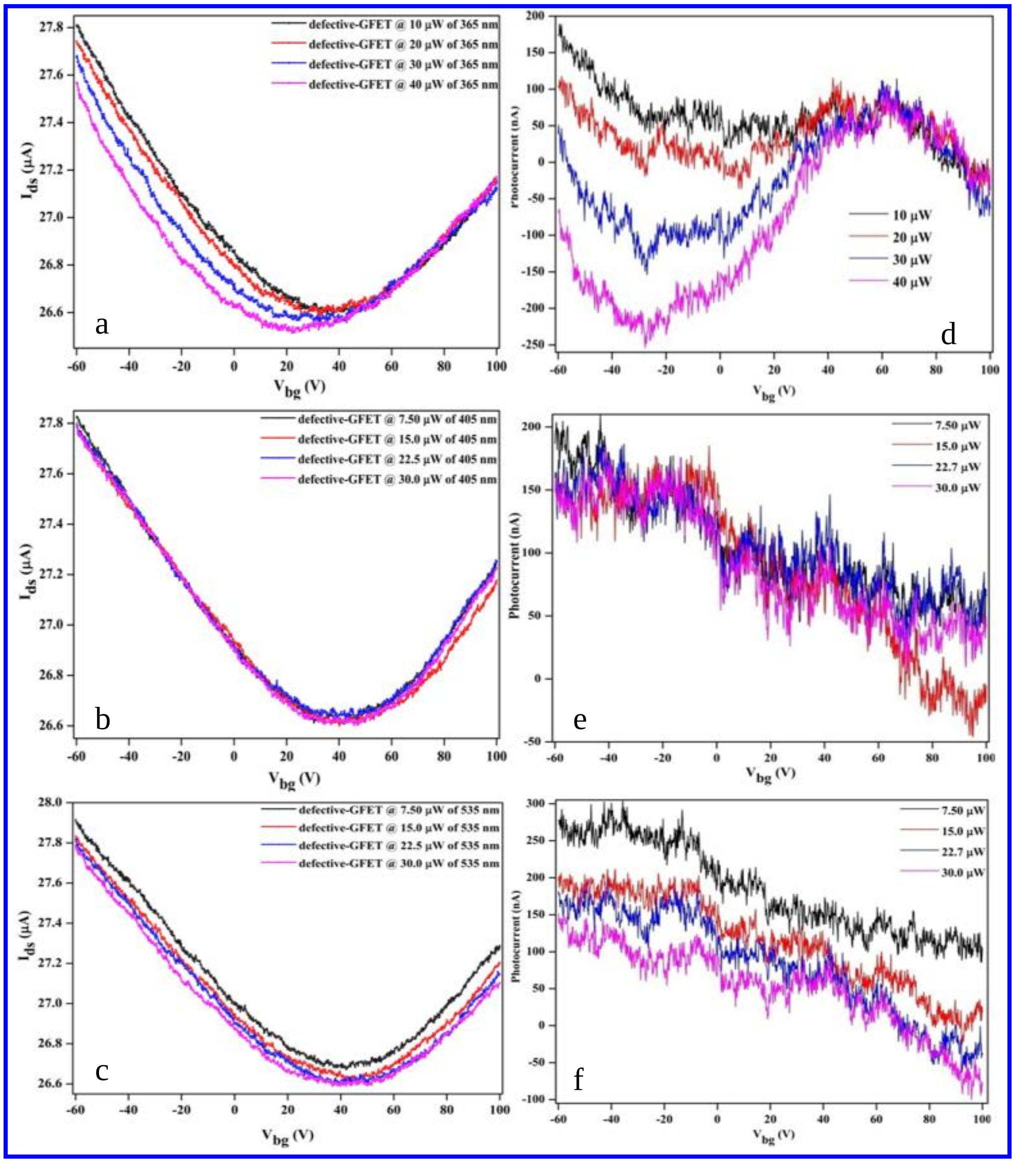

Fig.6.4. (a) –(c) Transfer curves of the defective-GFET device under different powers of 365, 405 and 535 nm light illumination respectively. (d-f) Gate dependent photocurrent of the defective-GFET device under different powers of 365, 405 and 535 nm light illumination respectively.

More insight into the Dirac point shifting and photoresponing behavior of the defected-GFET, we measured the gate dependence of photocurrent at different wavelength and power see Fig.6.4a-c. The defected-GFET shows the strong photogating effect and gate modulation, over UV and visible region. The power dependent photocurrent curves were extracted from Fig.6.3a-c and are plotted in Fig.6.4d-f. Here the photocurrent, lack in the polarity reversal, attributed to the accumulation of a large amount of holes (absorption of oxygen molecules) [9,13] in defected graphene causing the symmetry.

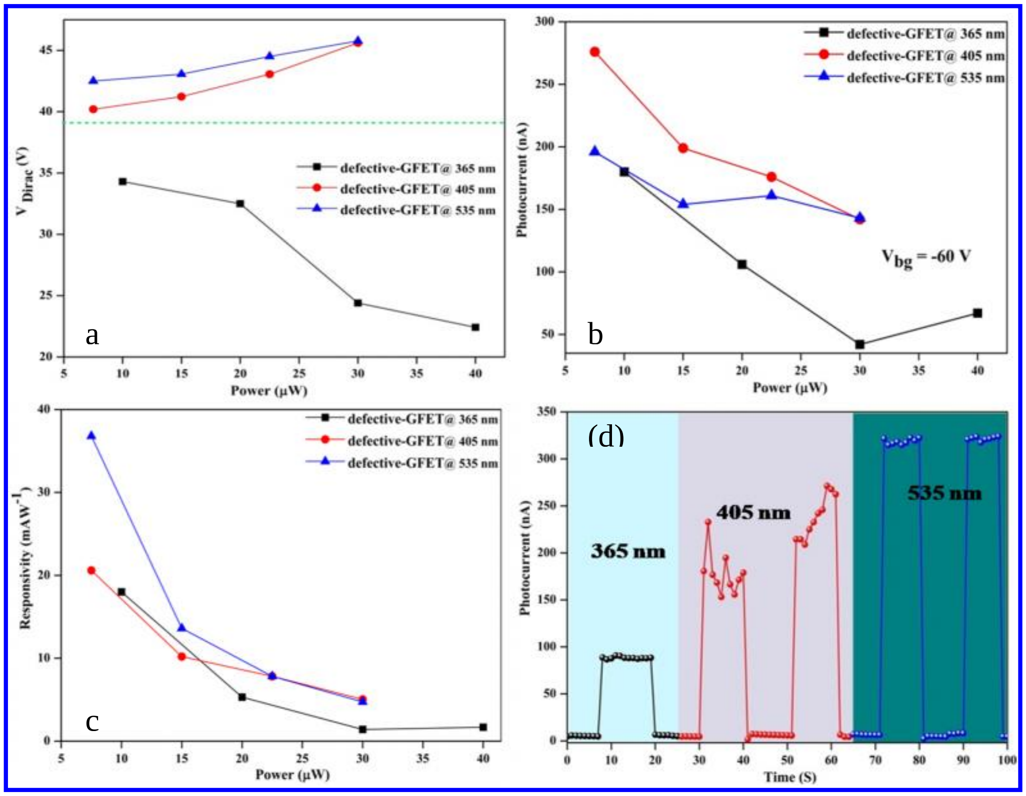

Fig.6.5. (a) Power dependent Dirac point shift (V_{Dirac}) in the defective-GFET device (green dotted line indicates the Dirac point at dark). (b) Power dependent photocurrent of the defective-GFET device at V_{bg} of -60 V. (c) Measured photoresponsivity versus powers under different illumination wavelength. (d) Time-dependent photocurrent spectra of the defective-GFET device under UV (365 nm) and visible (405 and 535 nm) light irradiation for a bias of 1 V, at V_{bg} = 0 V.

The photoinduced Dirac point shift (V_{Dirac}) in the defected-GFET with different powers of UV (365 nm) and visible (405 and 535 nm) light are shown in Fig.6.5a, a green dotted line indicates the Dirac point position in dark. When the device illuminated with visible (405 and 535 nm) light, the transferring of photogenerated holes to the defected graphene, induces further p-doping effect, which leads to up-shift the V_{Dirac}, to 45 V for the power of 30 μW, the shift in the visible wavelengths (405 and 535 nm) are almost identical. Interestingly, the device showed down-shifts (towards negative), under UV (365 nm) light and Dirac point shifted to 22 V of V_{bg} for the power of 40 μW, which suggesting that when the UV light is turned on the photo-induced desorption process starts and the rate of the process is increasing, when the incident power increases resulted in n-doping (hole removal) effect.[13,14] Fig.6.5b shows the photocurrent of the defected-GFET device as a function of incident power with various illumination wavelengths, at V_{bg} of -60 V, where the V_{ds} is 10 mV. The photocurrent of the device decreases with respect to the power, for all illumination wavelengths, which is due to the high defect density,[13,16] trapping of holes in the defected sites[7], as well as the fast recombination of photo-generated charge carriers.[3] The high illumination power, required high external bias voltage to separate the excitons, before they recombine[17], which may increase the photoresponse of the device, because the device shows linear reponse in the I_{ds}-V_{ds} curve see Fig.6.3d.

The significant parameters to determine the capability of a photodetector or photoconductor, is responsivity (R) which depends on the electrical output to the optical input. R is defined as[2,7,9]

$$R\left(AW^{-1}\right)=\frac{\left(I_{light}-I_{dark}\right)}{P_{opt}} \qquad (6.1)$$

Where, I_{light}, I_{dark}, P_{opt}, are current under illumination, current in dark, and incident light power, respectively. The responsivity of the defected-GFET device is estimated using Eq. (1). The device shows high responsivity, under low excitation power, we achieved the value of 37, 21 and 18 mAW^{-1} for 535, 405, and 365 nm wavelengths, respectively (see Fig.6.5c) at 10 mV of V_{ds}. This high photoresponsivity of the device is due to the effective separation of photogenerated electron-hole pair in the defected graphene surface,[3,7] now its clear that the defected-GFET device has the capability of converting the incident photons into electrical signal for broad spectral wavelength. The photoresponsivity of our device is very much comparable with the previous reports, see Table 6.1, where the FET based photoresponsivity of the mechanically exfoliated graphene layers was compared over the UV and visible region.

Table 6.1. Comparison of the photoresponsivity of graphene transistors in the UV and visible region.

Detector type	**Active layer**	**Wavelength**	**Responsivity (R)**	**Reference**
Visible	SLG	632.8 nm	1 mA/W	18
	SLG	532 nm	~10 mA/W	19
	BLG	480 nm-750 nm	~1.5 mA/W	20
	SLG	690 nm	0.25 mA/W	21
	SLG/$FeCl_3$-FLG	532 nm	~0.1 V/W	22
	SLG/metal nanostructures	457-785 nm	~10 mA/W	23
	SLG/chlorophyll	683 nm	~1.1x10^6A/W	24
	SLG/Argon plasma	535 nm	~37 mA/W	Our device
	SLG/Argon plasma	405 nm	~21 mA/W	Our device
UV	SLG/MoS_2	635 nm	5x10^8A/W	25
	SLG/ZnO QDs	325 nm	10^4A/W	26
	SLG/Argon plasma	365 nm	~18 mA/W	Our device

Fig.6.5d shows the time-dependent photocurrent measurement of the defective-GFET device under UV (365 nm) and visible (405 and 535 nm) light modulation with 1V bias voltage, at room temperature, where the V_{bg} is 0 V. Here the turn-on and turn-off time of the light source was 10 s. The device showed excellent stability and reproducibility over UV and visible region see Fig.6.6. The ratio of I_{light} to I_{dark} increased as the illumination wavelength, increased, having values of 86, 240, and 320, for wavelengths of 365, 405, and 535 nm respectively. The device showed a fast switching, when the light source was turned on, the photocurrent reaches its maximum level within in 0.9 Sec and the decay time of the device is 1 Sec, these are very much comparable to the previous reports.[16,13]The high photoresponsivity and fast switching time in the defective-GFET devices suggest that which can be employed for the photodetection application.

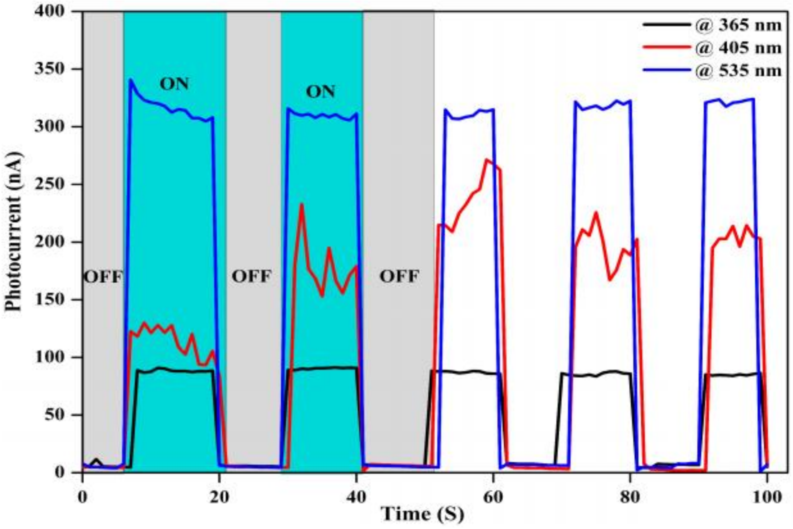

Fig.6.6. The time-dependent photocurrent of the defective-GFET device with multiple on/off cycles, under UV (365 nm) and visible (405 and 535 nm) light illumination for the bias voltage of 1 V, at $V_{bg} = 0$ V.

6.4 Conclusions

In this chapter, we demonstrated an enhanced, stable, wavelength dependent and gate-tunable photoresponse in graphene by inducing defects by plasma irradiation. Raman, X-ray photoelectron spectroscopy and electrical transport measurement showed that plasma irradiation imposes p-doping. The effective separation of photo-induced charge carriers in the defect site enhances the photoresponse of the defective –GFET device , except the higher power regions. The device shows high responsivity, under low excitation power, the maximum photoresponsivity of 37 mAW^{-1} for 535 nm illumination which is ~3 times higher than that of pristine. Photoinduced molecular desorption under 365 nm, UV light illumination causes the responsivity to 18 mAW^{-1}. The photoresponse of the defected graphene could be further enhanced by controlling the defect density. This study shows that the tunable photodetector with high responsivity is feasible by introducing an artificial defect on graphene surface.

References

[1] Liu, C.H.; Chang, Y.C.; Norris, T. B.; Zhong, Z. Graphene Photodetectors with Ultra-Broadband and High Responsivity at Room Temperature *Nature Nanotech.* 9, (2014), 273-278.

[2] Li, J.; Niu, L.; Zheng, Z.; Yan, F. Photosensitive Graphene Transistors *Adv. Mater.* 26, (2014), 5239-5273.

[3] Zhang, Y.; Liu, T.; Meng, B.; Li, X.; Liang, G.; Hu, X.; Wang, Q.J. Broadband High Photoresponse from Pure Monolayer Graphene Photodetector *Nat Commun.* 4, (2013), 1811.

[4] Mak, K. F.; Ju, L.; Wang, F; Heinz, T. F. Optical Spectroscopy of Graphene: from the Far Infrared to the Ultraviolet *Solid State Commun.* 152, (2012), 1341-1349.

[5] Sargent, E.H. A Sensitive Pair *Nat Nanotechnol.* 7, (2012), 349-350.

[6] Thiyagarajan, K.; Saravanakumar, B.; Mohan, R.; Kim, S.J. Self-Induced Gate Dielectric for Graphene Field-Effect Transistor *ACS Appl. Mater. Interfaces* 5, (2013), 6443-6446.

[7] Thiyagarajan, K.; Ananth, A.; Saravanakumar, B.; Mok Y. S.; Kim, S. J. Plasma-Induced Photoresponse in Fewlayer Graphene *Carbon 73,* (2014), 25-33.

[8] Iqbal, M. Z.; Khan, M. F.; Iqbal, M. W.; Eom, J. Tuning the Electrical Properties of Exfoliated Graphene Layers using Deep Ultraviolet Irradiation *J. Mater. Chem. C*, 2, (2014) 5404-5410.

[9] Cheng, S.H.; Weng, T.M.; Lu, M.L.; Tan, W.C.; Chen, J.Y.; Chen, Y.F. All Carbon-Based Photodetectors: An Eminent Integration of Graphite Quantum Dots and Two Dimensional Graphene *Sci. Rep.* 3, (2013), 2694.

[10] Rousseau, B.; Szwarckopf, H. E.; Thomann, A. L.; Brault, S. P. C-Atom Displacements on HOPG Surface Under Plasma Low-Energy Argon-Ion Bombardment *Appl. Phys. A* 77, (2003), 591-597.

[11] Su, Y.; Pei, S.; Du, J.; Liu, W.B.; Liu, C.; Cheng, H.M. Patterning Flexible Single-Walled Carbon Nanotube Thin Films by an Ozone Gas Exposure Method *Carbon* 53, (2013), 4-10.

[12] Yan, J.A.; Chou, M. Y. Oxidation Functional Groups on Graphene: Structural and Electronic Properties *Phy. Rev.B* 82, (2010), 125403.

[13] Kang, C.G.; Lee, S.K.; Choe, S.; Lee, Y. G.; Lee, C.L.; Lee, B. H. Intrinsic Photocurrent Characteristics of Graphene Photodetectors Passivated with Al_2O_3 *Optics Express* 21, (2013), 23391-23400.

[14] Sun, P.; Zhu, M.; Wang, K.; Zhong, M.; Wei, J.; Wu, D.; Cheng, Y.; Zhu, H. Photoinduced Molecular Desorption from Graphene Films. *Appl Phys Lett* 101, (2012), 053107.

[15] Breusing, M.; Ropers, C.; Elsaesser, T. Ultrafast Carrier Dynamics in Graphite *Phys Rev Lett.* 102, (2009), 086809.

[16] Gowda P.; Sakorikar, T.; Reddy, S. K.; Ferry, D.B.; Misra, A. Defect-Induced Enhancement and Quenching Control of Photocurrent in Few-Layer Graphene Photodetectors *ACS Appl. Mater. Interfaces* 6, (2014), 7485-7490.

[17] Gowda, P.; Mohapatra, D. R.; Misra, A. Enhanced Photoresponse in Monolayer Hydrogenated Graphene Photodetector *ACS Appl. Mater. Interfaces*, 6, (2014), 16763-16768.

[18] Xia, F.; Mueller, T.; Mojarad, G. R.; Freitag, M.;. Lin, Y.; Tsang, J.; Perebeinos, V.; Avouris, P. Photocurrent Imaging and Efficient Photon Detection in a Graphene Transistor *Nano Lett.* 9, (2009), 1039-1044.

[19] Park, J.; Ahn, Y.H.; Vargas, C.R. Imaging of Photocurrent Generation and Collection in Single-Layer Graphene *Nano Lett.* 9, **(**2009), 1742-1746.

[20] Lemme, M.C.; Koppens, F.H.L.; Abram, L.F.; Rudner, M.S.; Park, H.; Levitov, L.S.; Marcus, C.M. Gate-Activated Photoresponse in a Graphene p-n Junction *Nano Lett,* 11, (2011), 4134-4137.

[21] Freitag, M.; Low, T.; Xia, F.; Avouris, P. Photoconductivity of Biased Graphene *Nature Photonics*, 7, (2013), 53-59.

[22] Withers, F.; Bointon, T. H.; Craciun, M. F.; Russo, S. All-Graphene Photodetectors. *ACS Nano* 7, (2013), 5052-5057.

[23] Echtermeyer, T.J.; Britnell, L.; Jasnos, P.K.; Lombardo, A.; Gorbachev, R. V.; Grigorenko, A.N.; Geim, A.K.; Ferrari, A.C.; Novoselov, K.S. Strong Plasmonic Enhancement of Photovoltage in Graphene *Nat Commun.* 2, (2011), 458.

[24] Chen, S.Y.; Lu, Y. Y.; Shih, F.Y.; Ho, P.H.; Chen, Y.F.; Chen, C. W.; Chen Y.T.; Wang, W. H. Biologically inspired graphene-chlorophyll phototransistors with high gain *Carbon* 63, (2013), 23-29.

[25] Roy, K.; Padmanabhan, M.; Goswami, S.; Sai, T. P.; Ramalingam G.; Raghavan, S.; Ghosh, A. Graphene–MoS_2 Hybrid Structures for Multifunctional Photoresponsive Memory Devices *Nat. Nanotechnol.* 8, (2013), 826-830.

[26] Guo, W.; Xu, S.; Wu, Z.; Wang, N.; Loy, M. M. T.; Du, S. Oxygen-Assisted Charge Transfer between ZnO Quantum Dots and Graphene *Small* 9, (2013), 3031-3036.

CHAPTER VII

Graphene-CdSe Hybrid Device for Photosensing Application

7.1 Introduction

Graphene is an exceptional materials with excellent electronic properties, which weakly absorbs light (2.3%) and the absence of a gain mechanism limited the photoresponsivity of the pristine graphene.[1] Efforts have been made to improve the photoresponsivity of graphene by either engineering the graphene carrier dynamics or coupling the graphene to optical absorption media.[2]

In this chapter, we show the enhanced photoresponsivity of graphene device, when the optical absorption media (CdSe quantum dots) attached over the surface (graphene) though diazonium salts. The electrical transformation and photoconducting ability of the graphene-CdSe QDs hybrid device shows superior results, when compared to the pristine devices.

7.2 Experimental Section

Ribbon like graphene layer (RGL) is cleaved from HOPG by using scotch tape and were transferred to an SiO_2/Si substrate for detail refer section 2.2. Optical microscope (Fig.7.1a) and micro Raman spectroscopy were used to characterize the thickness of the RGL flakes (refer section 2.2). The RGL device was fabricated by evaporating thin layer Pt (3 nm- sputter coating) and a 100 nm-thick gold (Au-thermal evaporator) layer electrodes directly on top of the selected, large-sized RGL using hardmasks. Finally the RGL device were annealed at 250 °C under in an Ar atmosphere for 1 hr to improve the adhesion of electrodes. This photoresist free method ensures the electrical characteristics were not affected by the electrode fabrication process.

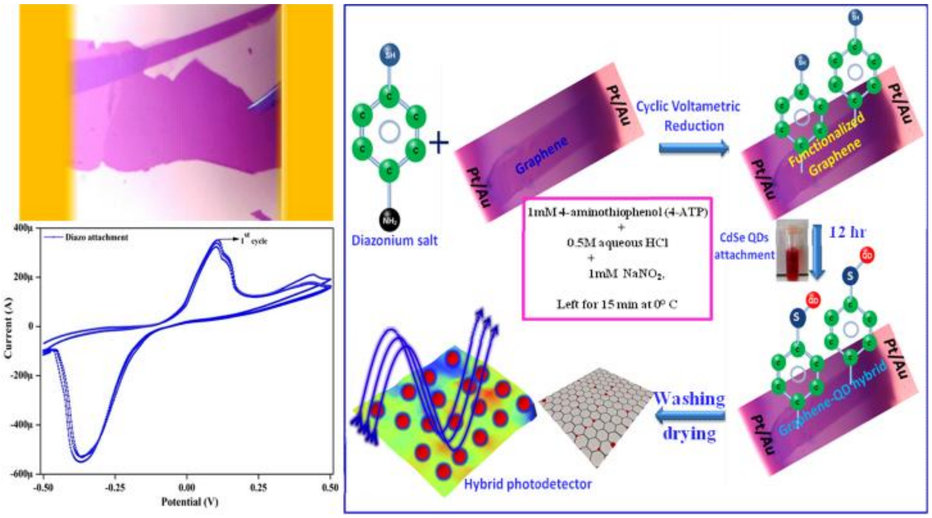

Fig.7.1. (a) Optical microscopic image of the fabricated device. (b) Cyclic –volt metric reduction of Diazonium salt. (c) Schematic diagram of the functionalization process.

For the functionalization of graphene with diazonium salts, the 4-aminothiophenol (Sigma-Aldrich, 99%) were used without further purification, here the 1mM 4-aminothiophenol was solubilized in 0.5M aqueous HCl, and 1mM sodium nitrite were added to generate the aryl diazonium salt in the electrochemical cell (in situ). The mixture was degassed and left to reacts for about 15 min at 0°C. The electrochemical reductive modification of graphene surface with in situ generated 4- TPdiazonium salt was conducted by applying a potential to the electrode between 0.5V and −0.5V for two to four cycles see Fig.7.1b. Subsequently, the electrodes were rinsed with copious amounts of Milli-Q water and dried under a stream of argon prior to the next step. Then the 4- TP modified graphene surface was immersed in CdSe solution for 12 hr at room temperature to form the CdSe immobilized Graphene surface by the formation of S–CdSe bond between the 4- TP layers and CdSe. Fig.7.1c, is the schematic diagram of the functionalization process. Finally the hybrid device is washed with water and dried using the N_2 gas.

7.3 Results and discussion

Before the fabrication of hybrid device, we have characterized the as synthesized CdSe QDs graphene layers to ensure their pristine properties. The UV-vis absorption spectrum of CdSe QDs dispersed in toluene is shown in Fig.7.2a, which exhibits the excitonic transition at 566 nm corresponding to the 1S transition.[3] Where the two insets Figures in are the fluorescing image of CdSe QDs, excited by 365 nm UV light, suggesting that the size of the QDs will be in the range of 4-5 nm.

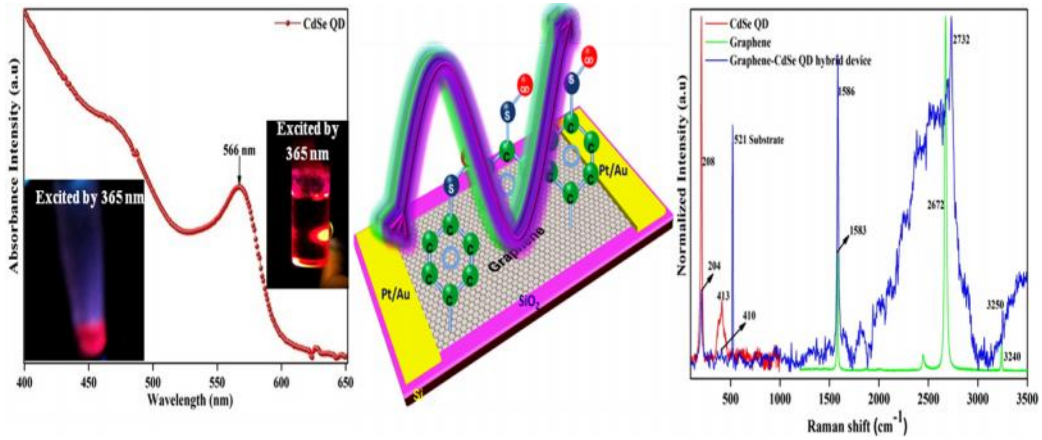

Fig.7.2. (a) UV-Vis absorbance spectrum of CdSe QDs and the fluorescing image under 365 nm light illumination. (b) Schematic diagram of the hybrid device (c) micro Raman spectrum of hybrid device along with the pristine ones.

The hybrid device is formed through the functionalization process which starts with the attachment of diazonium compound to the graphene surface by electrochemical reduction. Where the delocalized electron is transferred to the diazonium cation from the graphene, which releases the N_2 molecules and becoming an aryl radical, which forms a covalent bond with a carbon atom present in the honeycomb lattice.[4] Here the thiol functional group is readily available at the head side of the which favors the CdSe QDs attachment which forms a hybrid device structure shown in Fig.7.2b.

The micro Raman spectrum of CdSe QDs (red color), pristine graphene (green color) and the hybrid device (blue color) are shown in Fig.7.2c. The peak corresponds to the A1 longitudinal –optical (LO) mode of the CdSe QDs appears at ~208 cm^{-1} and 2LO photon peak appears at ~413 cm^{-1}, whereas in case of hybrid device these peaks shifted to ~204 and ~410 cm^{-1} respectively attributed to the homogenization attachment of CdSe QDs on graphene surface and also due to the relaxation of momentum conservation[5,6] There is no hint of D peak and the appearance of G and 2D peaks indicates that the pristine device was lucratively fabricated on SiO_2/Si substrate.[7] The peaks shift with broadening along with the hint of D peak in the hybrid device suggest that the CdSe QDs is successfully attached over the graphene lattice, which serves as a light absorbing medium.

We have monitored the electrical changes of the pristine graphene device (before diazo attachment), after functionalization process (after diazo attachment), through current-voltage (I-V) characteristics which is shown in Fig.7.3a, where the conductivity of the device is considerably decreasing due to the formation of σ bond between diazonium compound and graphene lattice. The attachment of CdSe QD (hybrid device) further decreases in the conductivity (increases the resistance) of the device, corroborate that the light absorbing media was successfully bonded to the graphene through diazonium compound see Fig.7.3b. To explore the photoresponse characteristics of the hybrid device, we carried out photocurrent measurement under ambient conditions at an applied bias voltage of 1 V for different illumination wavelengths see Fig.7.3b. We observed three orders of magnitude improvement in the photocurrent in the hybrid device attributed to the effective separation and transport of photogenerated carriers (electron – hole pairs)[8]. Here the light absorption was taking place in the CdSe QDs, whereas the graphene layer beneath the CdSe QDs are acting as a carrier extractor as well as a transporting layer. The maximum photocurrent was observed under 535 nm illumination; the photocurrent decreases when wavelength decrease.

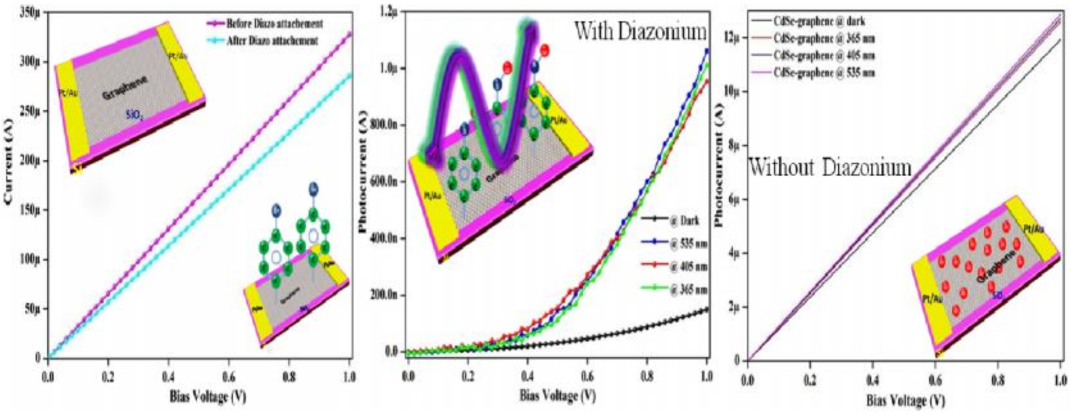

Fig.7.3. (a) Current –Voltage *(I-V)* characteristics of graphene device before and after functionalization with Diazonium salt, and the insets are the schematics of the corresponding devices. (b) and (c) Photoresponse *I–V* curve with and without diazonium salt, (Inset shows a corresponding schematic diagrams).

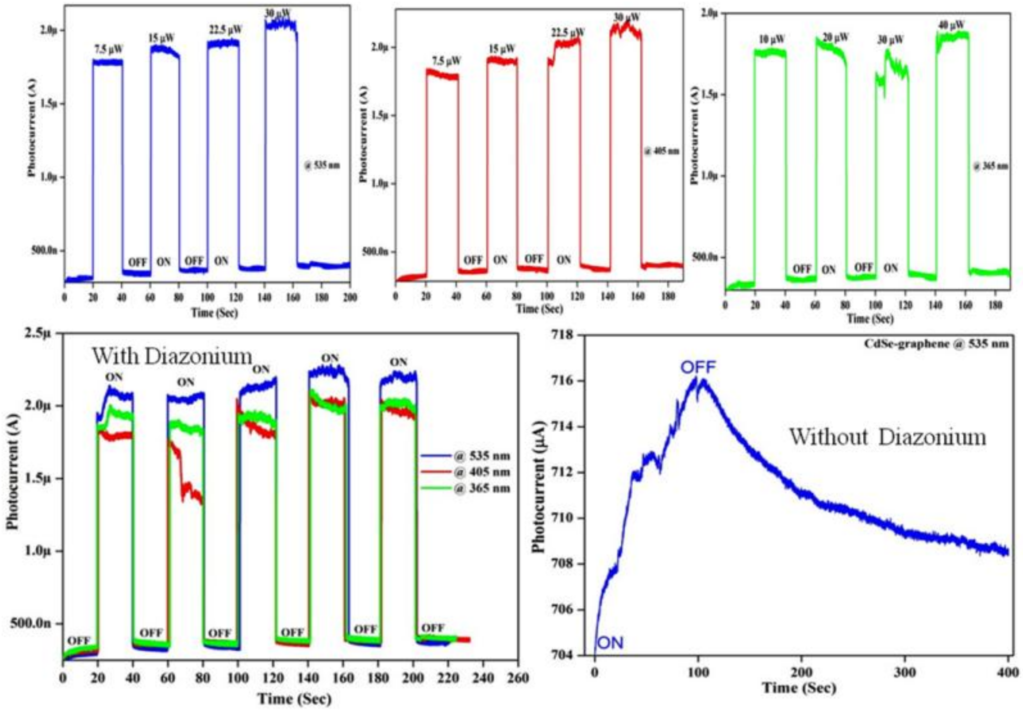

Fig.7.4. (a)- (c) The power dependence photoresponse of the hybrid device under 535, 405, and 365 nm wavelength light illumination at 1 V bias voltage. (d) and (e) Comparison of time dependent photocurrent response of the device with and without Diazonium salt attachment at 1 V bias voltage of 1 V.

Fig.7.4a shows the time-dependent photocurrent measurement of the hybrid device under UV (365 nm) and visible (405 and 535 nm) light irradiation at 1 V bias, with multiple on/off cycles. The turn-on and turn-off time of the light source was 10 s. The device exhibited excellent stability and reproducibility over the UV and visible region. When the light source was turned on, the photocurrent reached its maximum within a millisecond (ms), where the ratio I_{light} to I_{dark} increased as the illumination wavelength, increased. The incident power dependence photoresponse of the hybrid device are shown in Fig.7.4b–d at different wavelength illuminations. Linear behavior was observed for the visible and UV wavelengths, indicating the broader spectral response of graphene. The device without diazonium compound shows the poor response see Fig.7.4e, attributed to the recombination of photogenerated carriers due to the lack of transporting pathways.

The photocurrent as a function of incident power with various illumination wavelengths is shown in Fig.7.5a. The photocurrent of the device increased linearly with the incident power for all illumination wavelengths, whereas in case of visible light the photoresponse is identical due to the absorption behavior of CdSe QDs.

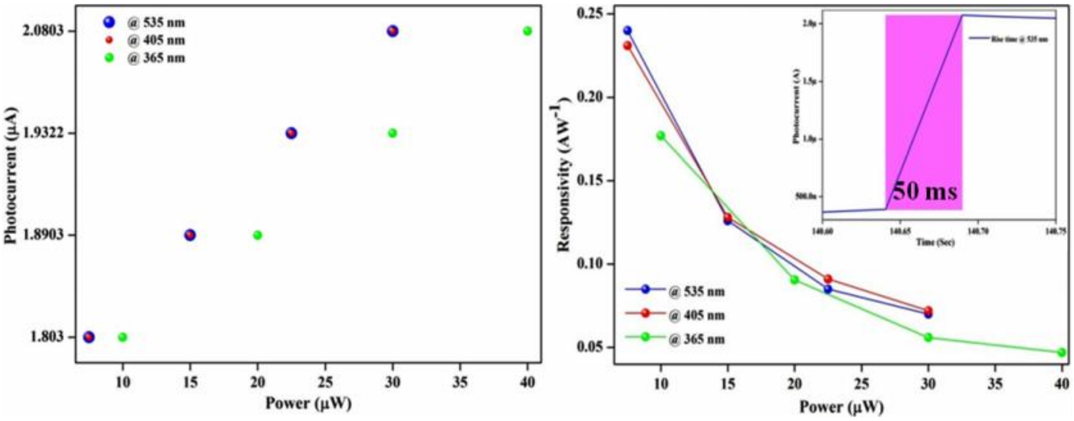

Fig.7.5. (a) The power-dependence photoresponse of the hybrid device at different wavelength. (b) Responsivity of the hybrid device as a function of the incident power. Inset is the response time of the device under 535 nm visible-light irradiation.

We have used responsivity (R) as a significant parameter to determine the capability of the hybrid photodetector, which depends on the electrical output to the optical input. R is defined as[2,7,12]

$$R\left(AW^{-1}\right)=\frac{\left(I_{light}-I_{dark}\right)}{P_{opt}} \qquad (7.1)$$

Where, I_{light}, I_{dark}, P_{opt}, are current under illumination, current in dark, and incident light power, respectively. The responsivity of the hybrid device is estimated using Eq. (1). The device shows high responsivity, under low excitation power, we achieved the value of 0.24, 0.23 and 0.17 AW^{-1} for 535, 405, and 365 nm wavelengths, respectively see Fig.7.5b. at 10 mV of V_{ds}. This high photoresponsivity of the hybrid device is due to the effective separation and transporting of the photogenerated charge carriers through the aryl compound to the graphene. The response time of the hybrid device is 50 ms under 535 nm light illumination shown in the inset in of Fig.7.5b, which is comparatively high due to the long charge separation, which is crucial for enhancing the photoresponse of the device.

7.4 Conclusions

In this chapter, we have fabricated graphene – CdSe QDs hybrid device by immobilizing CdSe QDs on graphene surface through electrochemical reduction of diazonium salt and demonstrated an enhanced, stable, wavelength dependent photosensor. Photoresponsivity of the hybrid device remarkably improved when compare to the pristine device, which shows 0.24 AW^{-1} under 535 nm light illumination. Long time separation and effective transporting of photogenerated charge carriers by the aryl compound is the reason for this high responsivity.

References

[1] Sargent EH. Photodetectors: A sensitive pair. Nat Nanotechnol, 7, (2012), 349-350.

[2] Konstantatos G, Badioli M, Gaudreau L, Osmond J, Bernechea M, Pelayo Garcia de Arquer F, Gatti F, Koppens FHL. Hybrid graphene–quantum dot phototransistors with ultrahigh gain. Nat Nanotechnol 7, (2012), 363-368.

[3] Prabakar K, Minkyu S, Inyoung S, Heeje K. CdSe quantum dots co-sensitized TiO_2 photoelectrodes: particle size dependent properties J. Phys. D: Appl. Phys. 43, (2010), 012002.

[4] Jung M-H, Chu M-J. Comparative experiments of graphene covalently and physically binding CdSe quantum dots to enhance the electron transport in flexible photovoltaic devices Nanoscale, 6, (2014), 9241-9249.

[5] Chikate, R. C, Kadu, B. S, Damle, M. A. Nanoengineered CdSe quantum dot–montmorillonite composites: an efficient photocatalyst under visible light irradiation, RSC Adv., 4, (2014), 35997-36005.

[6] Liao, C, Zhu, X. Energy transfer from CdSe quantum dots to graphene, Proc. of SPIE, 9068, (2014), 90680Q-1.

[7] Thiyagarajan, K. Saravanakumar, B, Mohan, R, Kim, S.J. Self-Induced Gate Dielectric for Graphene Field-Effect Transistor *ACS Appl. Mater. Interfaces* 5, (2013), 6443-6446.

[8] Guo, W.; Xu, S.; Wu, Z.; Wang, N.; Loy, M. M. T.; Du, S. Oxygen-Assisted Charge Transfer between ZnO Quantum Dots and Graphene *Small* 9, (2013), 3031-3036.

CHAPTER VIII

Self-induced Gate Dielectric for Graphene Field-Effect Transistor

8.1 Introduction

Graphene field-effect transistor (GFET) with different gate architectures (back-, top- and side-gate) have their own merits and de-merits. Gate oxide layer (dielectric) is an essential part of a transistor compare to the graphene channel. Depositing a high-quality gate dielectrics, without introducing defects on the graphene lattice is a challenging task in the transistor fabrication process.[1] Although, atomic-layer deposition (ALD) is the most common technique to deposit high-*k* dielectrics, which requires an initial functionalization process prior to the deposition. This results in breaking of chemical bonds, defective structure and even doping of unwanted impurities on the graphene lattice which can significantly affect the device mobility, on/off ratio, conductance, sub-threshold swing, and may also increase the noise level of G-FETs.[1,3]

In this chapter, we show how to overcome this performance degradation problems of graphene device, by developing a new type of G-FET device based on ZnO microwire as a top-gate electrode with self-induced dielectric layer. The surface adsorbed[4] oxide layer of ZnO act as dielectric layer and the high-*k* value of ZnO provides enough capacitance to control the active graphene channel.

8.2. Fabrication of the avant-garde GFETs

Fig.8.1a shows a schematic of the graphene/ZnO micro wire hybrid device. Graphene were prepared from HOPG by micromechanical cleavage method and were transferred onto SiO_2 (300 nm)/Si substrate and silver (paste) electrodes were made on both sides of graphene. ZnO microwires with diameters of ~5 μm, a length of 20-150 μm have been chosen and cautiously placed (vertically) over the graphene layer without damaging the crystal lattice for ZnO microwire growth please refer section 2.5. The device were heat on a hot plate for 150 °C to remove the surface adsorbed oxygen, silver contact was made on both sides of the hot microwire. The device was cool down to room temperature to re-adsorb the oxygen on the remaining parts of the ZnO microwire making it insulating and the wire underneath the silver contact remain more conducting than the rest of the wire. Field emission scanning electron microscopy (FESEM) image of the fabricated self-induced top-gated (ZnO microwire) graphene-FET (STG-FET) was shown in Fig.8.1b.

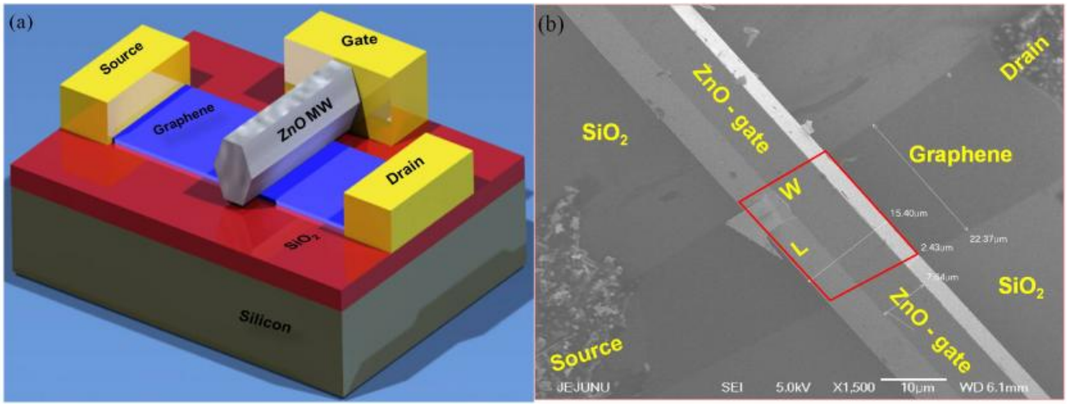

Fig.8.1. (a) Schematic of graphene FET device with ZnO microwire as a self-induced top-gate electrode, (b) Typical FE-SEM image of self-induced top-gated graphene-FET (STG-FET).

8.3 Results and discussion

After the fabrication of STG-FETs, Raman spectroscopy measurement was done with 514 nm Ar^+ ion laser as an excitation light source using Horiba Jobin Yvon LabRAM HR800 system. Raman spectrum of ZnO microwire is illustrated in Fig.8.3a manifest the material quality and wurtzite crystal structure of the synthesized ZnO microwire. Zone center optical phonon modes for the Wurtzite crystal structure of ZnO microwire are $A_1 + 2B_1 + E_1 + 2E_2$.[5] Group theory predicts that the two B_1 modes are Raman inactive and all the other modes are first-order Raman-active. The heavier Zn sublattice, with non-polar vibrations is the reason for the low-frequency E_2 mode. The high frequency E_2 mode predominantly involves the oxygen atoms. The second order Raman peak at 331 cm^{-1} is attributed to the acoustic phonons.[6] The two peaks at 379 and 410 cm^{-1} in the spectrum correspond to A_1 (TO) and E_1 (TO) modes respectively. The peaks corresponds to the LO modes are not present in the obtain spectrum. The peaks at 100 and 437 cm^{-1} are associated to the two non polar Raman active $2E_2$ (low and high) modes.[7] The line width of E_2 (high) mode is about 7.5 cm^{-1}, while the line width of E_2 (low) is about 2.4 cm^{-1}. The corresponding peaks, line width values of the Raman spectrum confirm that the top-gated material is ZnO microwire.

Fig.8.2b shows the Raman spectrum of single layer graphene. Absence of D peak (defect) reveals the material quality. The full width at half maximum (FWHM) of 2D-peak is ~ 22 cm^{-1} and the intensity ratio between 2D and G peaks is 2.9 these values indicates that, the STG-FET device was successfully fabricated on a SiO_2/Si substrate without causing any material damage. The inset in Fig.8.2 is the optical microscopy image of the fabricated STG-FET device. ZnO microwire plays an immense role, which defines the channel length (with respect to the width of the graphene layer), the diameter of the microwire sets the channel width and also working as a top-gate electrode. The active channel width (W) and length (L) of the STG-FET device is show in Fig.8.1b. The surface oxide or depletion layers of ZnO microwire is pretended as gate dielectrics. The electrical characteristics of the device were measured by Agilent, B1500 A semiconductor parameter analyzer.

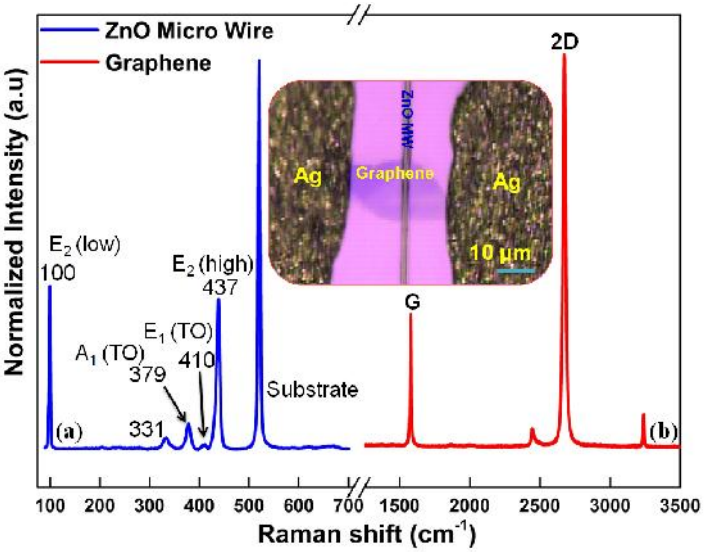

Fig.8.2. Raman spectrum (a) ZnO microwire, (b) single layer graphene. Inset shows the Optical microscopy image of a STG-FET device.

Gate oxide or depletion layer thickness of the STG-FET can be approximated by,[8,9]

$$t = \left(\frac{2\pounds_0 \pounds_{ZnO} V}{eN_D} \right)^{1/2} \qquad (8.1)$$

Here $£_o$ is the permittivity of free space, $£_{ZnO}$ is the dielectric constant of the top-gated ZnO microwire ~ 8.7,[8] e is electron charge, V is applied potential with order of 1 V and N_D is the free electron carrier density ~10^{17} cm^{-3}. The thickness of the top-gate dielectric layer is approximated to be 98 nm. The top-gate capacitance (C_{TG}) of the STG-FET is estimated to be C_{TG} = 78 nF/cm^2, corresponding to a relative dielectric constant of ~8.7 with a dielectric layer thickness of ~98 nm for the ZnO microwire.

Electrical transport studies of fabricated STG-FET were carried out in ambient conditions. Self-aligned gate-dependent drain current (I_{ds}) versus Drain voltage (V_{ds}) is shown in Fig.8.3a. The applied top-gate voltage was increased from -30 to 30 V with the step of 10 V. Fig.8.3a clearly shows that the gate voltage increases towards positive direction the device conductance decreases, which is due to the influence of surface adsorbates.[10,11] In ambient conditions, the free charge carriers of ZnO microwire were depleted by the surface adsorbates. Consequently the electronic transport property of top-gated ZnO microwire is dominated by the injected electrons. Absorbance of O_2 from ambient condition form a depletion layer over the ZnO microwire surface with a thickness of ~98 nm reduces the carrier concentration of ZnO microwire.[8,11]

The top - gate voltage induced carrier concentration is given by $n = \frac{£_o £_{ox} V_{TG}}{t_{ox} e}$, where e is the electron charge, V_{GT} is a top-gate voltage. For typical V_{GT} = 50 V the formula yields n = 2.45 x 10^{12} cm^{-2} for STG-FET device. The transfer characteristics of the drain –source current (I_{ds}) Vs self-induced top-gate voltage (V_{TG}) of STG-FET device at V_{ds} = 100 mV, and 500 mV is shown in Fig.8.3b. At V_{TG}= 0 V the device shows p-channel operation and a perfect symmetric ambipolar behavior were observed with the Dirac point located at 5 V of gate voltage. We observed one order increment in drain current (I_{ds}) with respect to drain voltage (V_{ds}). The STG-FET device can delivers an on-current of 175 µA at V_{ds}= 500 mV for V_{TG} = - 40 V and the room temperature on/off current ratio of the device is 55 at V_{ds} = 500 mV.

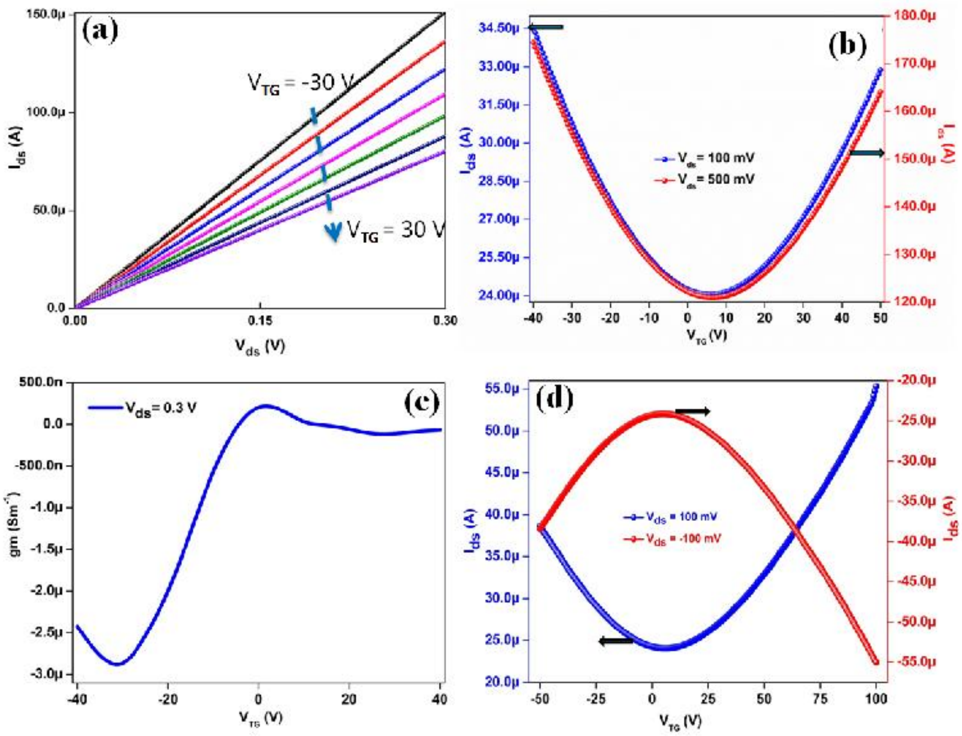

Fig.8.3. (a) Output characteristic (I_{ds} –V_{ds}) of STG-FET recorded at different gate voltage from -30 to 30 V with the step of 10 V, (b) The transfer characteristics (I_{ds} - V_{TG}) of STG-FET at the drain source voltage of 100 mV, 500 mV during the sweep of top-gate bias from -40 V to 50 V, (c) The transconductance (g_m) of STG-FET as a function of top-gate voltage at V_{ds} of 300 mV. (d) The transfer characteristics of STG-FET at two different channel bias voltage.

Fig.8.3c represents the gate-dependent transconductance of STG-FET, which is defined as $g_m = dI_{ds} /dV_{TG}$ and the transconductance of the device significantly varied with respect to the applied gate potential. The peak transconductance values are found to be 275 nS for the positive branch (n-type) and 2.9 µS for the negative branch (p-type) of

$V_{TG.}$ The hole branch current is larger than electron branch current, which leads to high field effect mobility of 3588 $cm^2/V.s$ for holes and 340 $cm^2/V.s$ for electron (including the contact resistance). The mobility values are derived through transconductance method, here channel length L is 53.5 μm, and channel width W is 5.5 μm. This huge difference in device mobility arises due to more number of negative charges induced on the ZnO microwire surface by the positive gate voltage, which leads to the increment in oxide layer thickness resulting in the reduction of transconductance. Fig.8.3d shows the transfer characteristics of STG-FET device at different channel bias. At different bias voltage the device delivers the same amount of current. The minimum conductance is reproduced when applying the negative drain voltage. It suggests that the surface induced oxide layer doesn't affect by the channel bias.

Fig.8.4a shows the resistance (R) as a function of top-gate voltage at V_{ds} = 100 mV. The maximum resistance reveals the charge neutrality point (Dirac point) of the device. To calculate the device mobility value, it is necessary to exclude the contact resistance that is comparable to the device channel resistance. Transfer length measurement (TLM) method has been used to measure contact resistance (R_C) of STG-FET with different channel length. Here the graphene channel width or diameter of the ZnO microwire is ~5 μm. The total resistance (R_T), corresponding channel length (L) (R_T - L plot) of the fabricated device is given in Fig.8.4b. The contact resistance of STG-FET device was extracted through a linear fit which intercept at L = 0, gives the total contact resistance $2R_C$ = 2.2 KΩ. The total resistance of the STG-FET device can be expressed with the following relation.[12,13]

$$R_{Total} = \quad 2R_C + \quad R_{Channel} = \quad 2R_C + \quad \frac{L}{We«\sqrt{(n_0^2 + n^2)}} \qquad (8.2)$$

where R_{Total} is the total resistance of the STG-FET device. R_C is the metal/graphene contact resistance. $R_{Channel}$ is the resistance of the graphene channel covered by self-induced top-gate electrode, *e* is electron charge, μ is the mobility of the device, n is the carrier concentration induced in graphene channel by top-gate electrode and n_0 is the residual carrier concentration of graphene; which is generated by charged impurities[14] present in graphene/ZnO microwire interface (n_0 = 2.45 x 10^{11} cm^{-2} for STG-FET device). The channel length is L and the width of the channel is W.

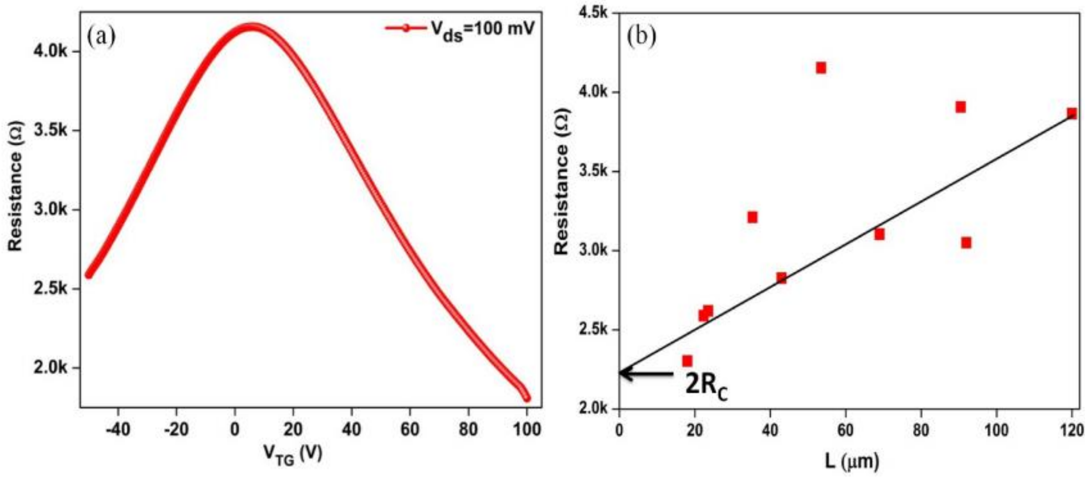

Fig.8.4. (a) The total resistance (R_T) versus self-induced top-gate voltage (V_{TG}), (b) Total resistance versus channel length (R_T - L) plot of STG-FET devices.

The extracted STG-FET device mobility (μ) based on the diffusive transport model state in Eq. (2) is exceeds 1630 cm^2/V.s for holes and 1240 cm^2/V.s for electrons. This present study shows that the ZnO microwire can be used as a top-gate electrode for G-FETs device without depositing any dielectric layer.

8.4 Conclusions

In this chapter we have fabricated a graphene-FET device with ZnO microwire as a top-gate electrode. The depletion layer of the ZnO microwire is acting as a gate dielectric for G-FETs with thickness of ~98 nm. The device characteristics are well agreed with the existing device models. The STG-FET device gives the on on-current of 175 µA, on/off current ratio of 55 and the device mobility exceeds 1630 cm^2/V.s for holes and 1240 cm^2/V.s for electrons at room temperature. Self-induced gate dielectric process prevents the G-FETs from impurity doping, defect formation in graphene lattice and facilitates the fabrication process. The performance degradation of G-FETs can be overcome by our device structure.

References

[1] Liao, L.; Bai, J.; Lin, Y.C.; Qu, Y.; Huang, Y.; Duan, X. High-performance top-gated graphene-nanoribbon transistors uning Zirconium oxide nanowires as high-dielectric-constant gate dielectrics *Adv. Mater.* 22, (2010), 1941-1945.

[2] Lin, Y.M.; Chiu, H.Y.; Jenkins, K. A.; Farmer, D. B.; Avouris, P.; Valdes-Garcia, A. Dual-gated graphene FETs with f_T of 50 GHz *IEEE Electron Device Lett.* 31, (2010), 68.

[3] Lemme, M. C.; Echtermeyer, T. J.; Baus, M.; Kurz, H. A graphene field-effect device *IEEE Electron Device Lett.* 28, (2007), 282-284.

[4] Liao, Z-M.; Lv, Z-K.; Zhou, Y-B.; Xu, J.; Zhang, J-M.; Yu, D-P. The effect of adsorbates on the space-charge-limited current in single ZnO nanowires *Nanotechnology*, 19, (2008), 335204.

[5] Kaschner, A.; Haboeck, U.; Strassburg, M.; Kaczmarzyk, G.; Hoffmann, A.; Thomsen, C.; Zeuner, A.; Alves, H.R.; Hofmann, D.M.; Meyer, B.K. Nitrogen-related local vibrational modes in ZnO:N Appl. Phys. Lett. 80, (2002), 1909.

[6] Chai, G.Y.; Lupan, O.; Rusu, E.V.; Stratan, G.I.; Ursaki, V.V.; Sontea, V.; Khallaf, H.; Chow, L. Functionalized individual ZnO microwire for natural gas detection *Sens. Actuators A* Physical 176, (2012), 64-71.

[7] Chai, G.Y.; Chowa, L.; Lupan, O.; Rusud, E.; Stratan, G.I.; Heinrich, H.; Ursaki, V.V.; Tiginyanu, I.M. Fabrication and characterization of an individual ZnO microwire-based UV photodetector *Solid State Sci.* 13, (2011), 1205-1210.

[8] Liao, Z. M.; Zhang, H. Z.; Zhou, Y. B.; Xu. J.; Zhang, J.M.; Yu, D.P. Surface effects on photoluminescence of ZnO nanowires *Phys. Lett. A* 372, **(**2008), 4505-4509.

[9] Vanheusden, K.; Warren, W.L.; Seager, C.H.; Tallant, D.R.; Voigt, J.A.; Gnade, B.E. Mechanisms behind graphene photoluminescence in ZnO phosphor powers *J. Appl. Phys.* 79, (1996), 7983-7990.

[10] Liao, L.; Duan, X. Graphene-dielectric integration for graphene transistors *Mater. Sci. Eng. R* 70, (2010), 354-370.

[11] Liao Z. M.; Liu, K. J.; Zhang, J. M.; Xu, J.; Yu, D.P. Effect of surface states on electron transport in individual ZnO nanowires *Phys.Lett. A* 367, **(**2007), 207-210.

[12] Liao, L.; Bai, J.; Qu, Y.; Lin, Y-C.; Li, Y.; Huang, Y.; Duan, X.; High-k oxide nanoribbons as gate dielectrics for high mobility top-gated graphene transistors *Proc. Natl. Acad. Sci. U.S.A* 107, (2010), 6711-6715.

[13] Wang, Y.; Huang, B-C.; Zhang, M.; Miao, C.; Xie, Y-H.; Woo, J. C. S. Fabrication of self-aligned graphene FETs with low fringing capacitance and series resistance *ISRN Electronics* 2012, (2012), 891480.

[14] Adam, S.; Hwang, E. H.; Galitski, V. M.; Das Sarma, S. A self-consistent theory for graphene transport *Proc. Natl. Acad. Sci. U.S.A* 104, (2007), 18392-18397.

CHAPTER IX

SUMMARY

This chapter summarizes the entire results of this dissertation. Initial part of this thesis deals with the electrical transport properties of an ideal defect- free multilayer, few-layer and single layer graphene. The electrical transport phenomenon of fabricated graphene devices showed the transition of metallic (MLG) to semiconductor (SLG) behavior with respect to their thickness. The semi-conducting behavior of SLG in R (T) measurement suggests that each graphene layer inside the graphite flakes are semiconductors.

The electronic transport properties of the multilayer graphene with and without defect were investigated where the defect-rich multilayer graphene exhibits semiconductor-like temperature dependence of the resistance. This defect-induced M-SC transition in multilayer graphene has the potential applications in advanced nonlinear devices.

The optoelectronic properties of defective single and fewlayer graphene was investigated which shows enhanced photoresponsivity when compared to the pristine device. A maximum photoresponsivity of 0.47 AW^{-1} and photoconductive gain of 1.1 were achieved with 535 nm light illumination and a bias voltage of 0 V, for defective fewlayer graphene, where as the defective-GFET showed a photoresponsivity of 37 mAW^{-1} for 535 nm illumination which is ~3 times higher than that of pristine.

The photo-sensing capability of graphene-CdSe QDs hybrid device was investigated by immobilizing CdSe QDs on graphene surface through electrochemical reduction of diazonium salt and demonstrated an enhanced, stable, wavelength dependent photosensor. The photoresponsivity of the hybrid device remarkably improved when compare to the pristine device, which shows 0.24 AW^{-1} under 535 nm light illumination.

Finally, we have fabricated a G-FET device with ZnO microwire as a top-gate electrode. The depletion layer of the ZnO Microwire is acting as a gate dielectric for G-FETs with thickness of ~98 nm. The device characteristics are well agreed with the existing device models. The STG-FET device gives the on on-current of 175 μA, on/off current ratio of 55 and the device mobility exceeds 1630 cm^2/V.s for holes and 1240 cm^2/V.s for electrons at room temperature. Self-induced gate dielectric process prevents the G-FETs from impurity doping, defect formation in graphene lattice and facilitates the fabrication process. The performance degradation of G-FETs can be overcome by our device structure.

PUBLICATION

1. Plasma-induced photoresponse in few-layer graphene, **Kaliannan Thiyagarajan**, Antony Ananth, Balasubramaniam Saravanakumar, Young Sun Mok, Sang-Jae Kim* *Carbon, 73: 2014, 25–33* (IF 6.160).

2. Self-induced Gate Dielectric for Graphene Field-Effect Transistor, **Kaliannan Thiyagarajan**, Balasubramaniam Saravanakumar, Rajneesh Mohan, and Sang-Jae Kim*, *ACS.Appl.Mater.Interfaces, 5:2013, 6443−6446* (IF 5.900), *dx.doi.org/10.1021/am401219x*

3. Thickness dependent electrical transport properties of graphene, **Kaliannan Thiyagarajan,** Balasubramaniam Saravanakumar, Rajneesh Mohan, and Sang-Jae Kim*, *Science of Advanced Materials 5 (6): 2013, 542−548* (IF 2.908), *DOI:http://dx.doi.org/10.1166/sam.2013.1485*

4. Defect-induced metallic-to-semiconducting transition in multilayer graphene, **Kaliannan Thiyagarajan,** Antony Ananth, Balasubramaniam Saravanakumar, Young Sun Mok, Sang-Jae Kim*, *RSC Advances (Needing Revision)*

5. Gate-Tunable Photoresponse of Defective Graphene: from Ultraviolet to Visible, **Kaliannan Thiyagarajan,** Balasubramaniam Saravanakumar, and Sang-Jae Kim*, *ACS Appl. Mater. Interfaces, (Needing Revision)*

6. Graphene-CdSe QDs hybrid device for photosensing application *(Manuscript under preparation)*

VITAE

skthiyagaraj@gmail.com

The author **Kaliannan Thiyagarajan** born in hills queen town of Ooty, Tamilnadu, India on 11th July 1983. He received his undergraduate and master degree from Bharathiyar University in **Physics**. He has also done M.Tech in **Nanoscience and Technology** at Anna University, Thichy India. His research interest his to fabricate sensors based on the two dimensional materials especially for optoelectronic applications.

Patent

South Korea National Invention Patent, Controlling the electronic properties of Graphene through ZnO micro wire, Sang Jae Kim and **Kaliannan Thiyagarajan,** *Application number:* ***1020120102092.***

Award

Best paper award in the 12th Joint ***Symposium of Nagasaki University and Jeju National University on Science and Technology,*** held on June 5 2013 at Jeju National University, Jeju, Korea

Project grant

Karunya University, Seed Money Project fund, **Rs 40,000,** *for the "**Preparation of Modified Membrane for the Waste Water Treatment: Removal of chromium Ions**"*.(Dec' 2010-July' 2011)